BUOYANCY FLUX ESTIMATES FOR A TIDAL CHANNEL.

by

PAUL MACOUN
B.A.Sc, University of Waterloo, 1995

A Thesis Submitted in Partial Fulfillment of the
Requirements for the Degree of

MASTERS OF SCIENCE

in the School of Earth and Ocean Sciences

We accept this thesis as conforming
to the required standard

[redacted]

Dr. R. G. Lueck, Supervisor (School of Earth and Ocean Sciences)

[redacted]

Dr. C. Garrett, Member (School of Earth and Ocean Sciences)

[redacted]

Dr. R. Dewey, Member (School of Earth and Ocean Sciences)

[redacted]

Dr. H. Yamazaki, External Examiner
(Department of Ocean Sciences, Tokyo University of Fisheries)

University of Victoria

Supervisor: Dr. R. G. Lueck

Abstract

A parameterization of the vertical flux of density based upon the physics of oceanic mixing processes is required for a wide variety of practical problems, but remains an elusive goal. In August 2000, the horizontal microstructure profiler TOMI was used over the course of six days, in Sansum Narrows, to make simultaneous measurements of temperature, conductivity, vertical velocity and their fluctuations. These data provide average estimates of the heat and salt flux, and thus the buoyancy flux, and estimates of the rate of dissipation of kinetic energy. Concurrent profiles of vertical shear and in-situ estimates of the buoyancy frequency provide the means to relate the ratio of buoyancy flux to dissipation rate, to the Froude number, and to the buoyancy Reynolds number over a wide range of these parameters. The ratio of buoyancy-to-kinetic energy production reaches 0.77 in Sansum Narrows, and is generally larger than the value of 0.2 assumed to apply to the open ocean. It also appears to decrease with increasing buoyancy Reynolds number, and peaks in a small range in Froude number.

Examiners:

[redacted]

Dr. R. G. Lueck, Supervisor (School of Earth and Ocean Sciences)

[redacted]

Dr. C. Garrett, Member (School of Earth and Ocean Sciences)

[redacted]

Dr. R. Dewey, Member (School of Earth and Ocean Sciences)

[redacted]

Dr. H. Yamazaki, External Examiner
(Department of Ocean Sciences, Tokyo University of Fisheries)

Table of Contents

List of Tables

List of Figures

Chapter 1

Introduction

Turbulence in the ocean, and the mixing it causes, has a direct bearing on the physical properties of the ocean. Turbulence brings nutrients to the surface, which nurtures plankton growth. It influences the dispersal of pollutants, and hence can readily affect quality of life. Most importantly, it governs climate through the transmission of heat between the ocean and the atmosphere. A mere 2.5 meters depth of water has the same heat capacity as the whole depth of the atmosphere, and the absorption, storage and release of this heat has an important long-term effect on global climate (Caldwell and Moum 1995). Turbulent motions in a stratified fluid rapidly intermingle fluid parcels from spatially separated regions, thereby enhancing mixing across concentration gradients at levels significantly greater than molecular diffusion alone. For these and many other reasons, understanding turbulence and mixing in the ocean is an important undertaking.

Turbulent motions rapidly dissipate in the absence of an energy source, making it difficult to assume steady-state conditions in a turbulent flow. It has also been observed that turbulence occurs most often in a "patchy" way, where intense regions of overturning are interspersed with relatively calm water. This non-steady and non-homogeneous nature for turbulent motions requires a conceptual framework that is primarily statistical.

Oceanographic features and conditions in coastal regions differ significantly from those in the open ocean. The channels on the east coast of Vancouver Island exhibit elevated surface temperatures due to solar input in the summer. Coincidentally, river runoff enhancing stability in the halocline leads to significant stratification of the water column. This stratified water is subject to forcing by tides, where large volumes of water must negotiate geographic and hydrographic constrictions. These tidal channels are typically turbulent, where vertical mixing of the stratified water is the result of overturning instabilities driven by vertical and horizontal shear. These turbulent regions allow for the heat absorbed at the surface, along with the fresh water from runoff, to be mixed through a considerable depth, while colder, saltier water at depth, which is rich in nutrients, is carried towards the surface. Vertical mixing results in vertical homogeneity, and an increase in the gravitational potential energy. This increase in potential energy comes from the kinetic energy of the turbulence, which in turn comes from the kinetic energy of the mean flow (Pond and Pickard 1983). The scales of turbulent overturns contributing to these vertical transports are on the order of centimeters, to tens of meters.

In August of 2000, our group, the Ocean Turbulence Laboratory, spent a week on board the Coast Guard Vessel *Vector* in the vicinity of Sansum Narrows, where we collected oceanographic data with three separate instrument systems. Mounted to the side of the ship was an Acoustic Doppler Current Profiler (ADCP), which provides a measure of the vertical shear in the water column. A Conductivity, Temperature and Depth instrument (CTD) was also on board, permitting the measurement of the vertical profile of density at set stations along the length of the channel. The third instrument employed was the TOMI (Towed Ocean Microstructure Instrument), which is a horizontal microstructure profiler towed aft of the ship at depths up to 60 meters. Over the course of the week, the TOMI was towed into currents generated by morning and evening ebb tides, and afternoon flood tides. Excellent ship handling and little technical difficulty resulted in the successful profiling of the entire channel for two morning ebb tides, three afternoon flood tides, and five evening ebb tides. In conjunction with these measurements, CTD profiling through the night, before and after tows, and during peak flows on August 13^{th} produced over 100 vertical profiles of density at 16 stations north of, within and south of Sansum Narrows. In addition, for most tows with the TOMI, the ship mounted ADCP was making concurrent measurements of velocity at depth for the estimation of vertical shear.

The TOMI hosts an array of instruments dedicated to the measurement of turbulent quantities, such as the characteristics of larger, flux supporting eddies, to microstructure, which are the smallest features of the flow. Measurement of in-situ temperature, salinity and vertical velocity fluctuations provides adequate information to calculate the vertical fluxes of heat and salt along the tow path through the correlation of these quantities. Because the density of seawater is dependent on its temperature and salinity, fluxes of heat and salt provide a direct estimate of the density flux. This direct estimate of the work done against buoyancy forces can be scaled by the energy lost to viscosity at dissipative scales to provide a measure of how efficiently the water is mixing. Values for this scaled buoyancy flux vary considerably over the length of Sansum Narrows, and peak in regions of increased stratification and somewhat reduced dissipation level. Lower scaled buoyancy flux estimates correspond to highly turbulent regions in the channel, where vigorous mixing has reduced the stratification and hence the opportunity for the turbulent flow to mix efficiently.

The following chapter presents the relevant theoretical background and summarizes some previous work carried out by other researchers in this field. Chapter 3 lends itself to a detailed description of the instrumentation and data processing methods utilized to obtain estimates for the buoyancy flux, the dissipation rate, the buoyancy frequency, and the vertical shear. Chapter 4 provides a detailed summary of the water properties of channels adjacent to Sansum Narrows, and an overview of results from flux and other measurements made within the channel during ebb and flood tides. These results are discussed in Chapter 5 with reference to findings from other experiments, and are summarized in Chapter 6 alongside a look at potential future work.

Chapter 2

Background and Theory

Fluxes of heat and salt dictate the nature of the density (or mass) flux of seawater. Two well known and utilized indirect methods for estimating fluxes require measurements of small-scale temperature gradient variance (Osborn and Cox 1972) and small-scale shear variance (Osborn 1980).

The Osborn-Cox method estimates the vertical eddy coefficient for heat (K_T) and the vertical heat flux ($\overline{w'T'}$) from the measurement of the dissipation of temperature variance (χ). Estimating the heat flux via this method was not possible for the data from Sansum Narrows, however, due to the inability of the thermistors to fully resolve the temperature gradient spectrum at typical tow speeds (~ 1 m s^{-1}). The Osborn method on the other hand estimates the eddy coefficient for density (K_ρ) and the work done by the buoyancy flux ($g/\rho\ \overline{w'\rho'}$) from the measurement of the dissipation of turbulent kinetic energy (ϵ), which is calculated from shear spectra. An overview of the Osborn method is discussed in Section 2.1.1., as it provides a framework for comparing direct estimates of the work done against buoyancy forces to the dissipation rate.

The motivation to directly measure turbulent fluxes stems from a number of deficiencies associated with indirect methods for estimating fluxes. Both methods require fundamental assumptions about the nature of turbulence. Furthermore, χ and ϵ are typically calculated from the measurement of a single component gradient, which is commonly not fully resolved, and require the assumption of local isotropy to establish full gradient variances from one-dimensional measurements.

Relatively recently, as a result of these inadequacies, attempts have been made to directly estimate the vertical heat flux ($\overline{w'T'}$) through the simultaneous measurement of vertical velocity (w') and temperature (T') fluctuations (Yamazaki and Osborn 1993, Fleury and Lueck 1994, Moum 1996, Wolk and Lueck 2001). Direct in-situ estimates of $\overline{w'T'}$ are technically challenging to determine, as they require the concurrent measurement of two quantities, necessitate longer data records from a statistical standpoint, and have the potential to be contaminated by platform motions. The advantage of direct flux estimates is they do not require assumptions about the nature of turbulent motions and their effect on mass transport. The work outlined in this document explores variability in directly measured heat and salt fluxes (and hence density fluxes) in a turbulent tidal channel. These quantities are determined through the measurement of vertical velocity (w'), temperature (T') and salinity (S') fluctuations. This correlation of w' with both T' and S' to determine heat and salt fluxes is commonly referred to as the Eddy Correlation Method, and is discussed in Section 2.1.2.

2.1 Flux Measurements

2.1.1 The Osborn Method

Osborn (1980) devised a method for estimating the local cross-isopycnal density flux ($\overline{w'\rho'}$) from the measurement of the dissipation of turbulent kinetic energy (ϵ). He proposed that turbulence is maintained by the turbulent energy production of the Reynolds stress working against the mean shear, while the dissipation of TKE and the work done against buoyancy act as sinks for the turbulent energy.

Water properties such as velocity (u_i), density (ρ) and pressure (p) can be decomposed into mean and fluctuating parts, i.e.

$$\begin{aligned} u_i &= \overline{u}_i + u_i', \\ \rho &= \overline{\rho} + \rho', \\ p &= \overline{p} + p'. \end{aligned} \tag{2.1}$$

The mean terms (i.e. $\overline{u}_i$) represent mean motions which are larger in scale and change more slowly in time than the fluctuating parts. The fluctuating part is considered to include those variations on scales (eddies) which contribute significantly to the mean-square shear, whereas most internal waves and tidal currents are considered here as part of the mean state. As will be shown, the largest flux supporting turbulent eddies in Sansum Narrows are on the order six meters, which correspond to a time scale of approximately 40 seconds.

By substituting these decomposed values into the basic Navier-Stokes equation, and then subtracting the fluctuating terms from the total equation, we get an equation of motion for turbulent velocity (u_i'). The multiplication of this form of the Navier-Stokes equation by u_i', followed by averaging in space, produces the turbulent kinetic energy equation

$$\left(\frac{\partial}{\partial t} + \overline{u}_j \frac{\partial}{\partial x_j}\right)\frac{1}{2}\overline{u_i'^2} + \frac{\partial}{\partial x_j}\left(\frac{1}{\rho}\overline{p' u_j'^2} + \frac{1}{2}\overline{u_i'^2 u_j'} - 2\nu\overline{u_i' e_{ij}}\right) = -\frac{g}{\rho}\overline{u_3'\rho'} - \epsilon - \overline{(u_i' u_j')}\frac{\partial \overline{u}_i}{\partial x_j}, \tag{2.2}$$

where e_{ij} is the strain rate tensor defined by

$$e_{ij} \equiv \frac{1}{2}\left(\frac{\partial u_i'}{\partial x_j} + \frac{\partial u_j'}{\partial x_i}\right), \tag{2.3}$$

and ϵ, the dissipation of turbulent kinetic energy, is given by

$$\epsilon = 2\nu(\overline{e_{ij}})^2, \tag{2.4}$$

where e_{ij} represents the sum of the strain rate tensor over all indices. The first term on the left hand side of equation 2.2 represents the total rate of change of TKE. Osborn equates this term to zero under the assumption that turbulence is steady in time and space, although in reality observed turbulence tends to be intermittent or "patchy". The next three terms in Eq. 2.2 are all divergences which equal their respective boundary values when integrated over the domain of the turbulence. They are: the work done by the pressure-gradient, the transport associated with turbulent velocity fluctuations, and the transport attributed to viscous stresses. Monin and Yaglom (1975) show that for atmospheric flows, the pressure-velocity correlation ($\overline{p'u_j'^2}$) and the viscous stresses term ($2\nu\overline{u_i' e_{ij}}$) can be generally neglected for parallel shear flow in the absence of a destabilizing heat flux.

Osborn simplifies the mean turbulent kinetic energy equation by assuming all terms on the left hand side of equation 2.2 are negligible, producing

$$-\overline{u'w'}\,\frac{\partial U}{\partial z} \;=\; \epsilon \;+\; \frac{g}{\overline{\rho}}\,\overline{w'\rho'}, \tag{2.5}$$

where $B = g\overline{\rho}^{-1}\,\overline{w'\rho'}$ is the work done by the buoyancy flux, and $P = -\overline{u'w'}\,\partial U/\partial z$ is the Reynolds stress working against the mean vertical shear. P is commonly referred to as the production term , and represents the exchange of kinetic energy between the mean flow and the turbulence. P is usually greater than zero, meaning the energy exchange involves a loss to the mean flow and a profit to the turbulence (Tennekes and Lumley 1972). The buoyancy term B on the other hand is a TKE sink ($B > 0$) if energy from the turbulence is converted into gravitational potential energy, or a TKE source ($B < 0$) either if waters are undergoing restratification or if destabilizing buoyancy exists at a boundary (i.e. surface cooling). The dissipation term ϵ represents the rate at which viscous stresses perform deformation work against the fluctuating strain rate, and is always positive, and hence a TKE sink. The assumption that all terms in equation 2.2 are small compared to P, B and ϵ remains a contentious issue. Turbulence is characteristically non-steady and spatially variable. An evaluation of all the terms in the turbulent kinetic energy equation for a highly turbulent tow segment is outlined in Section 2.3.

The flux Richardson number (R_f) is defined as the ratio of the buoyancy term (B) to the production of TKE (P), and is generally assumed to be less than one for steady state turbulence. Stewart (1959) argues than in fact R_f should be considerably less than one for maintained turbulence in a shear flow, since energy is only lost vertically to work done by the buoyancy flux, whereas losses to viscosity are occurring in all three velocity components. At higher values of R_f, it seems unlikely that turbulence can be maintained under the strain of significant buoyancy losses. A variety of laboratory experiments have produced estimates for R_f that lie in the $0.15 - 0.20$ range (Britter 1974, Ellison 1957).

By assuming Osborn's simplified form of the TKE equation, the buoyancy flux term B can be defined in terms of R_f and ϵ, i.e.

$$B \;=\; \frac{g}{\rho}\overline{w'\rho'} \;=\; \frac{R_f}{1-R_f}\,\epsilon, \tag{2.6}$$

where w' is the fluctuating component of velocity in the vertical, ρ' is the instantaneous deviation of density from the mean density, and their product averaged is the flux of density.

A mixing efficiency can thus be described by

$$\Gamma = \frac{R_f}{1 - R_f}, \tag{2.7}$$

where Γ represents the ratio of work done against buoyancy forces, to the energy lost to viscosity at dissipative scales. A common choice for Γ is 0.2, which was suggested by Osborn (1980) as a maximum value for a long term average. Experimental evidence suggests that Γ is in fact a highly variable parameter, and is further discussed in Section 2.2.1.

2.1.2 The Eddy Correlation Method

The buoyancy term (B) from Eq. 2.6 can be established directly through the concurrent measurement of vertical velocity (w), temperature (T) and salinity (S).

These quantities, like velocity, can be separated into mean and fluctuating parts, i.e.

$$T = \overline{T} + T', \tag{2.8}$$

$$S = \overline{S} + S'. \tag{2.9}$$

Measurements of temperature and salinity, when demeaned, yield fluctuating values T' and S', which can be used to estimate ρ' according to

$$\frac{1}{\rho}\rho' = -\alpha T' + \beta S', \tag{2.10}$$

where $\alpha = -\rho^{-1}\ \partial\rho/\partial T$ is the thermal expansion coefficient and $\beta = \rho^{-1}\ \partial\rho/\partial S$ is the contraction coefficient for salinity.

By multiplying both sides of Eq. 2.10 by the fluctuating vertical velocity (w'), and then taking the mean, we obtain

$$\frac{B}{g} = \frac{1}{\rho}\overline{w'\rho'} = -\overline{w'(\alpha T' - \beta S')} = -\alpha\overline{w'T'} + \beta\overline{w'S'}. \tag{2.11}$$

The eddy correlation or direct method relies on the successful measurement and correlation of w', T' and S' signals. Their co-spectra yield estimates of the heat and salt flux, and hence provide a direct estimate of the in-situ work done against buoyancy forces ($B = g/\rho\ \overline{w'\rho'}$). Adding to this, the measurement of the dissipation of turbulent kinetic energy provides an average estimate of the work done against buoyancy forces relative to energy lost to dissipation, where the ratio

$$R = \frac{\frac{g}{\rho}\overline{w'\rho'}}{\epsilon}, \tag{2.12}$$

is herein called the "scaled buoyancy flux". Estimates of R are equivalent to the mixing efficiency (Γ) defined by Eq. 2.6 for regions in a turbulent flow where all terms from the turbulent kinetic energy equation except for P, B and ϵ can be neglected.

In this thesis, the eddy correlation method is used to obtain estimates of the buoyancy term B for various regions in Sansum Narrows during ebb and flood tides. Comparison of these estimates to the dissipation of TKE provide a direct estimate of the ratio of work done by the buoyancy flux, to energy lost at dissipative scales.

2.2 Previous Work

2.2.1 Past Estimates for Γ

Based on earlier estimations of R_f (Britter 1974, Businger 1973), Osborn (1980) suggested an upper value of approximately 0.2 for Γ (see Eq. 2.7). A variety of studies based on the eddy-correlation method have yielded a wide range of results for Γ, from as low as 0.02, to as high as 0.7. This large experimental range in Γ estimates dissuades us from believing that $\Gamma \leq 0.2$ applies to all flows in the ocean, and certainly emphasizes the need for understanding on how mixing efficiency may be parameterized in terms of other flow quantities.

Oakey (1982) made estimates of mixing efficiency based on measurements of temperature and shear using a vertical profiler. Based on arguments by Osborn and Cox

(1972), he estimated the vertical eddy diffusivity (K_z) using the temperature gradient variance ($\overline{(\partial T'/\partial z)^2}$) and the mean temperature gradient ($\partial\overline{T}/\partial z$). By also assuming that the buoyancy frequency (N) can be obtained from the temperature gradient, Oakey was able to estimate the mixing efficiency according to $\Gamma = K_z N^2/\epsilon$. From 25 vertical profiles, estimates of Γ ranged from 0.031 to 1.037. The mean and standard deviation of his results are $\Gamma = 0.259 \pm 0.214$.

Moum (1990) estimated the heat flux using the eddy-correlation method from data obtained using a vertical profiling instrument in the main thermocline. His measurements of w' were made using a piezo-resistive pressure transducer mounted in a Pitot tube, and his T' measurements were made with a thermistor. He found that flux transports are dominated by scales of many tens of centimeters, with characteristic w' values of several centimeters per second. He also found a considerable countergradient contribution in his flux estimates at any given time, while indirect methods only provided downgradient transports. As a result, his direct estimates for the average heat flux over 40 turbulent patches was -50 W m^2; the indirect method based on ϵ yielded an average heat flux of -420 W m^2, indicating $\Gamma \approx 0.02$.

Another effort to directly measure the heat flux was made by Yamazaki and Osborn (1993) with the use of an extremely stable platform, the submarine *USS Dolphin* in a weakly stratified, shear driven, turbulent layer. They used the low frequency content of signals from airfoil shear probes to establish w', and obtained T' from a thermistor. Their results indicated that direct measurements of the heat flux coincided with indirect estimates at $\Gamma = 0.05$, which they argued is consistent with nearly steady state mixing efficiencies determined from laboratory experiments (Rohr and Atta 1987). Their findings indicated that the length scale contributing most significantly to the heat flux was on the order of 1 m.

Fleury and Lueck (1994) made direct estimates of vertical heat flux using data collected with a towed vehicle in (1) a well defined turbulent interface at 400 m, (2) sporadic layers of turbulence in the thermocline near a salinity maxima and (3) a thermal inversion at the base of the surface mixed layer. Their estimates of Γ for these three regions are (1) 0.01 to 0.28, (2) 0.03 to 0.11 and (3) 0.05 to 0.12. Γ has a range in value for all three regions, and is consistent with the notion of a flux Richardson number smaller than $R_f \approx 0.2$. The largest wavenumber contributing to the flux was $6k_o$, where k_o, the Ozmidov wavenumber, is defined by

$$k_o = \frac{1}{2\pi}\left(\frac{N^3}{\epsilon}\right)^{\frac{1}{2}}, \tag{2.13}$$

and represents the wavenumber associated with the longest overturning length scale allowed by the ambient stratification. The smallest wavenumber resolved by Fleury and Lueck was limited through high-pass filtering to $0.5k_o$, due to body motion contamination at the lowest wavenumbers. One important feature of their co-spectra was a distinct lack of a flux maxima, which indicated that a potentially significant fraction of the total heat flux remained unresolved below their lower wavenumber limit, suggesting their estimates for Γ are unreliable.

An array of instruments provided Gargett and Moum (1995) with direct estimates of the density flux at a single depth in a turbulent tidal flow. A CTD that provided measurements of T' and S' was towed at depth in line with the projected vertical beam of a modified ADCP, which provided an estimate for w'. Their estimates for the density flux were then compared to indirect estimates based on ϵ and χ, which were derived from data obtained using a vertical microstructure profiler. They estimated Γ to be as high as 0.7 ($R_f = 0.4$), and pointed out that there are no validated predictions as to the magnitude of R_f expected for the exceptionally high Reynolds numbers they witnessed ($Re = uh/\nu \approx 10^7$). They further argued that these elevated mixing efficiencies were potentially the result of frontal vertical flows supplying energy directly to the vertical component (w'^2) of TKE.

Moum (1996) revisited the direct measurement of heat flux in the thermocline with the use of a pitot tube capable of resolving 1 mm s^{-1} fluctuations in vertical velocity. Vertical profiles of turbulent patches, when compared to the Osborn method (Section 2.1.1), yielded $\Gamma \approx 0.15 - 0.20$, although there was concern that fairly large uncertainties in the estimates existed due the limited thickness of observed turbulent patches. These results are in keeping with Osborn's (Osborn 1980) original long term average estimate for Γ.

The uncertainties in estimates of Γ experienced by Moum can be much reduced by sampling turbulence with a horizontal profiler. Wolk and Lueck (2001), hereafter WL, used the horizontal profiler the TOMI to make concurrent measurements of

w' and T' at night in the oceanic boundary layer. Direct heat flux estimates were compared to indirect estimates based on ϵ, yielding a range in Γ from 0.08 to 1.38. The average estimate for mixing efficiency in stable regions was $\overline{\Gamma} = 0.46$, which is close but slightly higher than the maximum mixing efficiency predicted by classical scaling arguments and laboratory results (Rohr and Atta 1987, Rohr et al. 1988, Lienhard and Atta 1990, Ivey and Imberger 1991, Barry et al. 2001). WL calculated an alternative average estimate of the mixing efficiency from the inverse of the mean of the inverse, producing $(\overline{\Gamma_o^{-1}})^{-1} = 0.29$. The confidence interval of the direct average did not encompass the inverse average, and WL argued this is a statistical issue related to the slow convergence of their flux ratio to its true value. In order to avoid the limitations imposed by instrument motions at low wavenumber (Fleury and Lueck 1994), a motion correction algorithm was developed that made it possible to resolve overturning wavelength scales up to 33 meters. This improvement in resolution allowed them to determine that the largest overturning scales supporting fluxes were approximately 2 meters.

In good part due to these estimates from the ocean, and to some degree as a result of experimental efforts, it has emerged that the mixing efficiency is a dynamic and variable parameter. This range in values for Γ may be due to the neglecting of significant divergence terms in the TKE equation, or are possibly as a result of unresolved variability of measured parameters within three-dimensional and potentially non-steady turbulent patches (Moum 1996), or can even be attributed to differences in the instability leading to the observed turbulence (Gargett and Moum 1995). The available theories for the dependence of R_f on dimensionless parameters such as the buoyancy Reynolds number ($Re_b = \epsilon/\nu N^2$) and Froude number ($Fr = U_z/N$) are either based on scaling relationships, validated against laboratory flows, or stem from numerical simulations in which $B = g/\rho\ \overline{w'\rho'}$ can be directly determined (Gargett 1988, Ivey and Imberger 1991, Itsweire et al. 1992, Barry et al. 2001).

Ruddick and Walsh (1997) collected microstructure data from the North Atlantic and used the dissipation estimates to compute the "apparent mixing efficiency", Γ_d, where

$$\Gamma_d = \equiv \frac{\chi N^2}{2\overline{\overline{T_z^2}}\epsilon}. \tag{2.14}$$

These computed values were then used to investigate variations in Γ_d with respect to the density ratio ($R_\rho = \alpha T_z/\beta S_z$) and the buoyancy Reynolds number, in an attempt to highlight the underlying physics of mixing in the region. The authors found that Γ_d is a somewhat increasing function of Re_b in the 100-1000 range, and a slight decreasing function of R_ρ. St. Laurent and Schmitt (1999) used microstructure observations at the NATRE (North Atlantic Tracer Release Experiment) site to assess the strength of salt finger mixing (Γ_d) over a range in Richardson number and density ratio. For doubly stable regimes, they found Γ_d values ($0.1 < \Gamma_d < 0.25$) to be in good agreement with the results of previous studies (Moum 1996, Ruddick and Walsh 1997), and that Γ_d appeared to have no discernable dependence on R_ρ for $0.25 < Ri < 5$. Favourable salt finger conditions on the other hand produced similar Γ_d values to the doubly stable data for $Ri < 1$, but higher values for Γ_d at larger values of the Richardson number.

Smyth et al. (2001) studied the time evolution of mixing in turbulent overturns using both a direct numerical simulation and microstructure measurements. During the simulations, the ratio of work done against gravity to energy dissipated via friction (R) would typically change by more than an order of magnitude through the course of the overturn. The ratio of the Ozmidov scale ($L_O = (\epsilon/N^3)^{0.5}$) to the Thorpe scale ($L_t = \langle\delta^2\rangle^{0.5}$) was found to increase monotonically with time in the simulated flows, and could potentially be used to account for the time dependence of R on the evolution of the overturn. The Ozmidov scale provides an estimate of the length scale above which motions are strongly affected by buoyancy, and the Thorpe scale is the root mean square of the vertical displacement of water parcels from equilibrium depth (Thorpe 1977). Smyth et al. suggest that the evolution of R is determined more by the Prandtl number ($Pr = \nu/\kappa$) than by the initial Reynolds number. Early in the evolution, mixing efficiency increases to its peak with decreasing Prandtl number, followed by a longer decay phase, where the asymptotic value of $R \approx 0.2$ is maintained for $\mathrm{Pr} = 7$, 4 and 2, but is almost twice as large for $\mathrm{Pr} = 1$.

2.3 Assessing Assumptions

Osborn's simplification of the turbulent kinetic energy equation to obtain the balance described by Eq. 2.5 warrants some consideration. Steady state conditions and a homogeneous flow are assumptions that must be cautiously applied to turbulence. The well known patchiness of turbulent overturns discounts the homogeneity assumption for averages over large areas, and trends in the dissipation rate over time indicate the growth and decay of turbulence. Also, neglecting divergence terms strictly requires averaging over the full three-dimensional volume of the turbulent patch, which is impossible to achieve from field measurements (Moum 1996).

A seventeen minute data segment from the 15^{th} of August was selected for the purpose of estimating the relative importance of all the terms in the TKE equation. The file corresponds to a highly turbulent region during a flood tide, where the vehicle undergoes a depth change of over 30 meters. This range in depth allows for the estimation of the terms in the TKE equation associated with vertical gradients. Data segments corresponding to significant depth variation were typically omitted to avoid possible temperature contamination in the airfoil probes, which has the potential to influence flux estimates. However, the chosen data segment comes from a well mixed region in the flow that shows reduced stratification in temperature, which suggests the risk of low frequency temperature fluctuations and hence contamination in the airfoil probes is low. The effect of temperature on shear probes is discussed further in Section 3.4.5. This data segment was also selected because it corresponds to a time when the vehicle makes little forward progress along the channel, and as such provides a better estimate of the rate of change in the vertical without an associated change of position in the horizontal.

The average dissipation rate for this data segment is $\epsilon = 1.05 \times 10^{-4}$ W kg^{-1}. The buoyancy term, determined from heat and salt fluxes, is $B = 3.83 \times 10^{-5}$ W kg^{-1}. Excluding the production term (P), the remaining terms in the TKE equation are (from Eq. 2.2)

$$1)\ \frac{\partial}{\partial t}\left(\frac{1}{2}\overline{u'^2}\right)\ 2)\ W\frac{\partial}{\partial z}\left(\frac{1}{2}\overline{u'^2}\right)\ 3)\ \frac{\partial}{\partial z}\left(\frac{1}{\overline{\rho}}\overline{p'w'^2}\right)\ 4)\ \frac{\partial}{\partial z}\left(\frac{1}{2}\overline{u'^2w'}\right)\ 5)\ \frac{\partial}{\partial z}\left(2\nu\overline{u'e'_{ij}}\right), \tag{2.15}$$

where u' and w' are the fluctuating along-stream and vertical components of velocity.

The first term corresponds to the rate of change of turbulent kinetic energy with time. A sufficiently long interval of time over which to assess changes in mean kinetic energy level is defined by the inverse of the tidal frequency Ω (rad/hr), i.e.

$$\frac{1}{\Omega} = \frac{1}{2\pi f} = \frac{1}{2\pi(\frac{1}{12})} \approx 2 \text{ hours}. \tag{2.16}$$

Kinetic energy is highest at mid-tide, and drops to zero at tides near slack. In other words, $\overline{u'^2}$ drops from a maximum at peak flow, to near zero, in the time interval $1/\Omega$. Data segments from tows in Sansum Narrows varied in length, from minutes to tens of minutes, thus producing buoyancy flux estimates at time scales significantly shorter than $1/\Omega$. The seventeen minute data segment selected for the computation of neglected terms in the TKE equation is therefore viewed as a worst case scenario.

The estimate for $\overline{u'^2}$ is determined using $\overline{w'^2}$, since u' was not measured. If stratification is assumed to suppress w' somewhat, then it is likely u' is in fact larger than w', and as a result this substitution yields an underestimate of the rate of change of TKE with time. However, low stratification estimates for the chosen data file suggest this discrepancy between velocity components is small, and hence it is reasonable to assume $u' \approx w'$. Based on these assumptions, a value of 1.04×10^{-6} W kg^{-1} was calculated for the rate of change of TKE with time, which is over 30 times smaller than the buoyancy term B. Term (2) from (2.15) is the transport of turbulent kinetic energy in the vertical, which is neglected since we assume that the average velocity in the vertical is zero ($W = 0$). There are regions in Sansum Narrows where bottom topography could theoretically produce a non-zero value for W, however, the data file used here comes from within the narrowest part of the channel, where local depth appears to be fairly level despite the presence of depth changes to the south and north.

The three remaining terms in (2.15) are all divergences, and represent the rate of change of turbulent kinetic energy due to pressure-gradient work (3), transport by turbulent velocity fluctuations (4), and transport by viscous stresses (5). These terms were assessed by evaluating turbulent quantities in two regions with significantly different mean depths; the assumption that vertical gradients are on larger scales than indicated by this depth range is required. Insufficient profiling time at depths within this range make the assessment of these quantity gradients on smaller scales impossible.

From two 200 second data segments at mean depths of 58 and 23 meters, estimates of $\overline{p'w'^2}$ are determined by calculating fluctuations in pressure (p') using $0.5\rho w'^2$. This substitution results in the quadruple correlation $\overline{w'^4}$, which is likely to be an overestimation of rate of change of TKE due to pressure gradient work because the correlation between p' and w'^2 is likely somewhat low, whereas the correlation of w' with itself is high. The merit of this method is that in finding a low value for the term, we can be sure that it remains insignificant with respect to the buoyancy and dissipation terms. The rate of change of TKE due to pressure-gradient work, based these assumptions, is 1.60×10^{-6} W kg^{-1}, and is less than a twentieth of B.

The transport of turbulent velocity fluctuations (4) is assessed using the same two data segments used to evaluate term (3) in (2.15). As was the case with estimating the rate of change of TKE with time, the along-stream fluctuating velocity component u' is substituted with w'. The argument that u' is likely to be larger than w' is still an issue here, but the low correlation (0.1-0.2) of u' with w' for turbulence renders this difference insignificant. In fact, the triple correlation of w' with itself is likely to overestimate the transport of turbulent velocity fluctuations. With these considerations in mind, term (4) equates to 2.80×10^{-6} W kg^{-1}, and is about a tenth of the value for B. The transport by viscous stresses term (5) is readily determined by using the values for e_{ij} associated with the measured dissipation rate for the two data segments, where $e_{ij} = \sqrt{\epsilon/2\nu}$. These values, alongside mean estimates of w' at both depths (assuming $w' \approx u'$), yield an estimate of 3.21×10^{-9} W kg^{-1} for the transport by viscous stresses term.

Another term from the three dimensional equations for turbulent kinetic energy worth consideration is the transport of TKE horizontally along the channel. This term is described by

Term	Assumptions	Value (W kg^{-1})	wrt ϵ
$\frac{\partial}{\partial t}\left(\frac{1}{2}\overline{u'^2}\right)$	$t = 7200$ s, $u' \approx w'$	1.06×10^{-6}	1×10^{-2}
$W\frac{\partial}{\partial z}\left(\frac{1}{2}\overline{u'^2}\right)$	$W \approx 0$, $z = 35$ m	-	-
$\frac{\partial}{\partial z}\left(\frac{1}{\rho}\overline{p'w'^2}\right)$	$z = 35$ m, $p' \sim \frac{1}{2}\rho w'^2$	1.60×10^{-6}	2×10^{-2}
$\frac{\partial}{\partial z}\left(\frac{1}{2}\overline{u'^2w'}\right)$	$z = 35$ m, $u' \approx w'$	2.80×10^{-6}	3×10^{-2}
$\frac{\partial}{\partial z}\left(2\nu\overline{u'e'_{ij}}\right)$	$z = 35$ m, $u' \approx w'$, $e_{ij} = \sqrt{\frac{\epsilon}{2\nu}}$	3.21×10^{-9}	3×10^{-5}
$U\frac{\partial}{\partial x}\left(\frac{1}{2}\overline{w'^2}\right)$	$U \approx 2$ m s^{-1}, $x = 3700$ m, $\overline{w'^3} \sim \frac{\epsilon}{l}$	1.70×10^{-6}	2×10^{-2}
$\frac{g}{\rho}\left(\overline{w'\rho'}\right)$	-	3.83×10^{-5}	3.6×10^{-1}

Table 2.1: Estimates of terms from the TKE equation with respect to dissipation rate for 17 minutes of data. For this file segment, the buoyancy term $B = g\overline{\rho}^{-1}\ \overline{w'\rho'}$ is approximately 1/3 the value of ϵ, while no other term exceeds 1/10 of the value for B.

$$U\frac{\partial}{\partial x}\left(\frac{1}{2}\overline{w'^2}\right), \tag{2.17}$$

and can be evaluated using scaling arguments with respect to dissipation level. We assume $\epsilon \sim w'^3/l$, where w' is the magnitude of vertical velocity fluctuations, and l is the dominant turbulent length scale, which is determined by the peak in the velocity spectrum. The horizontal transport of TKE (2.17) can be assessed by knowing how ϵ changes over the length of the channel, and by assuming a mean flow speed (U) along its length. The dissipation rate in the narrowest part of the channel was on the order 10^{-4} W kg^{-1} at peak tide, whereas 2 nautical miles up or downstream from this region ϵ was typically on the order 10^{-6} W kg^{-1}. Velocity spectra from both these regions had similarly located spectral peaks at approximately $k = 0.04$ cpm, which corresponds to a dominant turbulent length scale of $l \sim 1/(2\pi \times 0.04) \sim 4$ meters. By assuming a mean channel velocity of 3-4 knots ($U \approx 2$ m s^{-1}), and a channel length of 2 nautical miles (3.7 kilometers), the term defined by (2.17) equates to 1.70×10^{-6} W kg^{-1}, suggesting horizontal transport of TKE is small with respect to the buoyancy and dissipation rate terms for the data segment in question.

Through this fairly simple analysis it is apparent that the terms neglected by Osborn are in fact quite small for the data segment selected here. The net effect of including all of these terms in the TKE equation would be to increase the estimate of the production term P by 3-4 %.

Chapter 3

Instrumentation

3.1 TOMI

The TOMI (Towed Ocean Microstructure Instrument) is the Ocean Turbulence Laboratory's instrument for measuring ocean microstructure. Motivation for its development stemmed from a number of inadequacies plaguing users of free-falling vertical profilers. Vertical profilers produce short record lengths with characteristically large uncertainties as a result of the "thinness" of turbulent patches (Moum 1996). The TOMI profiles horizontally, and as such is ideal for investigating the long, horizontal patches of turbulence that frequent the ocean. By profiling within turbulent patches for extended periods, the uncertainties associated with oceanic turbulence measurements are considerably reduced.

The main body of the instrument is a modified fuel tank from the wing of a navy jet fighter. Within its cigar shaped outer hull resides an inner cylindrical hull which houses the two pressure cases containing the instrument's electronics. The forward pressure case protrudes about 30 cm in front of the hull, and its aft two-thirds is wrapped in thick open-cell polyurethane to minimize the effect of high frequency body vibrations on the turbulence sensors mounted on the forward end of the case. A set of fins attached at the stern of the vehicle provide stability and directionality while in tow, and two masts project 1.5 meters vertically up and 1 meter down midway along the body. A 70 kg weight is fixed to the far extremity of the lower mast to ensure the vehicle remains in the prescribed orientation during profiling. The inclusion of masts on the TOMI allow for the spatial separation of temperature and conductivity instruments, which provide an estimate of the vertical density gradient (see Section 3.2.3). Syntactic foam fills the void between the two hulls, which renders the instrument neutrally buoyant. Lead plates within the center space are added to

Sensor	#	Quantity	Units	Rate (s^{-1})	Location
Keller Pressure Transducer	1	P $P + \mathrm{d}P/\mathrm{d}t$	dbar	64	Mid-body
Propeller Current Meter	2	$U1$ $U2$	m s^{-1} m s^{-1}	64	Top Mast Bottom Mast
Linear Servo Accelerometers	3	a_x, a_y, a_z	m s^{-2}	512	Nose Cone Internal
Angular Rate Gyros	3	ω_x, ω_y, ω_z	rad s^{-1}	128	Nose Cone Internal
Compass	1	ψ	rad	64	Pressure Case
Sea-Bird Sensors	3	C T	S m^{-1} °C	64	Nose, Top Mast Bottom Mast
Airfoil Shear Probes	4	$\partial w/\partial t$ $\partial v/\partial t$	m s^{-2} m s^{-2}	512	Nose
Thermometrics FP07 Thermistor	2	T $T + \mathrm{d}T/\mathrm{d}t$	°C	512	Nose

Table 3.1: The TOMI's sensor array and the quantities measured. Shear probes and thermistors are sampled at higher rates in order to resolve the small scales associated with dissipation of TKE (ϵ) and the dissipation of temperature variance (χ).

give the vehicle a slightly negative buoyancy on the order ≈ 10 kg.

The vehicle is towed by and communicates with shipboard computers through a six conductor Kevlar cable, which connects to the vehicle at a tow point near the nose. Extended periods of observation and data processing indicate that the instrument closely follows movements at the nose, and has an equilibrium pitch angle of about $-2°$ (slightly nose-down). The tow cable runs forward and slightly up about 50 meters from the vehicle nose to a weighted section that acts as a damper to sudden cable movements from further up the tow line. In this configuration, about 350 meters of available tow cable allows for depth penetration to over 60 meters, which is more than adequate for measurements in Sansum Narrows. The shipboard terminus of the tow cable is a transceiver dedicated to telemetry electronics, which is linked to both a computer which logs the data and another machine which outputs a real-time visual display of certain key quantities.

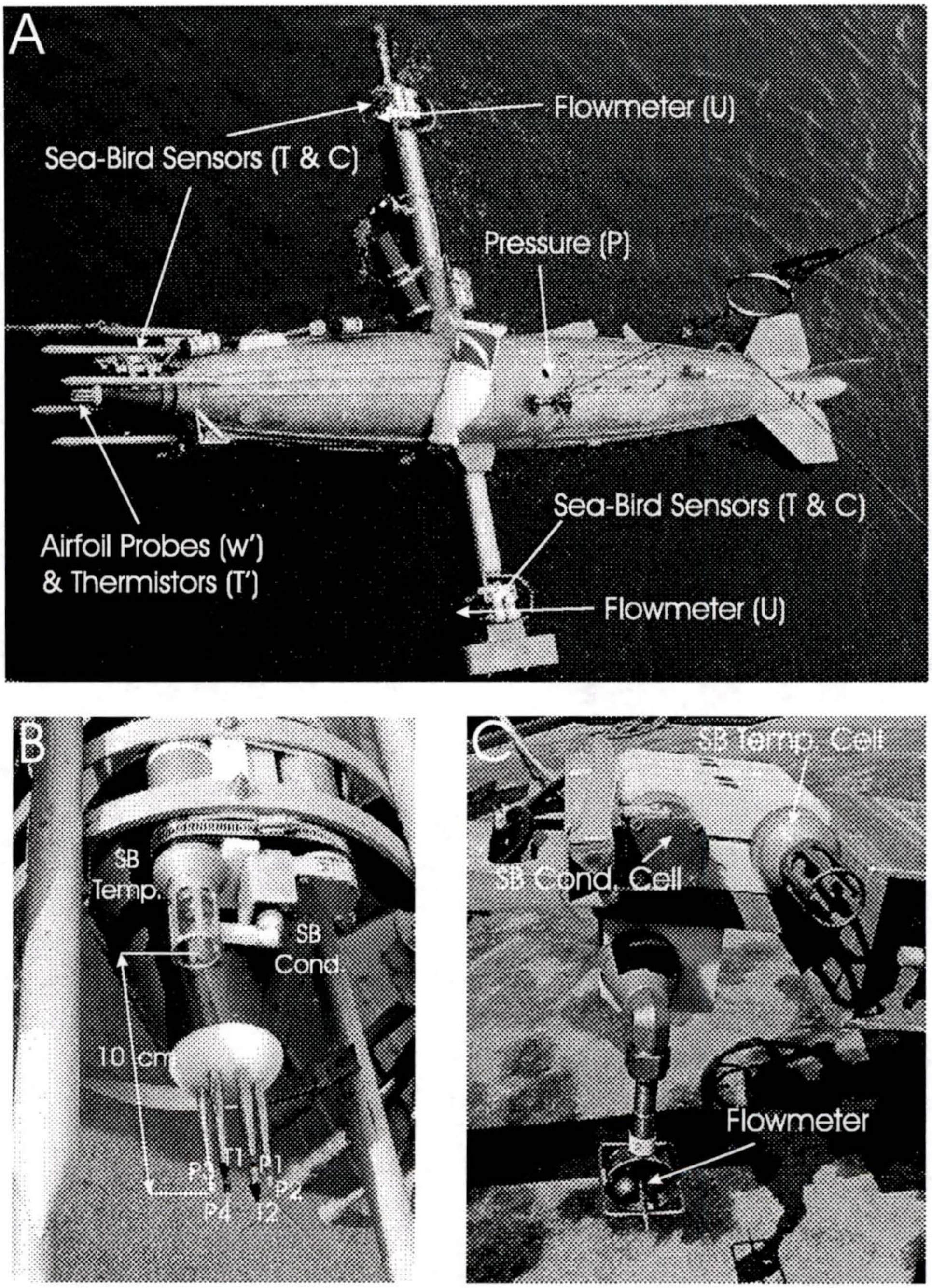

Figure 3.1: (A) The TOMI (Towed Ocean Microstructure Instrument) and its array of instrumentation. (B) A view of the vehicle nose and the position of the airfoil shear probes (P1-P4) and thermistors (T1-T2) relative to the nose *Sea-Bird* sensors. (C) A *Sea-Bird* temperature and conductivity sensor at the base of the lower mast used in conjunction with *Sea-Bird* sensors on the upper mast to estimate the square of the buoyancy frequency (N^2). Co-located is a flow meter used to estimate vehicle speed (U) through the water.

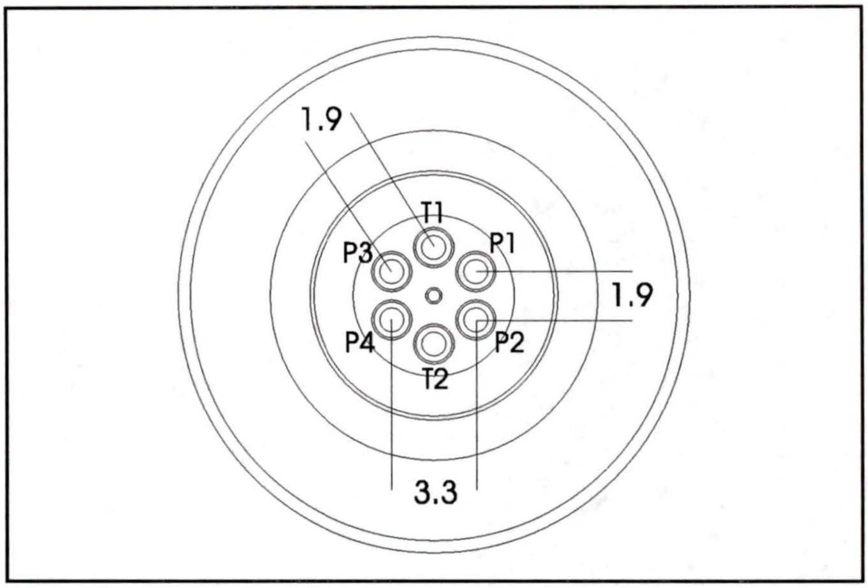

Figure 3.2: A front view of the airfoil probe (P1-P4) and thermistor (T1-T2) positions on the TOMI's nose. Dimensions are in centimeters. The probe in position P1 and the thermistor in T1 were used to estimate heat fluxes, as was the probe in P2 in conjunction with T2. Positions P3 and P4 were occupied by either Bullet probes or horizontally oriented Mantle probes.

3.1.1 Sensors

The TOMI supports a host of instruments in a variety of locations. They are, starting from the nose:

- 4 airfoil shear probes for the measurement of dissipation rate (ϵ) and instantaneous vertical velocity (w'). They were oriented vertically and horizontally, in close proximity to one another (see Fig. 3.2). Some tows were made using the new, smaller Bullet probe in positions P3 and P4 for comparison to the response from the Mantle probe (Macoun and Lueck 2002). These newly designed probes are approximately one half the size of the conventional Mantle, and hence have improved spatial resolution. Vertical velocity fluctuations (w') were determined exclusively using Mantle signals due to pronounced low wavenumber contamination in Bullet signals up to 1 Hz.
- 2 fast-response *Thermometric* FP07 thermistors for the measurement of temper-

ature fluctuations (T'), mounted above and below the cluster of airfoil probes. Regression with a *Sea-Bird* thermometer mounted near the nose was required for calibrating the thermistor signals.

- *Sea-Bird* temperature and conductivity cells, mounted approximately 10 centimeters behind the shear probe tips, provided estimates of the fluctuations in salinity (S').
- a multi-axis inertial sensing system for measuring linear accelerations and angular rates at the nose of the vehicle. Output was used to compute the body velocities (w_b') required to correct airfoil probe signals. The motion package is mounted inside the pressure case nose cone approximately 32 centimeters directly aft of the shear probe tips.
- a *Keller* pressure transducer at the back end of the forward pressure case for determining vehicle depth.
- *Sea-Bird* temperature and conductivity cells mounted in pairs at the top of the upper mast and bottom of the lower mast. Concurrent measurements provided estimates of the vertical gradient of density, and the square of the buoyancy frequency (N^2).
- propeller type current meters at the top of the upper mast and bottom of the lower mast. Their signal average was used as an estimate for the vehicle speed U; vehicle speed is used in the calculation of the spatial gradients of velocity ($\partial w/\partial x$).

To reduce the quantization noise and increase the resolution of the pressure (depth) measurement, the pressure P is pre-emphasized by combining it with it's scaled derivative ($68 \times \partial P/\partial t$) before sampling (Mudge and Lueck 1994). The enhanced pressure signal is extracted by convolving the combined signal with a single-pole low-pass filter with a cut-off that is determined by the scale factor applied to the derivative ($f_c = 1/2\pi \times 68$). The new, high resolution pressure data are then converted into units of decibars, which can be interpreted as meters of depth. The rate of change of P is a measure of the vehicle's vertical velocity through the water, and served as a check on calculations of the body velocity w_b' calculated using inertial measurements. The issue of fluctuating velocities associated with turbulent motions affecting pressure measurements was addressed by Wolk (1997), who found that a w' of 20 cm s^{-1} would contribute to a p' of only 0.002 dbar.

The digitized frequency output from the flow meters provide estimates of velocity (U) in meters per second. Calibration of these sensors was performed in a variable speed flow tank before and after the cruise. Time series from both meters were converted directly into physical units before "cleaning" with the use of a despiking algorithm. The last signal conditioning step was smoothing of the signal by the application of a low-pass filter with a cut-off at 1 Hz.

3.2 $d\mathrm{U}/dz$, ϵ and N^2

3.2.1 Vertical Shear ($d\mathrm{U}/dz$)

Estimates of vertical shear were obtained using a 600 KHz ADCP mounted near the stern of the ship. It was configured to generate two orthogonal estimates of horizontal velocity in 1 meter vertical bins. These velocity estimates were used to calculate a velocity magnitude for each one meter interval using the central approximation theory, thereby providing sufficient information to estimate vertical shear (dU/dz).

Comparison of the TOMI data with shear estimates from the ADCP requires the shifting of series in time so that they correspond in space. This shifting carries with it some error since the TOMI was not always at a constant distance, and hence time lag, behind the ship. The amount of shifting was determined by comparing shear estimates from the ship mounted ADCP and dissipation estimates from airfoil probes mounted on the TOMI. Coherent fluctuations in both quantities was typically detectable at a time lag of approximately 150 seconds. This lag indicates that the TOMI was on average 150 – 200 meters behind the ship.

3.2.2 Dissipation of TKE (ϵ)

Horizontal and vertical velocity components were measured with single-axis airfoil probes mounted orthogonally on the nose of the TOMI. For a detailed description of the airfoil probe designed for oceanic applications refer to Osborn and Crawford (1980), Siddon and Ribner (1965), Siddon (1971) and Oakey (1977).

The probe is a pointed body of revolution which utilizes hydrodynamic lift force to measure one cross-stream component of velocity. The cross-force on this axi-symmetric surface is detected by an insulated strain transducer. The transducer is a piezo-ceramic beam, which acts as a capacitively coupled voltage source. The voltage output passes through a charge coupled amplifier, and then through a differentiating circuit to improve the signal-to-noise ratio at higher frequencies. In the presence of a constant speed through the water, this differentiated signal becomes a measure of the along-stream gradient of cross-stream velocity fluctuations (Osborn and Crawford 1980). The probe is mounted so that its mean travel velocity (U) through the water is aligned with the axis of revolution of the probe, and the measured signal is the fluctuating flow (w or v) orthogonal to this direction of travel.

The output signal from an airfoil probe is described by

$$E_p = 2\sqrt{2}SUw, \tag{3.1}$$

where E_p is the probe output voltage. The sensitivity S is proportional to the transformation of a lift force into a voltage by the ceramic strain sensor, and is determined through calibration. Microstructure shear ($\partial w/\partial x$ and/or $\partial v/\partial x$) is obtained from the probe signal by applying the Taylor frozen field assumption

$$\frac{\partial}{\partial t} = U\frac{\partial}{\partial x}\,, \tag{3.2}$$

to the differentiated voltage E_p to give

$$E_s = \frac{\partial E_p}{\partial t} = 2\sqrt{2}G_d S U^2 \frac{\partial w}{\partial x}\,, \tag{3.3}$$

where G_d is the differentiation gain, E_s is the output from the analog differentiator, and

$$E_s = \frac{20}{2^{16}}N. \tag{3.4}$$

N is the recorded bit count and 20 Volts is the full range of the 16-bit A/D converter.

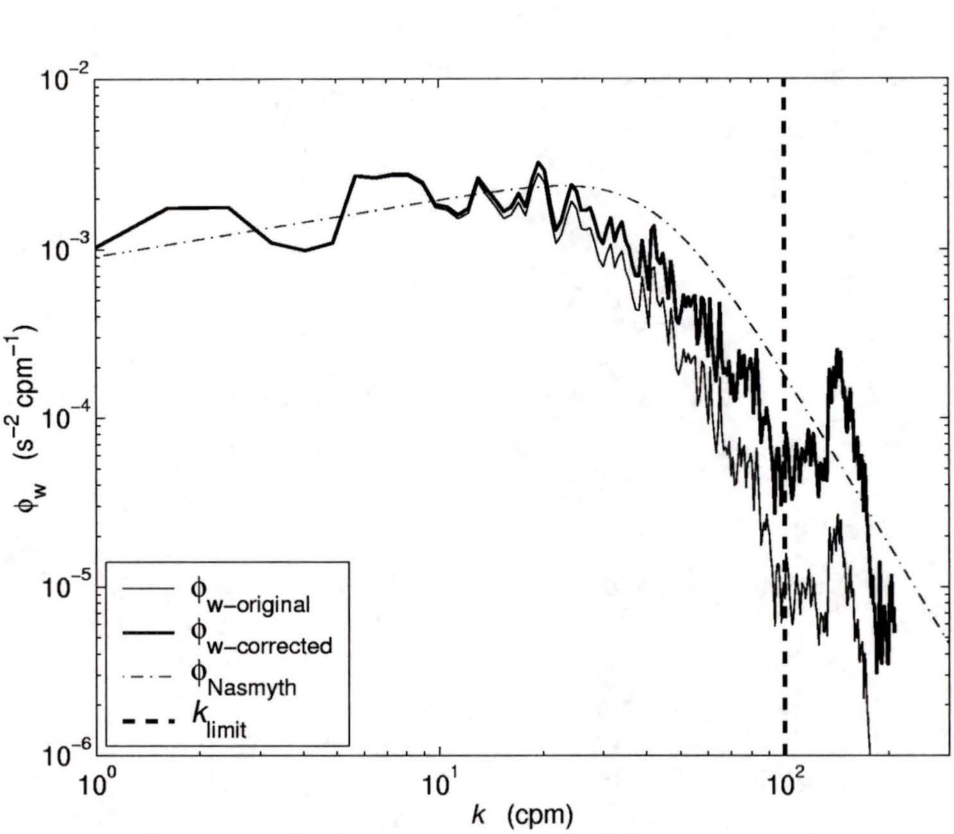

Figure 3.3: Shear probe spectra for 10 seconds of both original (thin solid line) and corrected (thick solid line) data. Nasmyth's theoretical spectrum for $\epsilon = 1.2 \times 10^{-6}$ W kg^{-1} and the upper wavenumber limit for integration are also included for reference.

Converted shear probe voltages yield instantaneous values of $\partial w/\partial x$. A common form of contamination in these signals is spiking due to collisions with plankton and other solid particles, which, if uncorrected for, have the potential to contribute significantly to the variance of the shear signal (ϵ). An algorithm is applied to all shear signals that isolates and removes erroneous content due to collisions. This algorithm compares a rectified version of the signal to a low-pass filtered version, and identifies spikes through a threshold difference between these series. Data points which exceed this threshold are replaced by a data interval (±5 samples) equivalent to the local mean, which effectively removes the spike and most of the ringing associated with the probe impacting a solid object. Typically, this technique for cleaning probe signals rarely alters more than 1% of the original record.

Under the assumption of local isotropy of the turbulence, the rate of dissipation of turbulent kinetic energy is determined by

$$\epsilon = 7.5\nu\overline{\left(\frac{\partial w}{\partial x}\right)^2} = 7.5\nu\overline{\left(\frac{E_s}{2\sqrt{2}SU^2}\right)^2}. \quad [W\ kg^{-1}] \tag{3.5}$$

In practice, the variance of shear is obtained by integrating the shear spectrum in wavenumber space.

The following data processing steps were required in order to obtain estimates of the dissipation rate from shear probe data. The $\partial w/\partial x$ time series from shear probes were divided into 10 second segments for the computation of power spectra based on 1 second FFT (Fast Fourier Transform) lengths. A limitation imposed by the size of the airfoil probe is its inability to resolve scales of comparable size to its sensing length. To account for this lost variance at high wavenumber due to spatial averaging, shear spectra were then corrected using a single-pole model, which is further discussed in Appendix A (see Fig. 3.3). A check for the spectral minimum identified the transition from signal to noise, and the wavenumber range for integration was adjusted accordingly. A first estimate of the dissipation rate was then made in accordance with Eq. 3.5. Comparison of the highest wavenumber used for the integration, to the Kolmogorov wavenumber ($k_s = (\epsilon/\nu^3)^{1/4}$) gives a measure of the area not captured by the airfoil probe with respect to the Nasmyth Spectrum (Nasmyth 1970), and dissipation is adjusted accordingly. The end result of this process is 10 second average estimates of ϵ used in conjunction with direct estimates of B for calculation of the scaled buoyancy flux R (Eq. 2.12).

3.2.3 Buoyancy Frequency (N)

The Brunt-Vaisala or buoyancy frequency (N) is a primary measure of stability in a stratified fluid. Unfortunately, since N involves estimating the vertical gradient of density, it is not necessarily an easy parameter to measure from a near horizontal measurement path.

The buoyancy frequency can be estimated using

$$N^2 = g\left[\alpha\left(\frac{\partial T}{\partial z} + \gamma\right) - \beta\left(\frac{\partial S}{\partial z}\right)\right], \quad [\mathrm{rad\ s^{-2}}] \tag{3.6}$$

where $\partial T/\partial z$ and $\partial S/\partial z$ are the vertical gradients of temperature and salinity respectively, and γ is the adiabatic lapse rate. To provide the estimates of N^2 used in this work to determine the buoyancy Reynolds number, vertically separated (≈ 2.5 meters) concurrent measurements of temperature and conductivity were made using *Sea-Bird* sensors on the top and bottom masts of the vehicle. Instantaneous salinity values (S') were then calculated from instantaneous estimates of pressure, temperature and conductivity (Lewis and Perkin 1981).

The *Sea-Bird* SBE3 thermometer and SBE4 conductivity cells generate a frequency proportional to the quantities being measured, which is digitized by the acquisition system. Temperature and conductivity estimates are determined from the recorded bit-counts using polynomial relations dependent on manufacturer calibration coefficients (Appendix B). Pre and post cruise calibrations of all *Sea-Bird* thermometer and conductivity cells permit an assessment of the uncertainties associated with estimating N^2. These uncertainties are due to systematic errors associated with calibration of the temperature and conductivity cells, and random errors caused by the technical limitations of the sensors. The systematic error in measurement of temperature and conductivity is the result of calibration drift over time. The *Sea-Bird* SBE3 and SBE4 cells were calibrated by the manufacturer in July of 1999, and again immediately after the cruise in September of 2000. These latter calibration coefficients were used exclusively for estimating temperature and conductivity, and sensor drift determined by comparison of pre and post cruise calibrations are employed here to assess uncertainties in these estimates. By assuming a linear drift between calibrations, the upper mast temperature and conductivity cells exhibit drifts of $2 \cdot 10^{-4}$ °C and $1 \cdot 10^{-4}$ psu per month respectively. Accordingly, the lower mast *Sea-Bird* sensors exhibit drifts of $3 \cdot 10^{-4}$ °C and $2 \cdot 10^{-4}$ psu per month. Since the cruise was almost exactly a month before the post cruise calibrations, these values for drift are assumed to be the range of uncertainty associated with estimates of temperature and conductivity. The ranges of uncertainty associated with their vertical gradients are

$$\triangle_{dT/dz} = 5 \cdot 10^{-4}\ {}^{\circ}\mathrm{C\ m^{-1}} \quad \& \quad \triangle_{dS/dz} = 3 \cdot 10^{-4}\ \mathrm{psu\ m^{-1}} \tag{3.7}$$

and the uncertainty associated with estimates of the buoyancy frequency is thus given by

$$\triangle_{N^2} = g(\alpha \triangle_{dT/dz} + \beta \triangle_{dS/dz}), \tag{3.8}$$

assuming that dz, the vertical distance between sensors, is exactly known and that α, β and γ do not change significantly. The error margin of the square of the buoyancy frequency (N^2), based on these calibrations, is $\triangle_{N^2} \approx \pm 3 \cdot 10^{-6}$ s^{-2}. Therefore, estimates of N^2 that lie within these bounds should be regarded as not significantly different than zero. Increasingly high positive values of N^2 outside this error margin indicate increasingly stable stratification, whereas high negative values of N^2 indicate unstable conditions and tend to occur in convective regions and in regions of intense turbulence.

3.3 Motion Correction

The TOMI is incapable of profiling along a perfect horizontal path. By the very nature of the flow fields that the TOMI encounters, the vehicle is inclined to undergo pitching, yawing and rolling motions, as well as accelerations along all three axes. The vehicle body acts like a high-pass filter to large-scale water motions through entrainment, where the velocity signals of large-scale eddies are heavily attenuated as the vehicle is carried within the eddy. The vehicle begins to slip as the scales of motion become progressively smaller, but can still be heavily influenced by the chaotic flow about it. In order that vertical velocity estimates from the shear probes (w'_p) mounted on the TOMI's nose are those of the turbulence, and not the result of vehicle motions, body velocities (w'_b) must be resolved and removed from probe signals. Shear probes are oriented orthogonally to one another with respect to their central axis for the measurement of velocity components w_p and v_p. To properly account for vehicle motion contamination in these velocity signals, w'_b and v'_b calculated from inertial sensors in the nose cone are extrapolated to the probe tips forward of vehicle nose. Addition of w'_b and v'_b to the instantaneous vertical (w'_p) and horizontal (v'_p) estimates of velocity from shear probes effectively removes these motions from the probe signals, revealing the true instantaneous velocity field of the turbulence (w').

The following overview of establishing vehicle orientation and body motions based on inertial measurements is drawn from work done by Wolk (1997). His development of algorithms that determine the instantaneous position and velocities of the TOMI have greatly facilitated the work presented here.

3.3.1 Vehicle Orientation

The TOMI is regarded as a rigid body. Hence, to describe vehicle motions in three dimensional space, the three rectilinear accelerations (A_x, A_y, A_z) along the x, y and z axes and the three angular velocities (ω_x, ω_y, ω_z) about them must be known. These parameters are provided by three high performance linear servo accelerometers and three micromachined quartz angular rate sensors mounted orthogonally in a compact package inside the nose cone.

In order to describe the orientation of the vehicle at any given time, Wolk (1997) defined two reference frames. They are, with slight variation

- an inertial earth-fixed coordinate system (EF) which is defined by the set of coordinate axes X, Y and Z, where Z is defined as positive upwards (towards the surface).
- a body-fixed coordinate system (BF) which is defined by the set of axes x, y and z, where x is along the main axis of the body and is positive forward, y is across the body and is positive to starboard, and z is the vertical component, positive upwards.

At any given point, the BF relative to the EF can be described by a set of Euler angles (θ, ϕ, ψ), where θ is the pitch angle describing rotations about Y, ϕ is the roll angle describing rotations about X, and ψ is the yaw angle describing rotations about Z (Etkin 1972). Accelerometer signals are dominated by gravitational acceleration at very low frequencies ($f < 0.1$ Hz), and exhibit inertial body accelerations at higher frequencies (Moum and Lueck 1985). Gyro signals on the other hand remain insensitive to inertial accelerations and have a useful bandwidth to 6 Hz, beyond which all gyros signals reach the noise floor (Fig. 3.4). By employing a recursive blending procedure developed by Wolk (1997), accelerometer and gyro signals are combined in such a way that the bandwidths of the Euler angles are extended to 6 Hz, thereby improving their resolution.

Initial estimates θ_i, ϕ_i and ψ_i were determined from low-pass filtered ($f_c = 0.5$ Hz) accelerometer signals according to

$$\theta_i = \arcsin\left(\frac{-A_x}{g}\right), \tag{3.9}$$

$$\phi_i = \arcsin\left(\frac{A_y}{g\cos\theta_i}\right), \tag{3.10}$$

$$\psi_i = \text{compass heading}, \tag{3.11}$$

where g is the acceleration due to gravity in the body-frame. These initial Euler angles are used to transform angular rates from the gyros (ω_x, ω_y, ω_z) into a first estimate of the Euler rates ($\dot{\theta}$, $\dot{\phi}$, $\dot{\psi}$) based on the transformation

$$\begin{bmatrix} \dot{\theta} \\ \dot{\phi} \\ \dot{\psi} \end{bmatrix} = \begin{bmatrix} 1 & \sin\phi\tan\theta & \cos\phi\tan\theta \\ 0 & \cos\phi & -\sin\phi \\ 0 & \sin\phi\sec\theta & \cos\phi\sec\theta \end{bmatrix} \begin{bmatrix} \omega_x \\ \omega_y \\ \omega_z \end{bmatrix} \tag{3.12}$$

These initial estimates for Euler angles and rates are then blended, and the resulting estimate for the Euler angles is recursed back into the transformation shown in 3.12 to further improve the accuracy of θ, ϕ and ψ. With only one recursion, the error in the angle is reduced to 10^{-3} degrees (Wolk 1997).

Fig. 3.4 shows the spectra from A_x and ω_y, which, when combined, provide an instantaneous estimate of the pitch angle (θ). The first panel (left) shows spectra from raw signals that have been converted to physical units, and then resampled to 128 samples per second. The accelerometer signal shows noticeable gravitational content below $f < 0.5$ Hz, which masks inertial accelerations at these lower frequencies, and inertial accelerations above $f = 1$ Hz. The gyro signal indicates that the most significant pitching is taking place in the vicinity of $f = 0.1$ Hz, and that the noise floor is reached by $f = 6$ Hz. The middle panel shows the resulting spectra for A_x and ω_y after the accelerometer signal is low-pass filtered at 0.5 Hz to provide the initial estimate θ_i, and the gyro signal is high-pass filtered at $f_c = 1/350$ Hz to remove

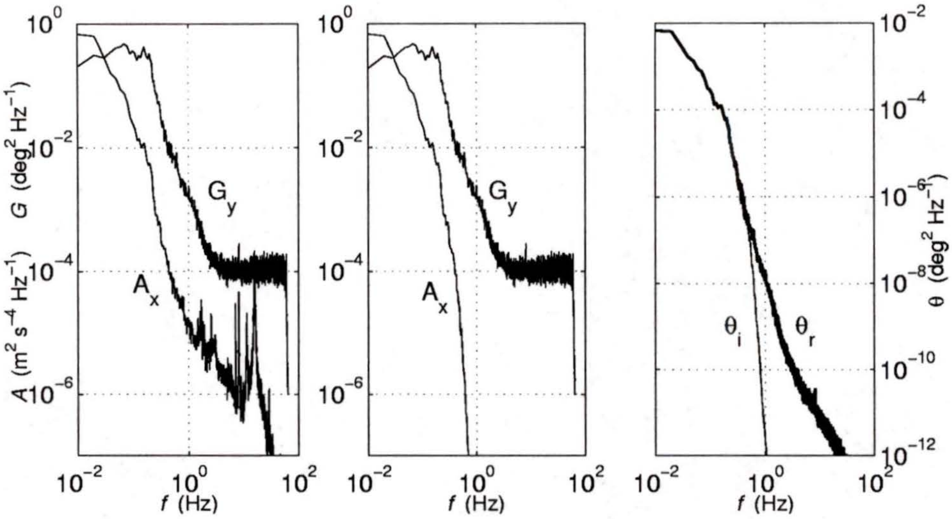

Figure 3.4: Accelerometer and gyro data used to calculate the pitch angle θ (Left panel). Signal spectra after low-pass filtering the accelerometer signal at 0.5 Hz and high-pass filtering the gyro signal at 1/350 Hz (Middle panel). The increased resolution of the pitch angle estimate (θ_r) after employing the recursive technique to blend both signals (Right panel).

spurious content due to low-frequency drift. The right panel shows the resulting estimates for θ based on (i) the low-pass filtered accelerometer signal used for the initial estimate θ_i, and (ii) the recursive technique which uses primarily gyro data (θ_r).

Inertial accelerations (a_x, a_y, a_z) used to estimate body velocities are extracted from the original accelerometer signals (A_x, A_y, A_z) by subtracting the component of gravity that arises from the vehicle's orientation (θ and ϕ), such that

$$a_x = A_x + g\sin\theta, \qquad [+\text{ forward}] \tag{3.13}$$

$$a_y = A_y + g\sin\theta\sin\phi, \qquad [+\text{ to port}] \tag{3.14}$$

$$a_z = A_z + g\cos\theta\cos\phi, \qquad [+\text{ upwards}] \tag{3.15}$$

where a_z is used to calculate the instantaneous vertical velocity of the instrument body (w_b') at any given time. The expressions in equations 3.13 to 3.15 show that inertial accelerations are given by adding, rather than subtracting, the accelerometer signal (A_x, A_y, A_z) to the gravitational component of acceleration based on the Euler angles. This apparent contradiction is the result of the chosen sign convention, where a vertical deviation towards the surface is considered positive. Since gravity is acting towards the bottom, and hence is negative ($g = -9.81$ m s^{-2}), addition of these signals effectively removes the gravitational component of acceleration due to vehicle orientation from the accelerometer signal.

3.3.2 Body Velocity (w_b)

The inertial accelerations of the vehicle are measured from 32 centimeters behind the airfoil probe tips. In order to estimate the degree to which body motions contaminate vertical velocity measurements from airfoil probes, inertial acceleration estimates need to be extrapolated to the probe tips. The reference accelerations at the mounting points of the accelerometers ($\underline{a} = (a_x, a_y, a_z)^T$) are projected to any point P on the instrument according to

$$\underline{a}_p = \underline{a} + \underline{\omega} \times (\underline{\omega} \times \underline{r}) + \frac{d\underline{\omega}}{dt} \times \underline{r}, \tag{3.16}$$

where $\underline{a}_p$ represents the inertial accelerations of all three components at point P, and $\underline{\omega} = (\omega_x, \omega_y, \omega_z)^T$ are the angular rates measured by the gyros. The length vector $\underline{r} = (r_x, r_y, r_z)^T$ corresponds to distances in x, y and z from the sensors to point P. The vertical accelerations of the body at the probe tips (a_t) are estimated from measurements of $\underline{a}$ and $\underline{\omega}$, using

$$a_t = a_z + \omega_x^2 r_z - \omega_x \omega_z r_x - \omega_y^2 r_z + \omega_y \omega_z r_y + \dot{\omega}_x r_y + \dot{\omega}_y r_x, \tag{3.17}$$

where a_z represents the vertical (inertial) accelerations of the body, $r_x = 31.9$ cm, $r_y = 1.5$ cm and $r_z = 2.6$ cm. Eq. 3.17 describes the vertical accelerations experienced by the probe tips in the body-frame (BF) coordinate system. These estimates are transferred to the earth-frame (EF) of reference through the transformation $A_t =$

$a_t \cos\theta \cos\phi$.

Integration of A_t over an appropriate time interval provides a time series of the vertical velocities experienced by the body (w_b), i.e.

$$w_b = \int_0^{t_i} A_t \, dt, \tag{3.18}$$

where the integration time t_i is dependent on flux timescales (see Section 3.4.1). The final signal conditioning step for body velocity estimates is the application of a zero-phase shift high-pass filter with a cut-off frequency of 0.02 Hz. This choice of cut-off is based on low frequency limitations imposed by airfoil probes (Section 3.4.5), and is applied to body velocity time series in order to maintain similar bandwidths between these signals. Also, high-pass filtering effectively demeans the body velocity signal given in Eq. 3.18, resulting in the ultimate goal, a time series of instantaneous body velocity (w_b').

3.4 Flux Parameters

3.4.1 Vertical Velocity (w)

The direct measurement of vertical fluxes requires the resolution of turbulent velocity fluctuations. The airfoil probe not only resolves small scales for the estimation of dissipation rate, but also measures the low wavenumbers associated with vertical fluxes of heat and salt. For Sansum Narrows, these wavenumbers are on the order $1 - 0.02$ cpm, which corresponds to length scales of $0.2 - 8.0$ meters. As previously discussed (Eq. 3.3, 3.4), the velocity gradient from an airfoil probe is given by

$$\frac{\partial w_p}{\partial t} = \frac{20}{2^{16}} \frac{N}{2\sqrt{2}SUG}. \tag{3.19}$$

The vertical component of velocity is provided through the application of an anti-derivative filter to $\partial w_p / \partial t$ over an appropriate time interval, where

$$w_p = \int_0^{t_i} \frac{\partial w_p}{\partial t} dt. \tag{3.20}$$

This integration is carried out in the time domain through the application of a single-pole low-pass butterworth filter to a scaled version of $\partial w_p/\partial t$ (Wolk and Lueck 2001), where

$$\int s(t)dt \Leftrightarrow \frac{1}{2\pi jf}S(f) \tag{3.21}$$

represents the Fourier transformation of the shear probe signal $s(t)$ to its Fourier transform $S(f)$. The scaled transfer function $H(f)$ of the single-pole filter is of the form

$$H(f) = \frac{k}{1 + jf/f_c}, \tag{3.22}$$

where $k = 1/2\pi f_c$ (from Eq. 3.21), and acts as an integrator of $s(t)$ because

$$\underbrace{H(f) \rightarrow \frac{1}{2\pi jf}}_{f>>f_c} \quad \& \quad \underbrace{H(f) \rightarrow k}_{f<<f_c}. \tag{3.23}$$

Wolk and Lueck (2001) equate (3.22) at low frequencies with the transfer function of a t-second running average filter in order to determine the best value for f_c, the integrating cut-off frequency, where

$$f_c = \frac{1}{2.3t_i}. \tag{3.24}$$

Their choice for t_i is 50 seconds (Eq. 3.20), which means $f_c = 0.009$ Hz, and $k = 18$ Hz^{-1}. The integration time t_i must be both long enough to capture the longest timescales expected and short enough such that error accumulation due to spurious low-frequency temperature effects in the probes can be avoided. The largest expected overturns (based on the Ozmidov length-scale) in Sansum Narrows contributing to vertical mass transport are on the order $5 - 10$ meters ($\lambda = 31 - 62$ m), requiring that for a mean travel velocity of $\overline{U} = 1$ m s^{-1}, the integration time must be at least $t \approx \lambda/\overline{U} \approx 60s$. In order to capture the largest scales contributing to fluxes in the Narrows, $t_i = 100$ s was chosen, and vertical velocity w_p was extracted from $\partial w_p/\partial t$ through the multiplication of the time series by $k = 37$ Hz^{-1}, followed by the low-pass filtering of the product with a 1^{st} order Butterworth filter with cut-off frequency

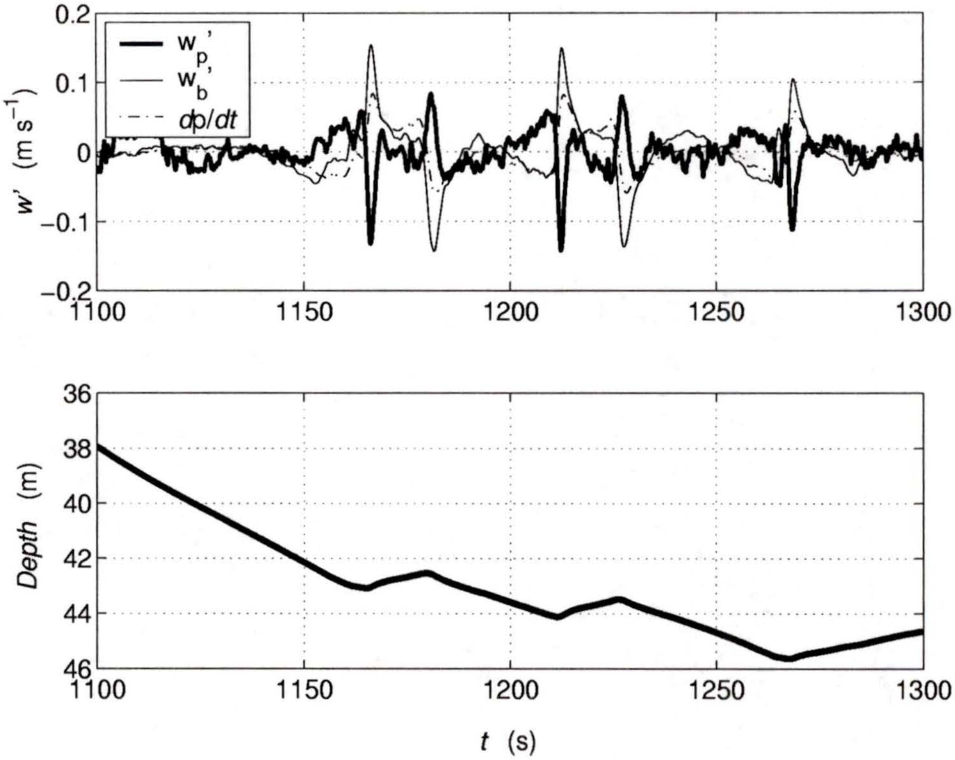

Figure 3.5: The upper panel shows time series of vertical velocity as measured from a probe (w'_{p}), and vertical body velocity derived from inertial sensors (w'_{b}). The lower panel is the associated depth record, which coincides well with estimated body velocity w'_{b}.

$f_c = 0.0043$ Hz.

Wolk and Lueck (2001) found temperature contamination in airfoil probe signals at low wavenumber that limited t_i to 60 s, and required high-pass filtering at 0.03 Hz. The newer materials and design of the probes used in this study are less conductive to heat than those employed by Wolk et al., and as such the probes exhibited only occasional contamination at the lowest resolved wavenumbers. The most significant contamination resided between $0.01 - 0.02$ cpm, and hence all probe signals are high-pass filtered at 0.02 Hz with a zero-phase shift 4^{th} order Butterworth filter, limiting the resolution of flux scales to 0.02 Hz (≈ 0.02 cpm). The application of this high-pass filter to the velocity signal effectively removes the mean, resulting in a time series of instantaneous vertical velocity fluctuations (w'_p). These estimates are then oriented to the Earth Frame (EF) of reference through the transformation $w'_p = w'_p \cos\theta \cos\phi$. The resulting estimate of w'_p is a measure of environmental velocity fluctuations in addition to fluctuations due to body motions (w'_b). Addition of these time series result in a contamination-free estimate of turbulent vertical velocity fluctuations (w'), which can be used for calculating vertical fluxes.

Fig. 3.5 shows a 200 second segment of probe and body velocity data (upper panel). The lower panel is the vehicle depth record, and the dashed line in the upper panel corresponds to the rate of change of pressure (depth). Coherence between the rate of change of pressure (dp/dt) measured at mid-body and w'_b measured near the nose (thin line) demonstrates that body velocities calculated from inertial sensors are reasonable when compared to measured depth changes. For obvious motions at the nose, we see an accompanying change in vehicle depth as a result. In addition, the w'_b and w'_p (thick line) signals appear to be anti-correlated for this data segment, indicating the probe signal is heavily contaminated by pitching motions at the nose of the vehicle. Addition of these signals provides a measure of vertical velocity fluctuations due to the turbulence alone.

3.4.2 Temperature (T)

The high resolution temperature measurement is made using two *Thermometrics* FP07 thermistors, located above and below the cluster of airfoil probes (Fig. 3.2). As with the pressure signal, the signal from each thermistor is combined with its derivative before sampling in order to improve signal resolution (Mudge and Lueck 1994). The enhanced temperature signal is extracted from the combined signal through the application of a 1^{st} order Butterworth filter with cut-off frequency $f_c = 1/2\pi$. A *Sea-Bird* thermometer located approximately 10 centimeters aft of the thermistors serves as a calibration tool. The signals from both thermistors are linearly regressed against the *Sea-Bird* sensor, and the spatial separation between sensors is compensated for by shifting the thermistor signals backwards by $0.10/\overline{U}$ seconds.

In order to maintain the phase properties between vertical velocity fluctuations and temperature, thermistor signals are high-pass filtered with the same integrating filter applied to airfoil probe signals. The final processing step for thermistor signals is the application of a high-pass, zero-phase shift filter with a cut-off frequency of 0.02

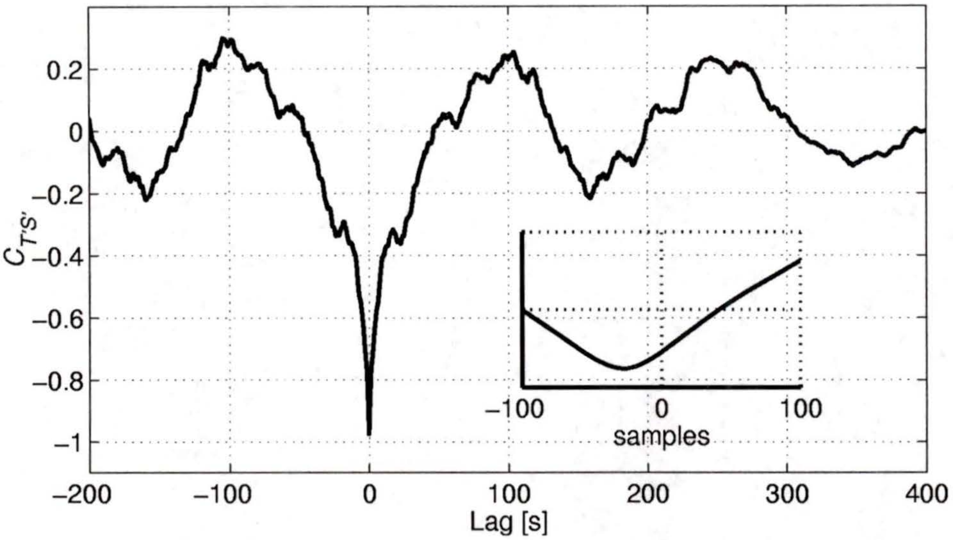

Figure 3.6: The cross-correlation function of temperature from a thermistor and salinity from the nose mounted *Sea-Bird* conductivity cell. Inset is a closer view of the negative peak with respect to sample points, which indicates that salinity measurements lag thermistor signals by approximately 25 points.

Hz. This filtering of the temperature signal ensures that velocity and temperature spectra are confined to the same lower wavenumber limit. An additional effect of this filter is the signal mean is removed, which results in a time series of instantaneous temperature fluctuations (T').

3.4.3 Salinity (S)

Salinity fluctuations used for flux estimates are extracted from conductivity measurements made by a *Sea-Bird* conductivity cell, located adjacent to the temperature cell used for calibrating thermistors. The salinity estimate requires concurrent measurement of temperature and pressure, along with conductivity, and was calculated using the polynomial expressions in Appendix B.

The largest obstacle associated with correlating w' and S' signals in our configuration is establishing a robust means of compensating for the spatial separation between these two measurements. The calibrated thermistor signals (T) serve as the best tool for determining how salinity measurements lag w' made at the nose. For each FFT used in the calculation of the buoyancy term (see Section 3.4.4), the cross-correlation for T and S was computed. The expectation is that typically these signals are anti-correlated, and therefore an indication of the time lag between thermistor and salinity measurements is provided by the location of the nearest negative peak to zero of the cross-correlation function (Fig. 3.6). The salinity time series was then shifted backwards by this lag in order that salinity measurements and velocity estimates from the probes coincided. This shift was typically $0.15 - 0.30$ seconds, and is slightly longer than it would take water to travel the distance between the instruments. In all likelihood the additional plumbing which guides water past the *Sea-Bird* thermometer and into the conductivity chamber is the reason for this additional time lag. The salinity time series then underwent the same high-pass filtering as applied to the thermistor signals.

3.4.4 The Buoyancy Term (B)

The buoyancy term is related to the average heat flux ($\overline{w'T'}$) and salt flux ($\overline{w'S'}$) by

$$B = \frac{g}{\rho}\overline{w'\rho'} \;=\; -g(\alpha\overline{w'T'} \;-\; \beta\overline{w'S'}), \tag{3.25}$$

where α is the thermal expansion coefficient, and β the saline coefficient of contraction. Average heat and salt fluxes are estimated by the covariance method, which requires the integration of w', T', and S' co-spectra over the appropriate wavenumber range. The co-spectra are given by

$$C_{w'T'}(k) = Re\left\{\frac{\Phi_w^*(k)\Phi_T(k)}{Nf_N}\right\} \quad \& \quad C_{w'S'}(k) = Re\left\{\frac{\Phi_w^*(k)\Phi_S(k)}{Nf_N}\right\}, \tag{3.26}$$

where Φ represents the spectrum and the subscript indicates for which signal, the $*$ symbol represents the conjugate of the FFT, N is the number of samples, and f_N is the Nyquist frequency. The average estimates for the heat and salt flux are then evaluated according to

$$\overline{w'T'} = \int_{k_1}^{k_2} C_{wT}(k)dk \quad \& \quad \overline{w'S'} = \int_{k_1}^{k_2} C_{wS}(k)dk, \tag{3.27}$$

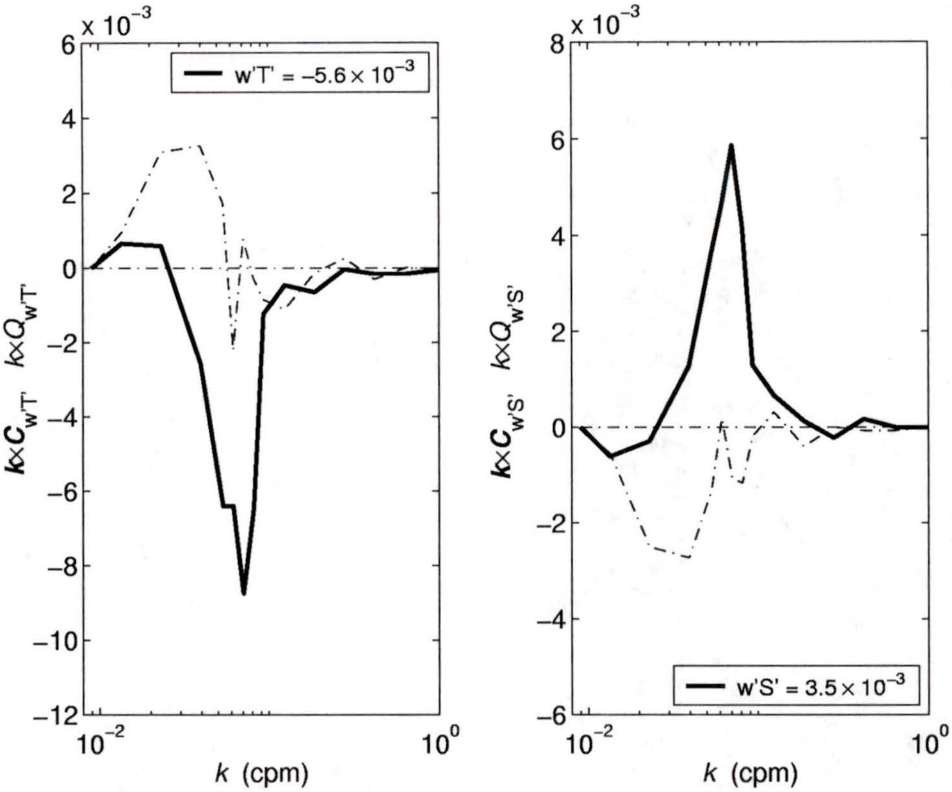

Figure 3.7: Examples of co-spectra and quad-spectra (Eq. 3.27) in variance preserving form. Heat flux ($\overline{w'T'}$) and salt flux ($\overline{w'S'}$) estimates are determined by integrating the co-spectra over the appropriate wavenumber range. The wavenumber bandwidth of each co-spectral estimate is determined by dividing frequency by average velocity ($k = f/\overline{U}$).

where k_1 and k_2 define the wavenumber range over which fluxes of heat and salt are occurring ($k_1 \approx 0.015$ and $k_2 \approx 1$)(Fig. 3.7). The buoyancy term is then computed using Eq. 3.25, and has units $m^2\ s^{-3}$ or W kg^{-1}. Positive values for B indicate a downgradient flux and sink for TKE, where light water is forced downwards and denser water from below is upwelled. A negative B indicates a countergradient flux, and a such, a source of TKE, where displaced water masses are restratifying.

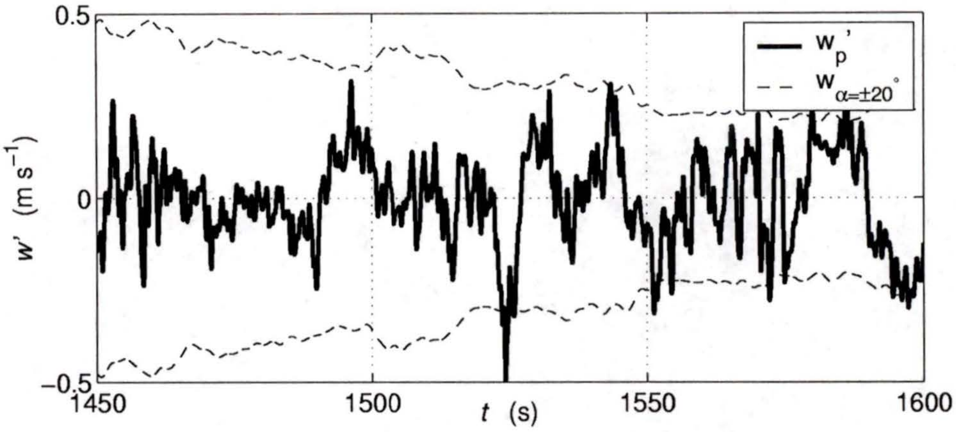

Figure 3.8: An example of airfoil probe signals that exceed the $\alpha < 20°$ criteria, where $w = \pm U \tan(20°)$.

3.4.5 Data Considerations

Careful inspection of time series was carried out with an emphasis placed on identifying regions of downgradient and countergradient fluxes. This priority has resulted in reasonably large differences in the length of flux files, meaning that estimates of B have different degrees of statistical reliability (see Section 4.2.4). Since FFT's used in the calculation of co-spectra are 100 seconds long, some files have buoyancy term estimates based on as few as four co-spectrums. Regardless, it was decided that the demonstration of variability in B was sufficiently important to occasionally warrant the estimation of B from these shorter files. Also, some regions along the length of the selected tows are devoid of an estimate for B/ϵ. The following section addresses a series of factors that affect the suitability of data for flux estimates.

One assumption made when using airfoil probes to determine velocity fluctuations is that the angle of attack is small, i.e. $U >> w$. The angle of attack must be smaller than approximately 20° for the shear probe to respond linearly to cross-stream velocity fluctuations (Osborn and Crawford 1980). Typically, maintaining a small α when the probe is mounted on a profiler is rarely a problem because these instruments move through the water at speeds much greater (≈ 1 m s^{-1}) than the magnitude of the cross-stream velocities ($10 - 20$ cm s^{-1}) (Lueck et al. 1997). However, due to the very high levels of turbulence in Sansum Narrows, $\alpha < 20°$ is not always satisfied.

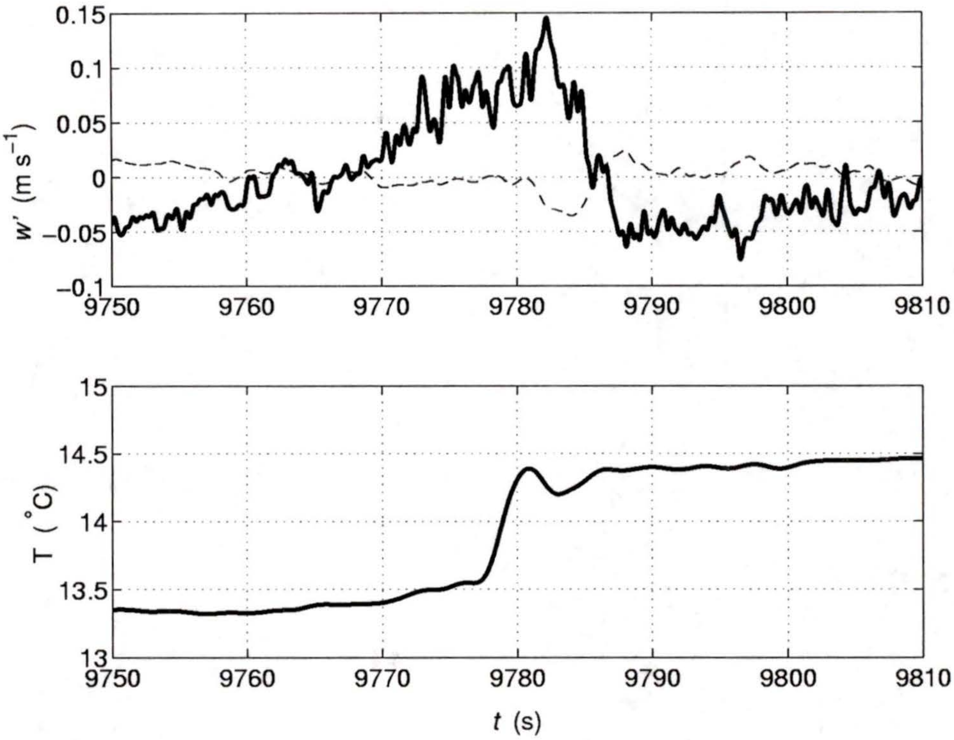

Figure 3.9: The panels above demonstrate an example of the pyro-electric effect. The upper panel is a plot of vertical velocity from a shear probe (thick line) and body velocity from inertial sensors (thin dashed line) for a region without turbulence. The lower panel shows a low frequency temperature change as a result of the vehicle rising towards the surface. This temperature change induces a spurious signal in the shear probe, resulting in low frequency contamination up to 0.02 cpm.

As such, any segments of airfoil probe data that exceed this criteria were deemed not suitable for flux calculations (Fig. 3.8).

A recognized problem with airfoil probes is the effect of low frequency temperature changes on probe response. This pyro-electric effect is the result of temperature changes inducing a spontaneous release of electrons within the probe's beam, and manifests itself as spurious content in velocity estimates at lower frequencies. This spurious content at frequencies typically lower than 0.02 Hz is most pronounced during the initial drop of the vehicle from the surface, and during the final retrieval of the vehicle after a tow, as a result of the large temperature gradients found near the surface. The upper panel in Fig. 3.9 is an example of low frequency signal contamination in a probe signal (thick line) due to the large, low frequency temperature change exhibited in the lower panel. The upper panel also shows the body velocity time series (thin dashed line) to demonstrate that the source of the larger probe signals is certainly not instrument motions. The lower panel shows the temperature, and in particular a low frequency increase in temperature from 13.4 °C to 14.8 °C during t = 9770 - 9790 seconds. This pronounced low frequency change in temperature induces a spurious low frequency signal in the airfoil probe signal with a period of approximately 50 seconds. This example corresponds to one of the more obvious instances where temperature has an effect on probe response, and the result is contamination in the probe signal up to $f \approx 0.02$ Hz. Further analysis has yielded that for most tow sections, temperature effects in airfoil probes are limited to $f < 0.02$ Hz. To eliminate this potential source of error in probe estimates of vertical velocity, all signals used in flux calculations are high-pass filtered at 0.02 Hz, which corresponds to a cutoff range in wavenumber space of $0.02 - 0.013$ cpm for typical vehicle speeds of $1 - 1.5$ m s^{-1}.

A further precaution taken with regard to temperature effects is the exclusion of data from tow sections which encompass significant climbs and descents through the water column. The large deviations in temperature experienced during these climbs and descents in the strongly stratified waters of Sansum Narrows are expected to cause spurious low frequency content in probe signals and hence flux estimates. The screening out of these data segments has led to some significant spatial gaps between flux estimates.

In conjunction with co-spectral estimates of the heat and salt flux, quadrature spectra were also computed to provide information about the phase relations between w' and T', and w' and S' (Fig. 3.10). Occasionally, quad-spectra were significantly larger than their associated co-spectra (> 3 times), indicating the existence of significant phase differences between signals, and the likelihood of contamination due to instrument motions or internal waves. The occurrence of relatively large quad-spectra is not that serious when considering their effect on flux estimates, because platform motions and internal waves are unlikely to produce a net flux correlation. Despite this, data segments exhibiting relatively large quad-variance were still screened out due to the likelihood that associated velocity estimates were still somehow compromised.

Along the length of Sansum Narrows there exists a trend in the density field at

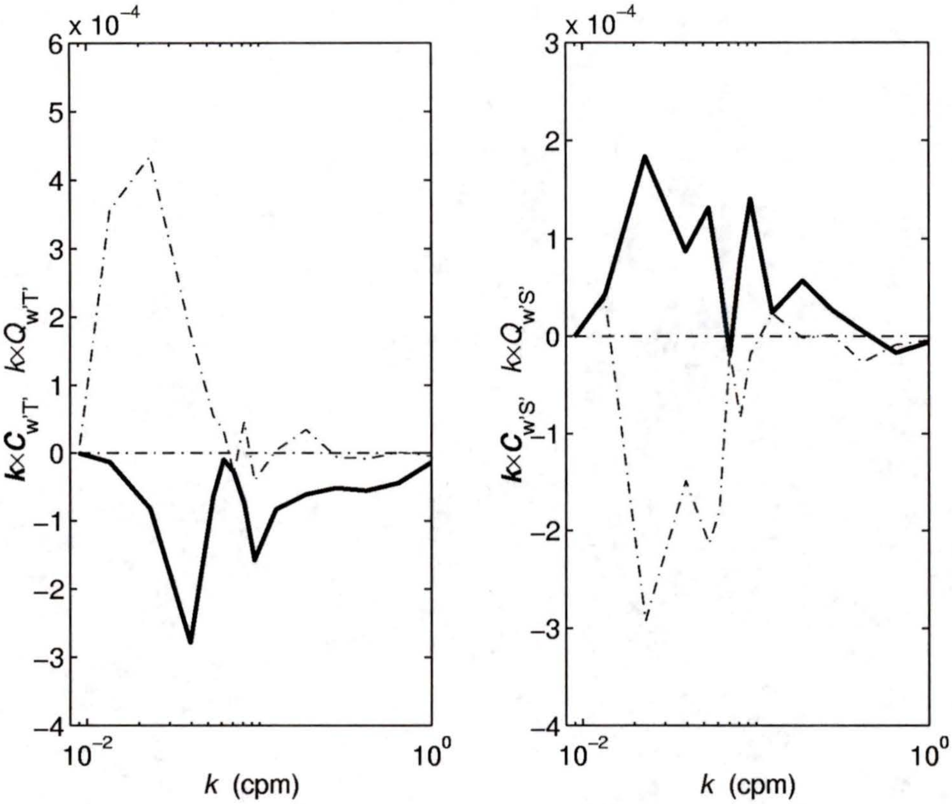

Figure 3.10: Co- and quad-spectra for 800 seconds of velocity, temperature and salinity data. The quad-spectrum from w' and T' signals (dashed line, left panel) contains significantly greater variance at lower wavenumbers than the co-spectrum (thick line). This suggests the probe signal is contaminated by body motions. Spectra of this nature were not included in the analysis.

constant depth, with a general progression towards fresher water heading northwards (Satellite Channel → Stuart Channel), and saltier water in the opposite direction. One must consider whether large sudden changes in density are part of the flux signal, or exist as a background signature that would persist even after the removal of the turbulent velocity field (Gargett and Moum 1995). The latter view is preferred in this case, and the removal of any trend in the density field is accounted for by the high-pass filter applied to temperature and salinity measurements.

File	Day	Time (PDT)	Tide/Current	Peak	Region
SN_2000c_000	11	18:55-20:52	ebb (-2.6 kt)	19:48	Ctd-02→Ctd-04
SN_2000f_000	13	18:29-21:23	ebb (-2.9 kt)	21:12	Ctd-02→Ctd-08
SN_2000g_000	14	05:27-09:17	ebb (-3.0 kt)	07:12	Ctd-02→Ctd-09
SN_2000h_000/3	14	12:44-16:20	flood (+4.4 kt)	14:22	Ctd-08→Ctd-03
SN_2000i_000/4	15	13:09-18:14	flood (+4.4 kt)	14:59	Ctd-09→Ctd-02

Table 4.1: Files selected for calculation of the buoyancy flux (B), dissipation rate (ϵ) and the buoyancy frequency (N).

Chapter 4

Observations

From six days in the vicinity of Sansum Narrows, hereafter SN, ten tows using TOMI were carried out during seven ebb and three flood tides. Screening of all the files associated with these tows resulted in the selection of the five tows outlined in Table 4.1 for the calculation of fluxes. The tidal currents in SN are mixed semi-diurnal, with ebbing flows (North→South) occurring in the morning and evening, separated by a large afternoon flood tide (South→North). A significantly smaller flood tide occurs at night between ebb tides. The file SN_2000c_000 in Table 4.1 corresponds to evening profiling of the southern portion of the channel during the peak flows of an ebb tide. Files SN_2000f_000 and SN_2000g_000 represent south-north tows along the entire length of the channel, during morning and evening tides respectively. The last two tows, files SN_2000h_000 and SN_2000i_000, correspond to north-south tows through the channel during two afternoon flood tides. Since ship handling is considerably easier when the bow is facing upstream, TOMI tows were generally made into the current.

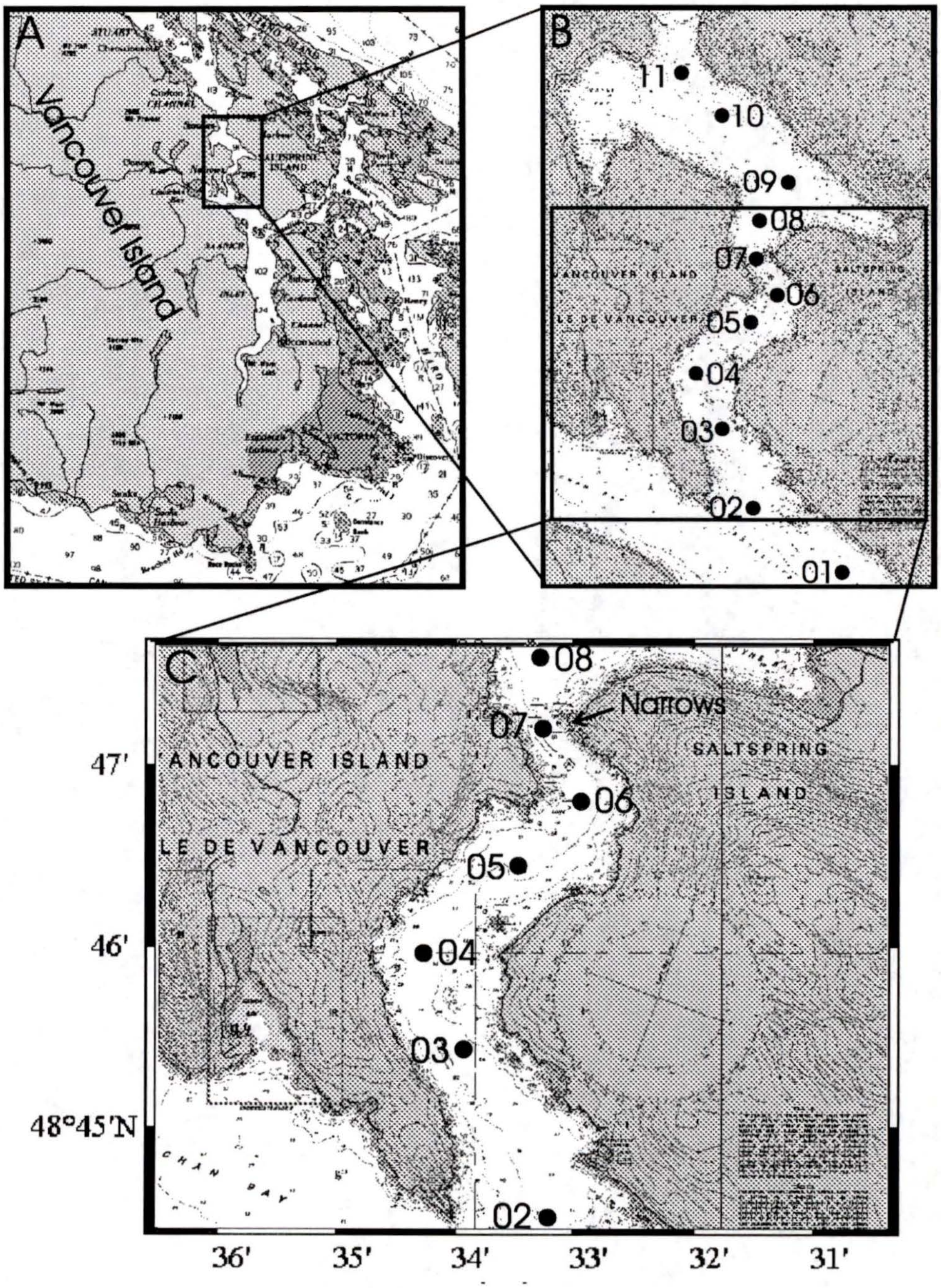

Figure 4.1: (A) Location of Sansum Narrows relative to Vancouver Island. (B) Stuart Channel, Sansum Narrows and CTD stations 01 − 11, and (C) a closer view of Sansum Narrows included to highlight the following features: the location of the "Narrows", the channel bend just south of Ctd-06, and the southernmost bend at Ctd-04.

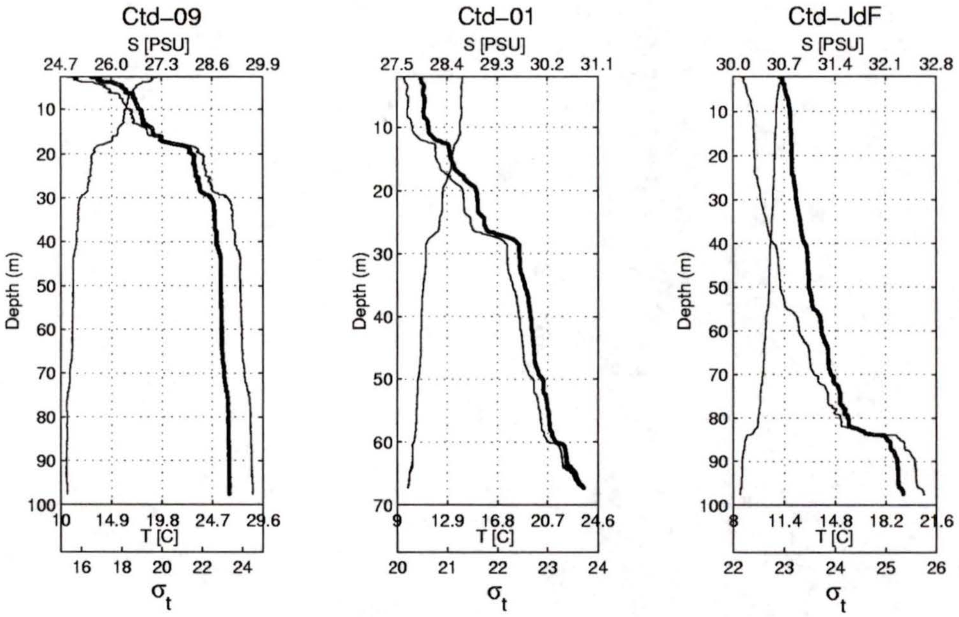

Figure 4.2: CTD profiles for Ctd-09, north of the Narrows, Ctd-01, out in Satellite Channel to the south, and Ctd-JdF, a station located in the Strait of Juan de Fuca, directly south of Haro Strait. σ_t is represented by the thick line.

4.1 CTD Profiles

During periods when TOMI was onboard, CTD profiling was carried out at 16 stations in Satellite and Stuart Channels, and within SN. Station Ctd-01 was situated in Satellite Channel, approximately 3 nautical miles south of the Narrows, and Station Cyd-16 was located in Stuart Channel (opposite Crofton), about 5 nautical miles north of the Narrows (Fig. 4.1B). The term "Narrows" corresponds to the region at the northern end of Sansum Narrows where channel width is less than 500 meters.

From a number of CTD casts in the vicinity of SN, we observe that water properties to the north (Stuart Channel) and south (Satellite Channel) have distinctly different characters. The top 50 meters of water in Stuart Channel (Fig. 4.2, Ctd-09) is heavily stratified as a result of significant inputs of fresh water from both the Fraser River (across Georgia Strait), and from rivers flowing into the channel from the east coast of Vancouver Island. Stuart Channel is defined by a dense grouping of Gulf Islands on its eastern shore, and by Vancouver Island on its western side.

Increased solar input during summer months further enhances the surface stratification through the absorption of heat by this brackish surface layer. Temperatures can exceed 18 °C at the surface ($\sigma_t = 17.5$ kg m^{-3}), but drop to 10 °C below 50 meters. Similarly, salinity increases dramatically from as little as 25 psu at the surface, to in excess of 29 psu at 50 meters. Below this depth, water properties change little ($\sigma_t = 22.8$ kg m^{-3}). Continuous effluent emerging from the Pulp and Paper Mill at Crofton, which empties 165,000 m^3/day into the channel at 38 °C, also contributes to the exceptionally high surface temperatures characteristic of all stations north of the Narrows. Satellite Channel to the south has characteristically colder and saltier water, although it is still less dense than Juan de Fuca water (Fig. 4.2, Ctd-01). At station Ctd-01, four cables off the southwest shore of Saltspring Island, the average surface temperature from CTD casts is approximately 14 °C ($\sigma_t = 20.4$ kg m^{-3}), and salinity is 27-28 psu. By 70 meters depth, temperature falls to below 10 °C, and salinity increases to 31 psu. These properties appear to remain unchanged all the way to the bottom ($\sigma_t = 24.3$ kg m^{-3}).

Fig. 4.3 is a Temperature-Salinity properties plot of CTD casts taken during relatively slack conditions at Ctd-10 north of SN, Ctd-01 south of the SN, Ctd-HS at the mouth of Spieden Channel along the eastern boundary of Haro Strait, and Ctd-JdF from the Strait of Juan de Fuca, south of Haro Strait. The water properties from the stations at each end of the Narrows have similar characteristics up to $\sigma_t = 22.5$ kg m^{-3}, at which point the water from Ctd-01 tends to become more salty than water at Ctd-10. This indicates that mixing within Sansum Narrows is confined to the top 30-40 meters (See Fig. 4.2). This finding is in keeping with channel hydrography, where the shallowest portion of SN is approximately 50 meters. Water properties at Ctd-HS and Ctd-JdF appear to be similar, with a slight freshening at the surface within Haro Strait as compared to south of the Strait. Water property differences between stations in the vicinity of SN and stations more towards the Strait of Juan de Fuca are particularly apparent in the $\sigma_t = 22.5 - 23.0$ kg m^{-3} range. The fact that Ctd-HS and Ctd-JdF casts are distinctly more saline than Ctd-01 for $T < 11$ °C suggests there are additional inputs and processes taking place between Ctd-01 and Ctd-HS.

On August 13th, profiling with TOMI was put on hold for the morning ebb and

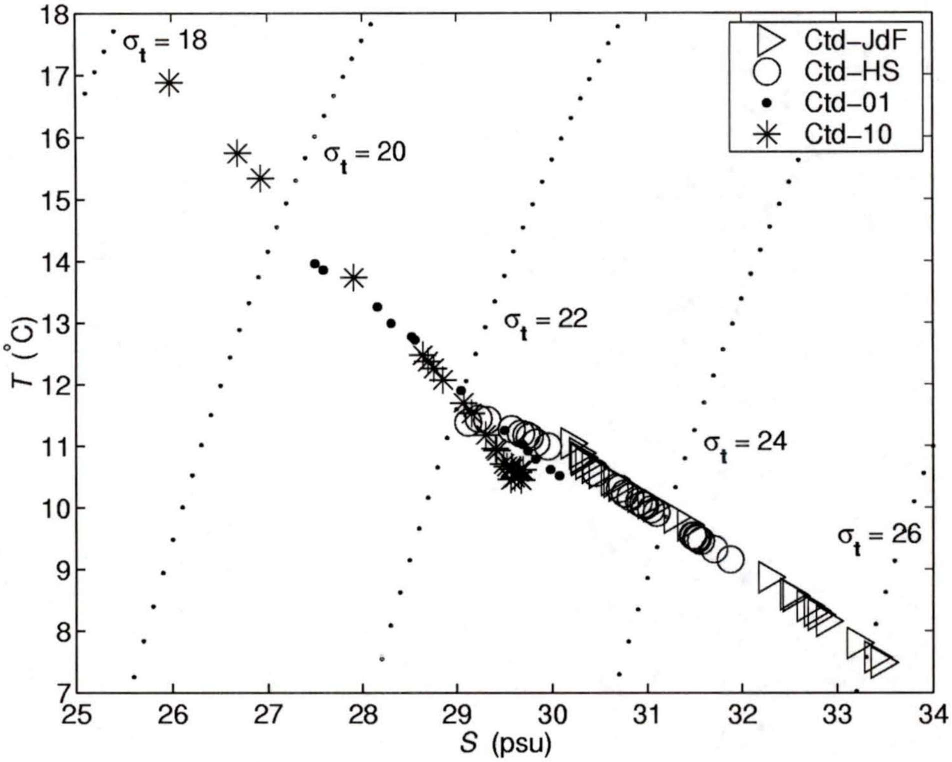

Figure 4.3: T-S plot of CTD data taken from south of Haro Strait (Ctd-JdF), along the eastern shore of Haro Strait (Ctd-HS), in Satellite Channel (Ctd-01), and from north of the Narrows in Stuart Channel (Ctd-10).

afternoon flood tides in order that representative CTD profiles could be taken during peak flows for stations Ctd-01 to Ctd-12. These vertical profiles of density (σ_t) are plotted by station in Fig. 4.4. By superimposing CTD profiles from both ebb and flood tides, we are provided with snapshots of the differences in σ_t for flows in opposite directions. Ebbing flows (thin line) pass southward into the Narrows (Ctd-07) from Stuart Channel, and exhibit regions of overturning which become more pronounced at $5-10$ meters and $20-40$ meters depth by Ctd-06. By Ctd-05, we see denser water ($\sigma_t > 22$ kg m^{-3}) has climbed to 20 meters, leaving only a shallow surface layer where $\sigma_t < 21$ kg m^{-3}. At Ctd-04, we see further "thinning" of the surface layer, and large overturns at $20-30$ meters depth. The Ctd-03 profile is basically unchanged from Ctd-04 in the upper 50 meters, but indicates overturns at various depths above and below well mixed vertical sections. By being a deeper cast than Ctd-04, the Ctd-03

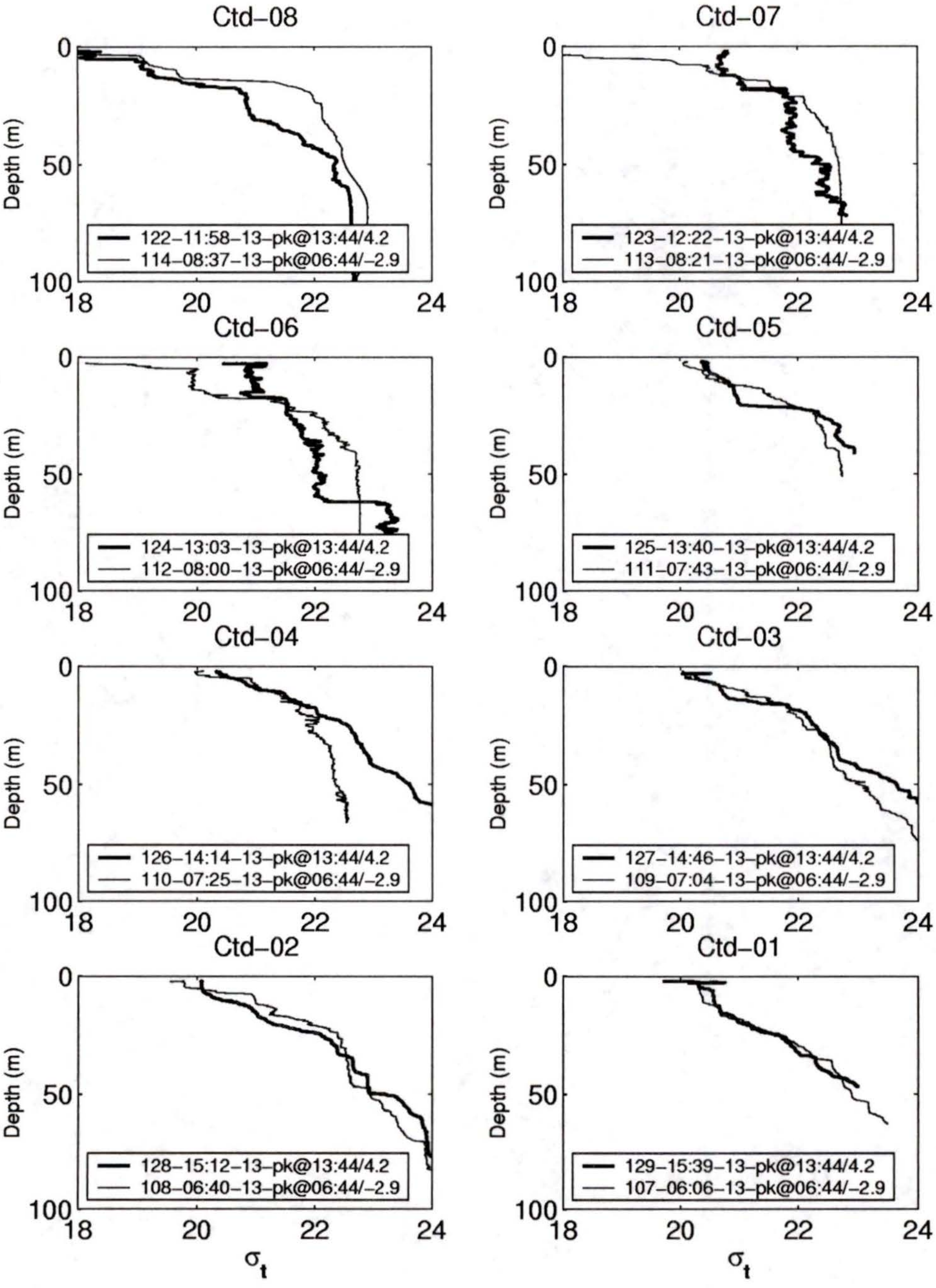

Figure 4.4: Plots of σ_t with respect to depth for CTD Stations 01-08. The thin line represents casts made on August 13th during an ebb tide, and the thicker line corresponds to casts made during the flood tide that same day.

profile also shows an intrusion of denser water below 50 meters. The profile at station Ctd-02 also suggests overturns, but in general closely resembles Ctd-01, which is well out of the Narrows. The peak ebb tide was -2.9 knots at 6:44 am, which corresponds approximately to profile Ctd-02.

Northward flowing flood tide water from Satellite Channel provides similar CTD profiles (thick line) to southward ebb flows at Ctd-01 and Ctd-02. However, by Ctd-03, differences begin to emerge. By Ctd-04, σ_t below 20 meters is almost 1 kg m^{-3} greater for all depths than the ebb tide CTD profile at Ctd-04. By station Ctd-05, a large jump in stratification is observed at $20 - 25$ meters (≈ 1.5 kg m^{-3}), suggesting mixing has occurred in the upper 20 meters of the water column. By Ctd-06, the entire water column exhibits large overturning such that by Ctd-07, the range in σ_t in the top 80 meters has been reduced to $21 - 23$ kg m^{-3}, from $20 - 24$ kg m^{-3} at Ctd-04, one nautical mile to the southwest. Less than half a nautical mile to the north of the Narrows (Ctd-08), we observe a dramatic change in stratification in the top 50 m of the water column, which is very similar to water properties further up the channel and away from intense turbulence. Below 50 meters however, is water of similar σ_t (≈ 22 kg m^{-3}) to that at Ctd-07, which suggests that the denser mixed water travelling northwards through the Narrows dives and continues to mix below the strongly stratified upper layer of Stuart Channel. The peak flood tide was +4.2 knots at 13:44, which corresponds approximately to profile Ctd-05.

To further understand the spatial variability of water properties in Sansum Narrows during maximum ebb and flood tides, temperature and salinity values for regions between stations Ctd-01 to Ctd-12 were approximated through linear interpolation along depth contours (Fig. 4.5, 4.6). For an ebbing current travelling southwards through SN (Fig. 4.5), a number of additional features become more apparent through viewing these properties in this manner. It appears that the most pronounced stratification near the surface occurs at Ctd-10, which is identified by the symbol $\nabla 10$. This stratification, after waters pass through the Narrows, is noticeably reduced by Ctd-04 ($\nabla 4$), where 18 $°C$ water at the surface has been replaced by water 5 degrees colder, and 2 psu more saline. Other noticeable features are pronounced downwelling between Ctd-08 and Ctd-06, a general increase of water density with depth just south of the Narrows, and a $1 - 2$ psu difference between waters north and south of the

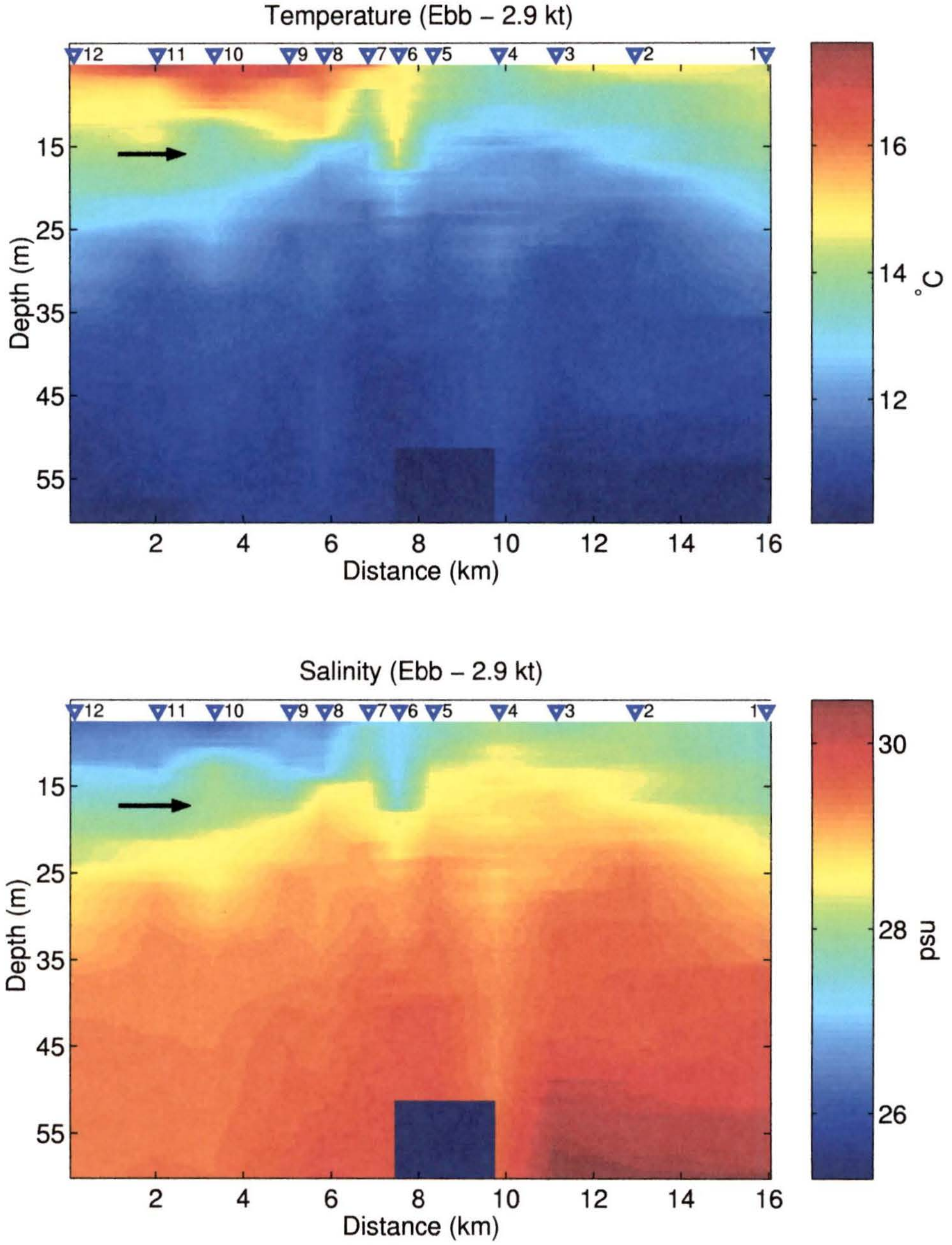

Figure 4.5: Temperature (upper panel) and salinity (lower panel) profiles for an ebb tide in Sansum Narrows determined through linear interpolation between CTD stations 01-12. Distance on the x axis refers to distance away from station 12 in a southerly direction. Arrows indicate the direction of flow, and CTD station locations are marked by the ∇ symbol.

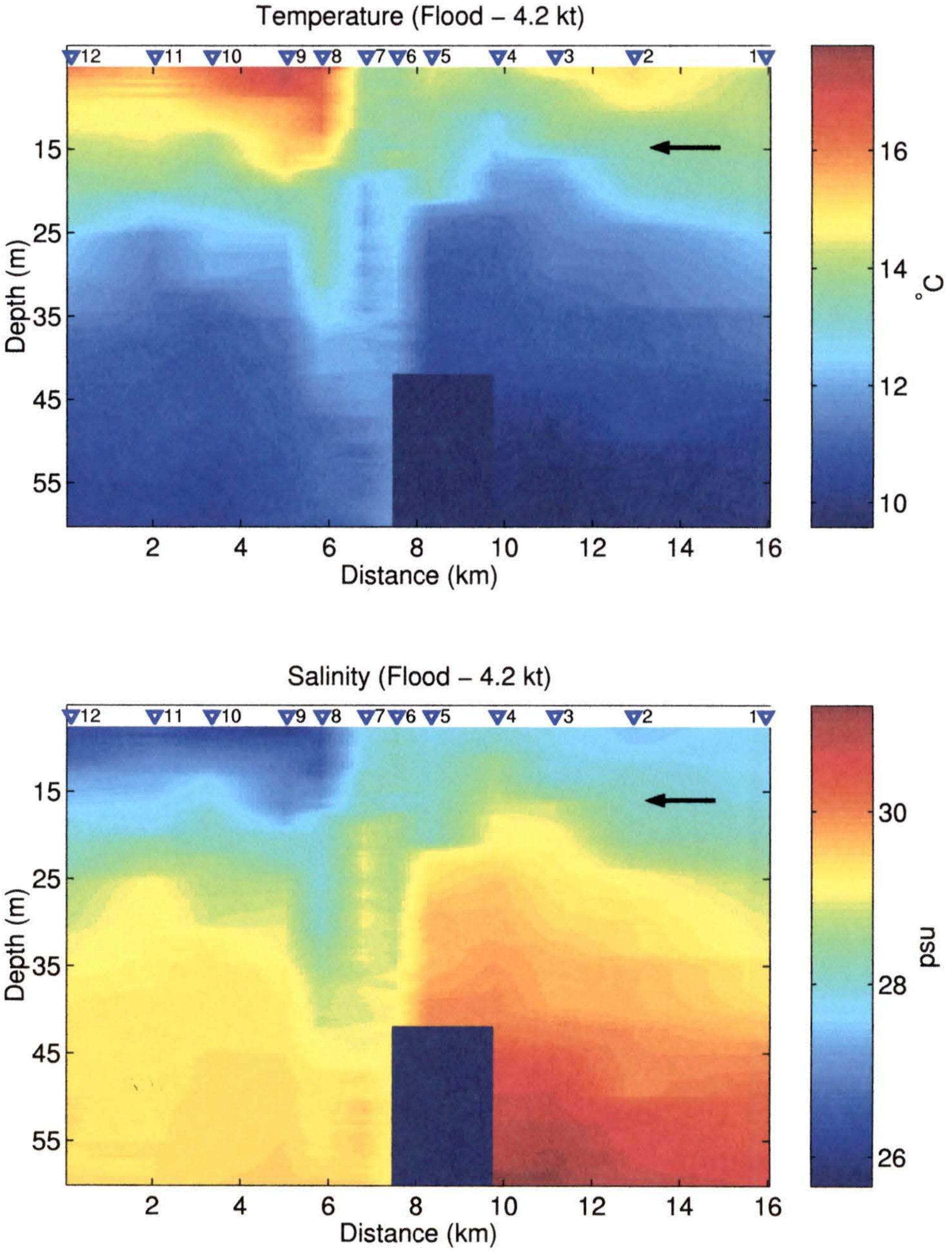

Figure 4.6: Temperature (upper panel) and salinity (lower panel) profiles for a flood tide in Sansum Narrows determined through linear interpolation between CTD stations 01-12. Distance on the x axis refers to distance away from station 12 in a southerly direction. Arrows indicate the direction of flow, and CTD station locations are marked by the ▽ symbol.

Narrows below 50 meters.

For northward flow during a flood tide (Fig. 4.6), we see pronounced mixing occurring as water from Satellite Channel passes over the shallowest part of the channel ($\nabla 5$), and into the narrowest stretch ($\nabla 6 - \nabla 7$). As discussed with reference to Fig. 4.4, this mixed water appears to dive below the heavily stratified surface waters of Stuart Channel immediately north of the Narrows, and finds its equilibrium position in the $15 - 20$ meter depth range. Another noticeable feature, which is particularly pronounced in the salinity profile (lower panel), is a general upward migration of denser water from below as the flow passes over the shallowest portion of the Narrows ($\nabla 5$). It also appears that the most saline water, which resides below 50 meters, is mixed upwards and diluted at the sill between Ctd-04 and Ctd-06. This notion is supported by the $1.5 - 2$ psu drop in salinity found on the downstream side of the sill at the same depth.

4.2 Time Series

4.2.1 Shear, Dissipation Rates & Buoyancy Frequency

Vertical shear ($d\mathrm{U}/dz$) estimates from the ship mounted ADCP did not correspond directly to dissipation rate and buoyancy frequency measurements made by TOMI. A spatial separation of $150 - 200$ meters between these instruments required ϵ and N^2 time series be shifted by an amount determined through comparison of instantaneous shear estimates from airfoil probes and vertical shear estimates from the ADCP. Typically lags of this nature can be accounted for by shifting one series in time relative to the other with the use of tow speed, however, in this case the tow cable length between the TOMI and the ship was constantly being altered, which complicates the time shift since the lag is always different. This difference is not large, however, it was determined that the required shift was more readily provided by comparison of shear estimates from airfoil probes and the ADCP. Once shifted, the time series of dissipation rate, buoyancy frequency squared and pressure were then resampled to coincide with the sample rate of the ADCP. The resampled pressure (depth) record from TOMI was then used to determine five meter vertical averages of $d\mathrm{U}/dz$ (U_z).

Concurrent time series of ϵ, N^2 and U_z allow for the comparison of non-dimensional numbers like the Richardson (Ri) and Froude (Fr) number, to quantities such as ϵ and Re_b, where

$$Ri = \frac{N^2}{(\frac{dU}{dz})^2} \quad \& \quad Fr = (Ri)^{-0.5}. \tag{4.1}$$

The upper panel in Fig. 4.7 is the vertical shear profile generated by the ADCP of southerly flows in Sansum Narrows during an ebb tide. The depth profile corresponding to TOMI's path over the course of the three and a half hour tow is superimposed in white. The tow began in Satellite Channel, and terminated in Stuart Channel about 1 nautical mile north of the Narrows. The average square of vertical shear from the ADCP is plotted in the panel below, along with the dissipation rate (ϵ) and the buoyancy frequency squared (N^2). When comparing estimates of ϵ and N^2 from TOMI to U_z from the ADCP, one must keep in mind that both N^2 and ϵ measurements are made at the depth of the vehicle and do not necessarily reflect water column properties above and below the instrument. Elevated levels of U_z^2 are observed for the first hour of towing as TOMI dissects the bottom portion of a region of fairly pronounced shear (top panel), followed by other regions of enhanced shear at 5500-7000 seconds and again at 9000-10000 seconds as TOMI heads north through the narrowest part of the channel. Dissipation rate estimates remain high over the course of the entire tow, with levels sometimes exceeding 10^{-4} W kg^{-1} at and slightly north of the southernmost bend in the Narrows (Ctd-04), and within the Narrows (Ctd-07). Dissipation rate levels are lower than 10^{-6} W kg^{-1} south of Ctd-02 ($t < 1000$ s) and north of Ctd-08 ($t > 11000$ s). The square of buoyancy frequency reveals a stratified region south of Ctd-04 ($t < 3500$ s) that remains only intermittently stable upstream. N^2 is particularly small and sometimes negative just north of Ctd-04 and again in the shallowest and then narrowest part of the channel ($8000 < t < 10000$ s).

Fig. 4.8 corresponds to data collected during a flood tide on the afternoon of August 14th. The top panel again shows the shear profile generated by the ADCP and the depth profile corresponding to TOMI's path (white line) over the course of five hours of towing into the flooding current. The tow began in Stuart Channel in the vicinity of Ctd-08, and is prematurely terminated in the top panel at the southern

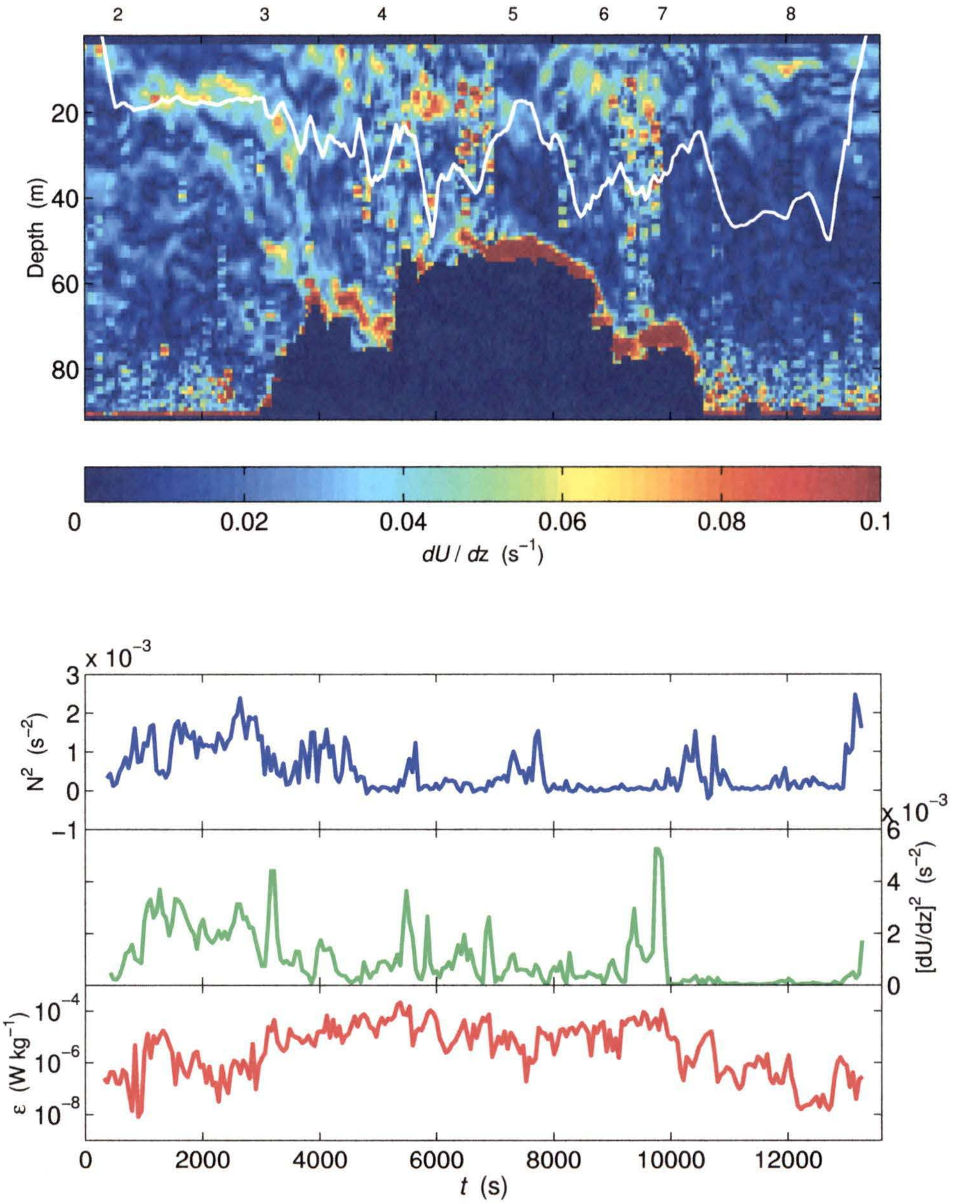

Figure 4.7: The upper panel is a display of vertical shear estimates for an ebb tide from the ADCP, overlain by TOMI's depth profile. As a reference, the numbers above the plot correspond to the general locations of CTD stations 2-8. Plotted in the lower panels are average estimates of the buoyancy frequency squared (N^2), the vertical shear squared ($[dU/dz]^2$) and the dissipation rate (ϵ).

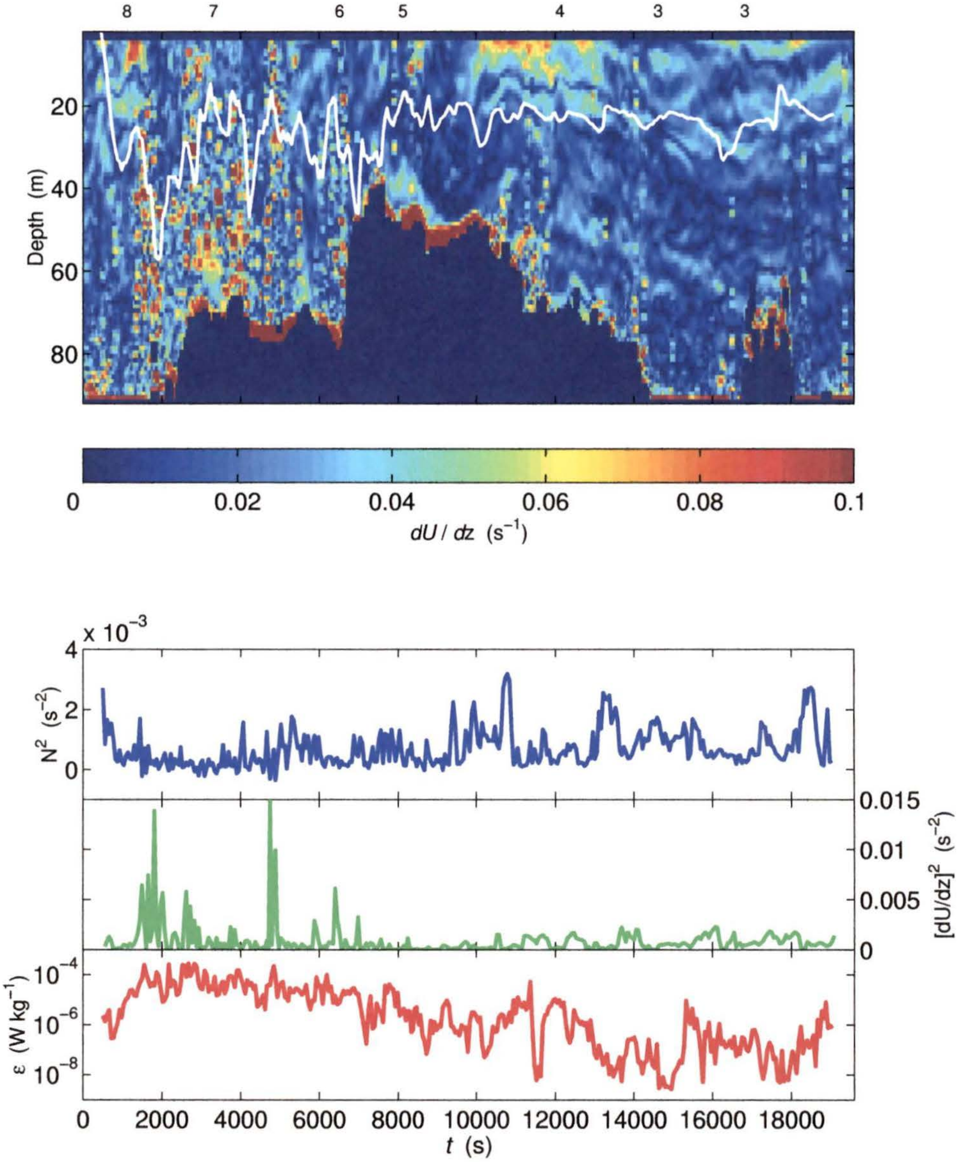

Figure 4.8: The upper panel is a display of vertical shear estimates for a flood tide from the ADCP, overlain by TOMI's depth profile. As a reference, the numbers above the plot correspond to the general locations of CTD stations 3-8. The number 3 appears twice because the ship is circling in the vicinity of Ctd-03. Plotted in the lower panel are average estimates of the buoyancy frequency squared (N^2), the vertical shear squared ($[dU/dz]^2$) and the dissipation rate (ϵ).

extremity of Sansum Narrows (Ctd-02). The lower panels highlight the presence of very high vertical shear levels corresponding to the region within and just north of the narrowest section of Sansum Narrows, while dissipation levels in the same region remain above 10^{-5} W kg^{-1} and occasionally exceed 10^{-3} W kg^{-1} (not the case for this example). ϵ levels begin to decrease upstream in the shallowest portion of the channel (Ctd-05) and drop to below 10^{-7} south of Ctd-04. Values of N^2 corresponding to the high shear levels present in the Narrows are generally low and frequently negative, but stratification becomes more pronounced to the south at Ctd-04, and further upstream.

4.2.2 Velocity, Temperature & Salinity

Comparison of vertical velocity signals from probe and inertial sensor measurements show a tendency for the nose of the vehicle to be heavily influenced by large eddies. The intense turbulence in Sansum Narrows at scales on the order of the full length of TOMI tend to cause pitching motions at the nose which would cause uncorrected airfoil probes to underestimate the contribution made by these scales to heat and salt fluxes. By capturing these motions at lower wavenumbers through inertial sensors (w_b'), the environmental velocity field is properly resolved through the addition of w_b' and w_p' signals. In regions of reduced turbulence, where probe signals are primarily the result of body motions, w_b' and w_p' tend to be in-phase, anti-correlated signals of similar magnitude, which, as expected, when added are close to zero.

Fig. 4.9 shows w_p' and w_b' signals from a region of intense turbulence (top panel), and for a region of relatively low turbulence (panel third from the top). In both cases, w_p' and w_b' signals must be added together to compensate for body motions, but the effect is the opposite for these two regions. For intense turbulence (panel second from the top), w_b' adds variance at low wavenumbers to w_p', which compensates for the perturbation of TOMI's nose in an eddy. In contrast, for the relatively quiet region, the probe signal is mostly due to the effect of body motions associated with tension variations in the tow cable, which is demonstrated in the bottom panel by a resultant signal that has much smaller variance than the original probe signal (bottom panel).

In Fig. 4.10, TOMI is being brought to the surface after a tow northwards through the Narrows. The retrieval of tow cable is temporarily halted and restarted from $t = 50 - 90$ seconds, which is reflected in the vehicle depth and the nose angle (θ),

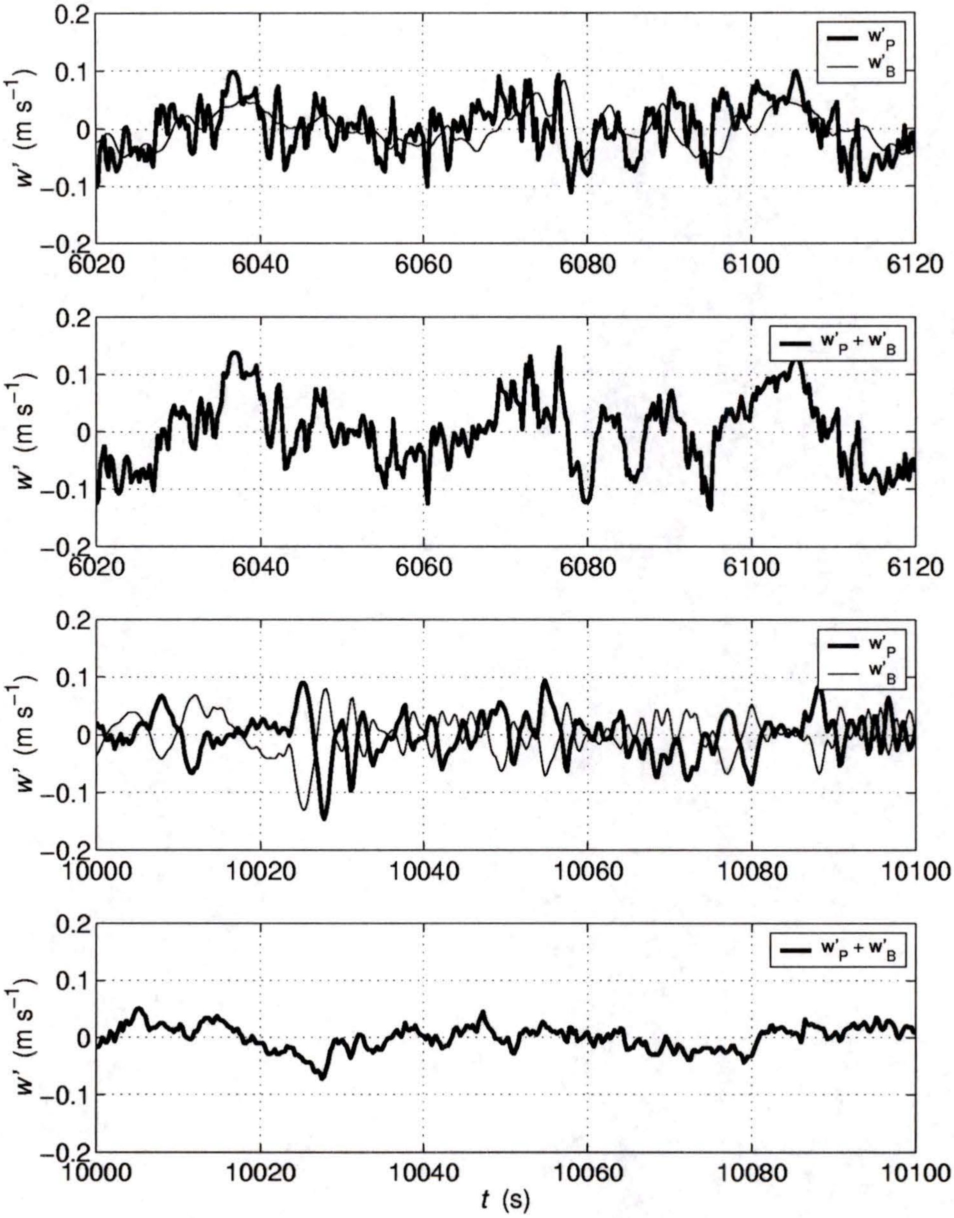

Figure 4.9: Panel 1 (top) shows instantaneous vertical velocity w_p' from a probe (thick line) and body velocity w_b' from inertial sensors (thin line), for a region of intense turbulence. Panel 3 (third from the top) demonstrates the same comparison but for a relatively non-turbulent region. Correction for body motions requires the addition of these signals, and the resulting signals are displayed directly below each case in Panels 2 and 4.

where a negative value for θ corresponds to the angle that a downwards facing nose makes with the horizontal. The estimates of vertical velocity experienced by the body (top panel, thin line) and vertical velocity estimated by the airfoil probe (thick line) agree with the pressure record. A deviation in the nose towards the bottom as tension is released on the tow cable at $t = 50$ seconds ($d\theta/dt < 0$) coincides with a velocity spike towards the surface in the probe ($+w'_p$) and a velocity spike for the body in the opposite direction ($-w'_b$). Forty seconds later we see a sudden retensioning of the tow cable, resulting in a rotation at the nose towards the surface and a pronounced w'_b signal in the same direction, which indicates the body is travelling towards the surface. In keeping with this motion, the probe signal at $t = 90$ seconds shows a pronounced negative spike, indicating this upwards motion at the nose has registered as a downwards velocity signal. The addition of these time series should effectively eliminate the contamination in the probe signal resulting from these sudden forces transmitted via the tow line. Closer examination of w'_p in the upper panel shows that body motions in this example do not account for all the variance in the probe signal, especially at $t = 50$ seconds, where addition of the signals (second panel from the top) still result in a spike in the probe estimate of vertical velocity. As TOMI nears the surface the w'_p and w'_b signals become smaller and almost perfectly anti-correlated ($t > 150$ seconds), indicating probe signals are essentially the result of body motions in this region, and that little turbulence is present.

Examination of corrected w', T' and S' series, and their products $w'T'$ and $w'S'$, has led to the sorting of file segments according to the following three flux types:

- Downgradient transport of heat and salt corresponding to positive fluctuations in vertical velocity and salinity, and negative fluctuations in temperature (or vice versa) (Fig. 4.11). The physical interpretation of downgradient transport is the downward mixing of warm, less salty surface water and the upward transport of colder, more saline bottom water.

- Counter or upgradient transport of heat and salt corresponding to similar signed velocity and temperature fluctuations, and the opposite sign for salinity fluctuations. Countergradient transports are the result of previously mixed water undergoing a re-stratification process due to buoyancy forces, or are due to

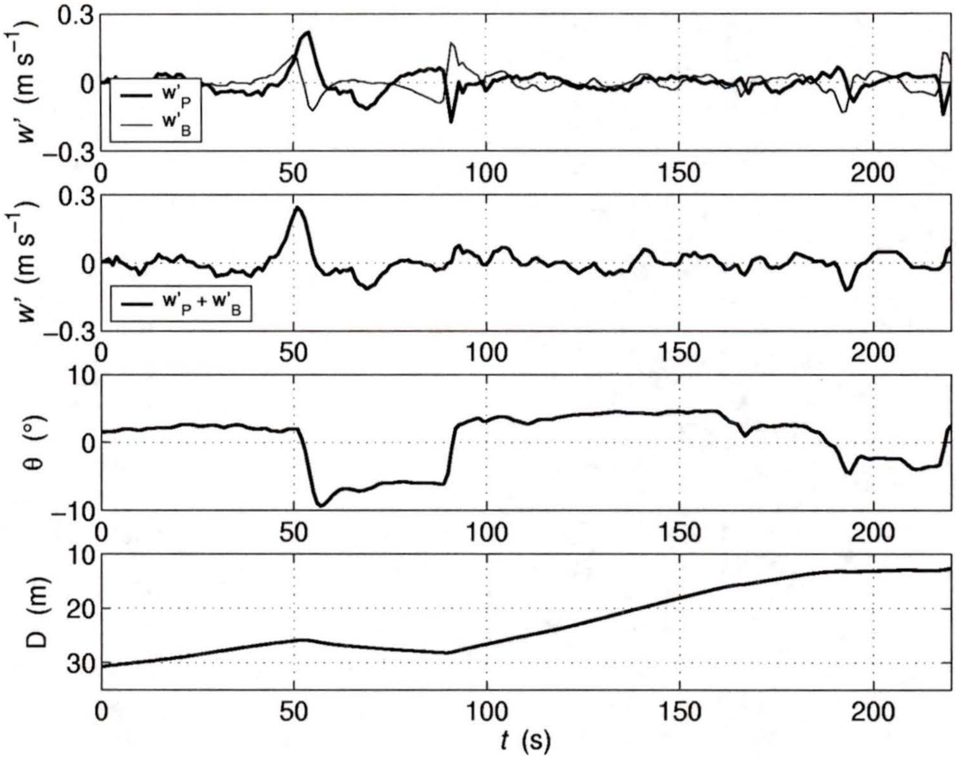

Figure 4.10: Time series of body velocity w_b' (thin line), probe velocity w_p' (thick line), vehicle nose angle θ and depth D. Comparison of w_b' and w_p' in regions of reduced turbulence show that body velocities derived from inertial measurements are adequate for correcting airfoil probe signals contaminated by body motions.

destabilizing buoyancy at a boundary.

- A mixed form for co-spectra, which are a combination of downgradient and upgradient transports. The upgradient fluxes in these cases typically occur at the largest scales (smallest k). A number of calculated co-spectra exhibit some countergradient transport at smaller wavenumbers ($0.02 - 0.04$ cpm), while still producing positive values for the buoyancy term (B).

4.2.3 Heat and Salt Flux Co-spectra

The probes and thermistors were sampled at a rate of $f_s = 512$ samples per second (sps), and low-pass filtered with a cut-off at 200 Hz. Since fluxes of heat and salt

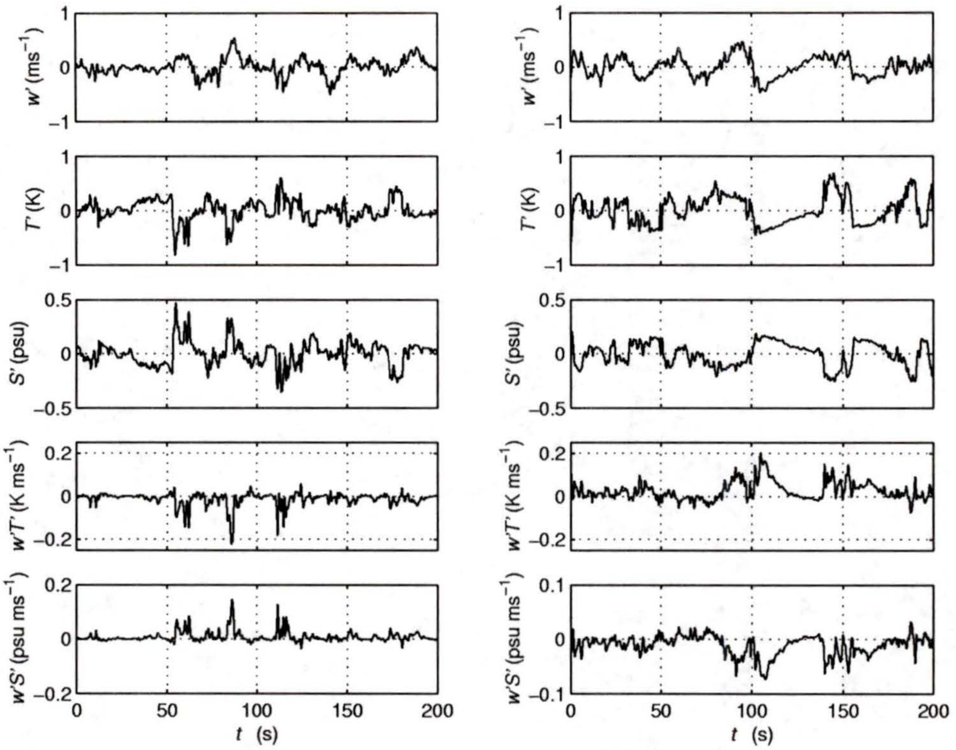

Figure 4.11: Time series of w', T' and S', and the products $w'T'$ and $w'S'$ for a region of downgradient transport (left panels) and countergradient transport (right panels).

occur at wavenumbers well below the Nyquist frequency ($f_N = 256$ Hz), velocity and temperature signals were resampled to 128 sps in order to save computing time, and salinity measurements were resampled from 64 to 128 sps through interpolation. At 128 sps, a typical vehicle speed of 1 m s^{-1} means the potential resolution of flux scales up to 64 cpm ($k = f/U$). However, temperature, vertical velocity and salinity co-spectra fall off above 1 cpm, which indicates that sampling rates need only be adequate to capture wavenumber content up to 1 cpm for fluxes in Sansum Narrows (Fig. 4.12). This means f_s could have been as low as 2-3 sps.

Spectra of corrected velocity, temperature and salinity fluctuations were established using the periodogram technique, in conjunction with 50% overlap. Periodograms were calculated using consecutive 100 second intervals of data, which are sufficiently long FFT lengths to ensure the entire bandwidth of the signal is represented in the spectrum. Since turbulence spectra are a spatial, rather than temporal phenomenon, corresponding 100 second averages of velocity ($\overline{U}$) were used to convert frequency (cps) to wavenumber (cpm). Vehicle velocity (U) was prone to large variations only during periods of climbing or descent, where climbs typically increased speeds by as much as a factor of 2, and descents on average would reduce the speed up to a half. Outside of these manoeuvres, U typically varied by ± 20 cm s^{-1}, and hence using 100 second averages for the conversion to wavenumber did not constitute a serious alteration to spectral distributions. The final co-spectra of velocity and temperature, and velocity and salinity, were compiled by ensemble averaging of the cospectral periodograms according to fixed wavenumber bins, uniformly distributed in logspace. The lowest bin center used in the integration is $k = 0.023$ cpm, and the highest bin center is $k = 1.02$ cpm. These outer bin centers define the bandwidth of flux estimates ($0.018 < k < 1.20$ cpm).

Examples of co-spectra (solid line) and quadrature spectra (dashed line) resulting from this technique are shown in Fig. 4.12. The upper two panels correspond to a region dominated by downgradient fluxes, where the heat flux ($\overline{w'T'}$) on the left is negative, and the salt flux ($\overline{w'S'}$) on the right is positive. The middle two panels correspond to mixed co-spectra, which exhibit dominant downgradient fluxes at most scales ($0.05 - 0.3$ cpm), and some restratification at the largest scales ($0.02 - 0.04$ cpm). The bottom panels show a general reversal in sign from the downgradient co-spectra in the upper panels, and represent a region dominated by countergradient transport of heat and salt, where buoyancy forces dominate, despite indications that slight downgradient transport is still occurring at scales in the $0.1 - 0.2$ cpm range.

As previously summarized in Chapter 2 (Eq. 2.11), the eddy correlation method provides a direct estimate of the work done by buoyancy forces ($B = g/\rho\ \overline{w'\rho'}$) through direct estimates of the heat flux ($\overline{w'T'}$) and salt flux ($\overline{w'S'}$). These quantities are determined through the integration of $w'T'$, and $w'S'$ cospectra (Fig. 4.12) over the relevant wavenumber band, i.e.

$$\frac{1}{\rho}\overline{w'\rho'} = -\alpha\overline{w'T'} + \beta\overline{w'S'}, \tag{4.2}$$

where

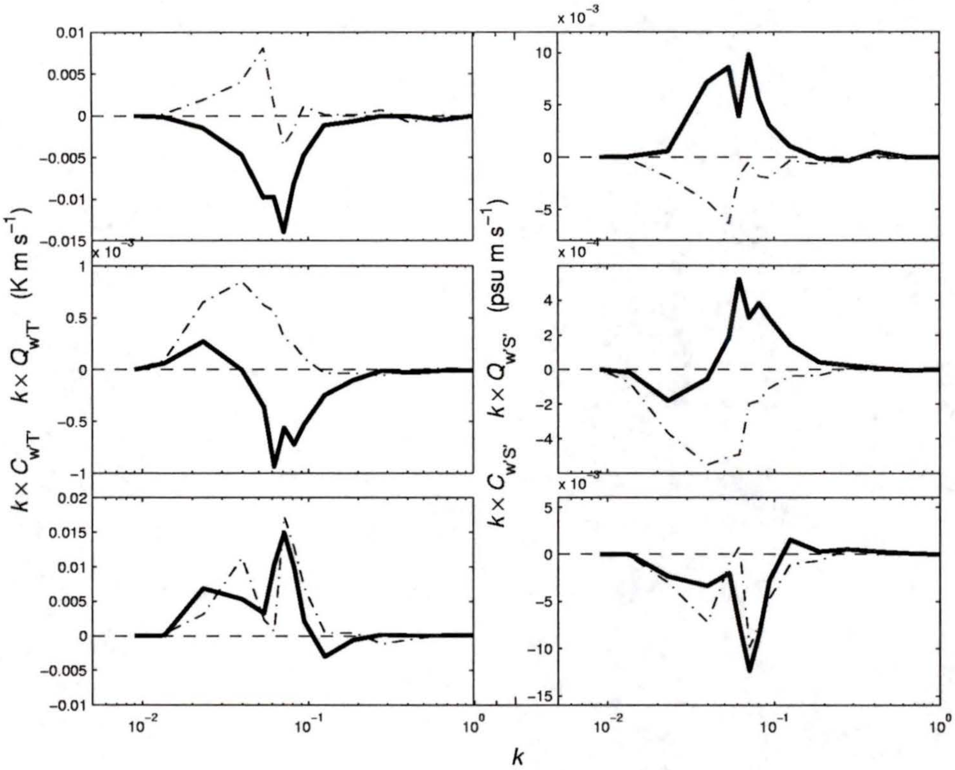

Figure 4.12: Ensemble averaged heat and salt flux co-spectra (thick lines) and quad-spectra (thin dashed lines) in variance preserving form for downgradient fluxes (upper panels), mixed fluxes (middle panels) and mostly countergradient fluxes (bottom panels). The left hand panels correspond to co-spectra of vertical velocity and temperature ($C_{w'T'}$), and the right hand panels represent their respective co-spectra for vertical velocity and salinity ($C_{w'S'}$).

$$\overline{w'T'} = \int_{0.018}^{1.2} C_{w'T'}(k)dk \quad \& \quad \overline{w'S'} = \int_{0.018}^{1.2} C_{w'S'}(k)dk. \tag{4.3}$$

Average estimates for the thermal expansion coefficient α, and saline coefficient of contraction β, are determined using formulas developed by Lillibridge (1989), which are based on the international equation of state of seawater (Millero and Poisson 1981). These coefficients depend only slightly on temperature, salinity and pressure. The work done by the buoyancy flux (B) is then determined by multiplying Eq. 4.2 by $g = 9.81$ m s^{-2}.

One check on the validity of heat and salt flux estimates in the vertical is to

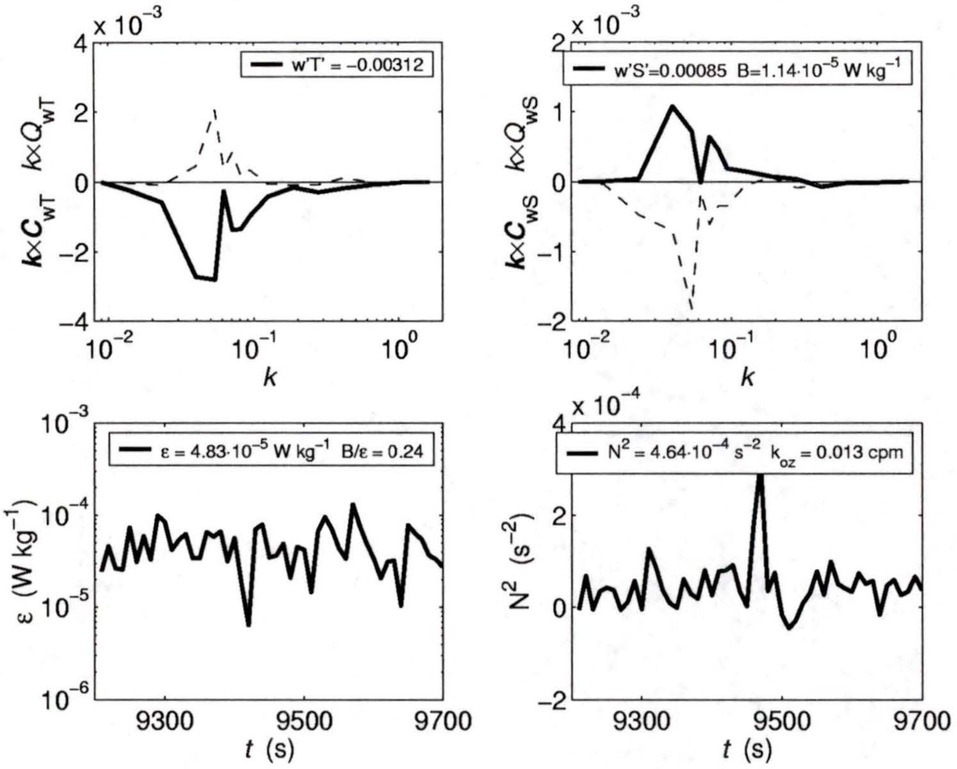

Figure 4.13: Heat and salt flux co-spectra (upper panels) in variance preserving form, dissipation rate (lower left panel) and buoyancy frequency squared (lower right panel) for 500 seconds of data. The buoyancy term $B = g/\rho\overline{w'\rho'}$ is determined from $\overline{w'T'}$ and $\overline{w'S'}$ using Eq. 4.2.

estimate the horizontal magnitudes of these quantities. For stratified flow in a straight and narrow channel, the expectation is that horizontal heat flux ($\overline{v'T'}$) and salt flux ($\overline{v'S'}$) are near zero, due to an expected lack of density gradient in the horizontal. However, channels that force the mean flow around bends and over rough topography are expected to exhibit potentially significant horizontal fluxes. Vertical overturning as a result of vertical shear, when exposed to horizontal shearing in a bend, evolves into a spiraling motion that supports fluxes through advection in the horizontal. Sansum Narrows encompasses two significant bends, one just south of the Narrows, and another about 1 nautical mile to the south-west. Horizontal fluxes for only a select few regions within the channel have been calculated, but preliminary results confirm that a small net horizontal flux does exist just south of the southernmost

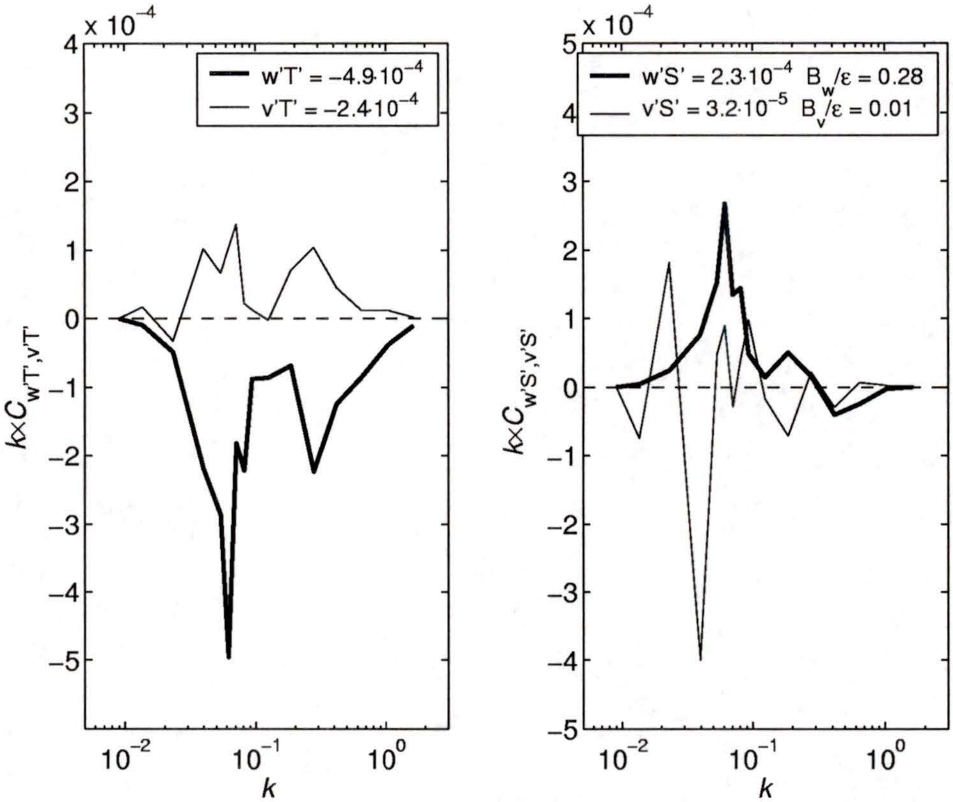

Figure 4.14: An example of the horizontal flux of heat and salt compared to their vertical counterparts, determined by calculating cospectra using v' in place of w'. For this case, there is little flux of density in the horizontal.

bend. Fig. 4.14 shows an example of horizontal heat and salt fluxes (thin lines) and the corresponding vertical fluxes (thick lines) for a region just north of the narrowest part of the channel. The tide is at full flood, and the water is fairly well mixed from being funnelled through the Narrows. The expectation in this case is that horizontal fluxes are near zero since the flow has been travelling a straight path for over 1000 meters. Although there appears to be a somewhat noticeable horizontal heat flux, a negligible salt flux renders the net horizontal buoyancy flux insignificant ($B_v/\epsilon = 0.01$) in comparison to the vertical buoyancy flux ($B_w/\epsilon = 0.28$).

4.2.4 Statistical Significance

The test for statistical significance in buoyancy flux estimates is to determine if they are significantly different from zero. This assessment is achieved using a technique outlined by Lueck and Wolk (1999), which is applied to the heat and salt flux estimates used to determine B.

Traditionally, covariance estimates have been assessed through the generation of two statistically uncorrelated time series that have the same probability density function and spectra as the series under consideration (Yamazaki and Osborn 1993, Fleury and Lueck 1994). The uncorrelated series are formed by lagging one series by an amount greater than the larger of the two auto-decorrelation times (τ_0), which is given by the first zero crossing of their auto-covariance functions. These lagged estimates are used to form a sample distribution of covariance for two statistically independent series. The distribution should be centered on zero, and its range indicates the probability of obtaining a flux estimate that is nonzero. This technique requires the calculation of a large number of lagged time series in order to generate a reliable PDF, and as a result the technique is cumbersome and time consuming.

The computational expense required to carry out this analysis is significantly reduced by simply computing the lagged covariance functions

$$R_{w'T'}(\tau) = \overline{w'(t)T'(t+\tau)} \;\;\&\;\; R_{w'S'}(\tau) = \overline{w'(t)S'(t+\tau)}, \tag{4.4}$$

where τ is time lags greater than τ_0. Comparison of these estimates to $R_{w'T'}(0)$ and $R_{w'S'}(0)$ then provides a measure of how significantly different the covariance estimate ($\tau = 0$) is from all lagged estimates. If $R_{w'T'}(0)$ and $R_{w'S'}(0)$ stand out, ie, they fall outside of the ±95 percentile range of the lagged estimates, then they are deemed significant.

The sample distribution used to test the significance of flux estimates is a compilation of all the values outside of $|\tau| \geq \tau_0$ generated by the functions

$$R_{w'T'}(\tau) = I[W*(f)T(f)]L^{-1} \;\;\&\;\; R_{w'S'}(\tau) = I[W*(f)S(f)]L^{-1}, \tag{4.5}$$

file	length [s]	$10^4\overline{w_1'T_1'}$ [$\mathrm{ms^{-1}K}$]	$10^4\lvert\rho_0\rvert$	$10^4\lvert\rho_{95}\rvert$	$10^4\overline{w_1'S'}$ [$\mathrm{ms^{-1}psu}$]	$10^4\lvert\rho_0\rvert$	$10^4\lvert\rho_{95}\rvert$	$10^6 B_1$ [$\mathrm{Wkg^{-1}}$]
E2_1	1100	-2.23	2.8	2.5	2.08	1.2	1.5	-
E2_2	400	-39.14	60.9	19.8	22.99	32.7	10.3	24.0
E2_3	1400	-14.86	24.7	10.6	7.01	12.4	5.9	7.80
E2_4	600	5.05	3.8	6.7	-7.26	3.4	3.7	-
E2_5	600	-18.08	21.4	13.7	6.26	7.7	6.4	7.60
E2_6	1100	-18.13	24.5	9.9	8.13	12.2	4.3	9.06
F1_1	1000	-20.66	28.8	26.6	7.12	13.9	13.8	8.85
F1_2	1000	-19.29	18.2	26.4	9.78	9.3	15.3	-
F1_3	1500	-40.06	49.1	26.4	18.79	32.4	15.7	20.9
F1_5	1100	-5.85	3.5	5.2	3.11	2.7	2.8	-
F1_6	1500	-3.49	3.0	2.2	1.59	1.8	1.4	1.77
F1_7	800	-3.25	3.8	2.4	1.96	2.4	1.5	2.01
F2_1	600	-37.84	49.8	39.9	23.99	35.9	26.6	24.6
F2_2	500	-44.27	39.4	49.8	16.98	29.3	36.5	-
F2_3	400	41.89	30.8	27.2	-28.71	20.4	17.7	−28.8
F2_4	1000	-23.69	15.8	36.6	21.79	16.0	24.0	-
F2_5	900	-7.58	9.9	14.4	4.75	4.7	8.6	-
F2_6	400	58.58	71.7	36.8	-24.17	34.4	15.0	−28.6
F2_7	600	-2.11	6.7	1.8	0.22	0.33	0.11	0.51
F2_8	2000	-1.14	1.2	0.7	0.13	0.04	0.04	-

Table 4.2: Heat flux ($\overline{w'T'}$) and salt flux ($\overline{w'S'}$) estimates based on measurements using airfoil probe $M05$ (Position P1) and thermistor $T01$ (Position T1). The statistical significance of these estimates are evaluated using the cross covariance technique on lagged signals. Values of ρ_0 that fall below ρ_{95} render the buoyancy term estimate (B_1) based on these fluxes statistically no different from zero.

where W, T and S are the Fourier transforms of w', T' and S', I represents the inverse Fourier transform, and L is the length of the time series.

Table 4.2 summarizes the heat and salt flux estimates computed using airfoil probe $M05$, thermistor $T01$, and the nose *Sea-Bird* conductivity cell. Alongside each estimate are values for the lagged covariance at $\tau = 0$ (ρ_0) and for the 95 percentile range of randomly lagged estimates (ρ_{95}). Flux estimates that have an associated zero lag covariance value greater than the 95 percentile confidence value are considered statistically significant, and the resultant buoyancy term estimate is kept. Table 4.3 summarizes the statistical significance of heat and salt flux estimates computed using

file	length [s]	$10^4\overline{w_2'T_2'}$ [ms^{-1}K]	$10^3\lvert\rho_0\rvert$	$10^3\lvert\rho_{95}\rvert$	$10^4\overline{w_2'S'}$ [ms^{-1}psu]	$10^3\lvert\rho_0\rvert$	$10^3\lvert\rho_{95}\rvert$	$10^6 B_2$ [Wkg^{-1}]
E1_1	1700	-2.96	3.4	2.3	1.76	2.1	1.4	1.82
E1_2	600	-31.68	47.3	15.5	18.81	30.0	9.5	19.8
E2_1	1100	-2.98	3.9	2.2	2.61	2.1	1.4	2.48
E2_2	400	-28.38	29.1	13.6	17.75	18.8	7.2	18.2
E2_3	1400	-20.68	33.0	10.6	9.95	18.1	6.1	11.0
E2_4	600	14.30	12.0	6.5	-9.87	7.4	3.7	−9.70
E2_5	600	-17.15	18.9	12.5	7.06	9.0	6.1	8.05
E2_6	1100	-18.09	21.0	7.5	8.66	11.3	3.5	9.45
E3_1	1700	-4.91	4.7	2.7	2.30	2.4	1.7	2.59
E3_2	1800	-18.21	25.5	10.3	10.01	17.2	6.2	10.5
E3_3	800	-2.13	4.1	5.4	2.41	3.2	2.8	-
E3_4	700	-6.43	6.6	5.3	2.97	4.0	2.7	3.26
E3_5	400	11.97	10.8	9.4	-4.87	5.1	2.9	−5.56
E3_6	700	-23.82	21.0	7.2	4.68	5.9	3.5	7.31
E3_7	800	-10.24	7.8	10.7	2.39	1.9	5.4	-
E3_8	1300	-1.08	1.2	0.5	0.15	0.2	0.1	0.29
F1_1	1000	-8.33	7.4	18.2	8.04	3.0	13.2	-
F1_2	1000	-26.70	38.4	19.1	13.22	23.3	11.3	14.6
F1_3	1500	-20.32	25.9	18.0	7.58	16.3	10.9	9.17
F1_4	800	-43.73	56.0	23.5	19.31	26.2	13.0	22.0
F1_5	1100	-3.36	9.5	5.6	1.71	3.9	3.0	1.85
F1_6	1500	-3.49	3.4	1.8	0.55	1.0	1.4	-
F1_7	800	-5.62	5.6	2.0	1.59	2.3	1.2	2.14
F2_1	600	-23.91	15.5	37.8	14.41	12.5	25.3	-
F2_2	500	-58.55	53.5	43.6	27.31	39.3	32.0	30.6
F2_3	400	24.56	18.1	23.4	-26.05	14.7	15.5	-
F2_4	1000	-59.98	65.0	32.6	37.48	41.7	21.6	38.3
F2_5	900	-23.22	27.4	12.0	12.05	14.4	7.3	13.1
F2_6	400	48.87	63.7	30.4	-17.02	26.7	12.4	−21.5
F2_7	600	-2.03	8.0	2.5	0.04	4.1	1.6	0.36
F2_8	2000	-1.52	1.8	0.6	0.50	0.8	0.4	0.63

Table 4.3: Heat flux ($\overline{w'T'}$) and salt flux ($\overline{w'S'}$) estimates based on measurements using airfoil probe $M09$ (Position P2) and thermistor $T02$ (Position T2). The statistical significance of these estimates are evaluated using the cross covariance technique on lagged signals. Values of ρ_0 that fall below ρ_{95} render the buoyancy term estimate (B_2) statistically no different from zero.

airfoil probe $M09$, thermistor $T02$, and the nose *Sea-Bird* conductivity cell. The two combinations of thermistor and airfoil probe were chosen based on proximity to one another, where $M05$ occupied the position P1 as shown in Fig. 3.2, and $M09$ occupied P2.

The results in Tables 4.2 and 4.3 indicate that the majority of flux estimates are significant. Disregarding the lack of B1 estimates for E1 and E3 files, it appears that flux estimates made using the combination M09 and T2 are more reliable. Of twenty flux estimates made by both combinations, eight flux estimates using M05 and T01 failed the significance test compared to four by M09 and T02. Also worth mention is the questionable estimate of fluxes for file F2_7. Both combinations of probe and thermistor shown statistical reliability in their estimates, but large differences in the calculated fluxes and those indicated by ρ_0 suggest the buoyancy term is unreliable, since ρ_0 is in itself an estimate of the variance.

4.3 Results

The scaled buoyancy flux as described in Section 2.1.2 is given by the ratio of work done by buoyancy flux, to the energy lost through dissipation, i.e.

$$R = \frac{\frac{g}{\rho}\overline{w'\rho'}}{\epsilon} = \frac{B}{\epsilon}. \tag{4.6}$$

File names, time intervals, and estimates of the buoyancy term (B) are tabulated in Tables 4.2 and 4.3. Estimates of the buoyancy term that pass the test for significance are combined in Table 4.4 with average estimates of the dissipation rate to provide values for the scaled buoyancy flux R. E1 and E2 file segments are from evening ebbs on August 11th and 13th, and E3 files pertain to a tow during the morning ebb on August 14th. The F1 and F2 file segments are from afternoon flood tides on August 14th and August 15th respectively. Since more than one vertically oriented probe and thermistor were present during tows for the E2, F1 and F2 file segments, two separate estimates of the scaled buoyancy flux (R) could be established. For E2, F1 and F2 files, R_1 corresponds to a scaled buoyancy flux estimate using the airfoil Mantle probe *M05* and the thermistor *T01*, and for all files, R_2 is the estimate

file	length [s]	$10^6\epsilon$ [Wkg^{-1}]	10^4N^2 [s^{-2}]	$N^2 < 0$ [%]	$1/N$ [s]	10^{-3} $\epsilon/\nu N^2$	R_1 B_1/ϵ	R_2 B_2/ϵ	$\overline{R}$	k_{oz} [cpm]
E1_1	1700	2.81	6.04	5	41	3.58	-	0.65	0.65	0.36
E1_2	600	44.10	2.23	25	67	152.12	-	0.45	0.45	0.04
E2_1	1100	3.30	5.23	6	44	4.85	-	0.75	0.75	0.30
E2_2	400	38.35	2.91	21	59	101.51	0.63	0.47	0.55	0.06
E2_3	1400	23.36	5.10	14	44	35.29	0.33	0.47	0.40	0.11
E2_4	600	17.86	1.92	22	72	71.71	-	-0.54	-0.54	0.06
E2_5	600	19.93	1.31	28	88	116.85	0.38	0.40	0.39	0.04
E2_6	1100	20.90	3.45	15	54	46.60	0.43	0.45	0.44	0.09
E3_1	1700	3.35	11.71	1	29	2.20	-	0.77	0.77	0.55
E3_2	1800	48.96	4.63	21	46	81.41	-	0.21	0.21	0.07
E3_3	800	5.53	4.72	11	46	9.01	-	-	-	0.22
E3_4	700	18.47	1.03	33	99	138.16	-	0.18	0.18	0.04
E3_5	400	22.86	0.21	41	218	830.91	-	-0.24	-0.24	0.01
E3_6	700	40.49	0.53	30	137	588.92	-	0.18	0.18	0.02
E3_7	800	18.72	4.58	15	46	31.41	-	-	-	0.12
E3_8	1300	0.48	1.30	8	144	2.83	-	0.60	0.60	0.28
F1_1	1000	66.09	3.61	22	53	140.85	0.13	-	0.13	0.05
F1_2	1000	59.34	1.96	31	71	232.73	-	0.24	0.24	0.03
F1_3	1500	43.00	5.45	22	43	60.69	0.49	0.21	0.35	0.09
F1_4	800	34.67	4.54	16	47	58.62	-	0.63	0.63	0.08
F1_5	1100	4.97	4.48	6	47	8.53	-	0.37	0.37	0.21
F1_6	1500	3.59	9.71	1	32	2.84	0.49	-	0.49	0.46
F1_7	800	4.50	5.73	1	42	6.04	0.45	0.48	0.47	0.27
F2_1	600	89.90	5.75	25	42	120.27	0.27	-	0.27	0.06
F2_2	500	114.40	3.39	25	54	258.68	-	0.27	0.27	0.04
F2_3	400	42.82	1.75	28	76	188.13	-0.67	-	-0.67	0.04
F2_4	1000	104.56	3.90	31	51	206.44	-	0.37	0.37	0.04
F2_5	900	20.18	3.32	21	55	46.80	-	0.65	0.65	0.09
F2_6	400	43.18	2.08	34	69	159.76	-0.66	-0.50	-0.58	0.04
F2_7	600	2.19	4.43	1	48	3.80	0.23	0.16	0.20	0.32
F2_8	2000	1.08	7.75	0	36	1.07	-	0.59	0.59	0.70

Table 4.4: Flux estimates for ebb (E1, E2 and E3) and flood (F1 and F2) tides in Sansum Narrows. The R_1 estimate is based on w' from airfoil probe *M05*, and thermistor *T01*, and R_2 is the estimate from *M09* and *T02*. Also tabulated are estimates of the dissipation rate (ϵ), the buoyancy frequency squared (N^2), the buoyancy Reynolds number ($\epsilon/\nu N^2$), and the Ozmidov wavenumber (k_{oz}).

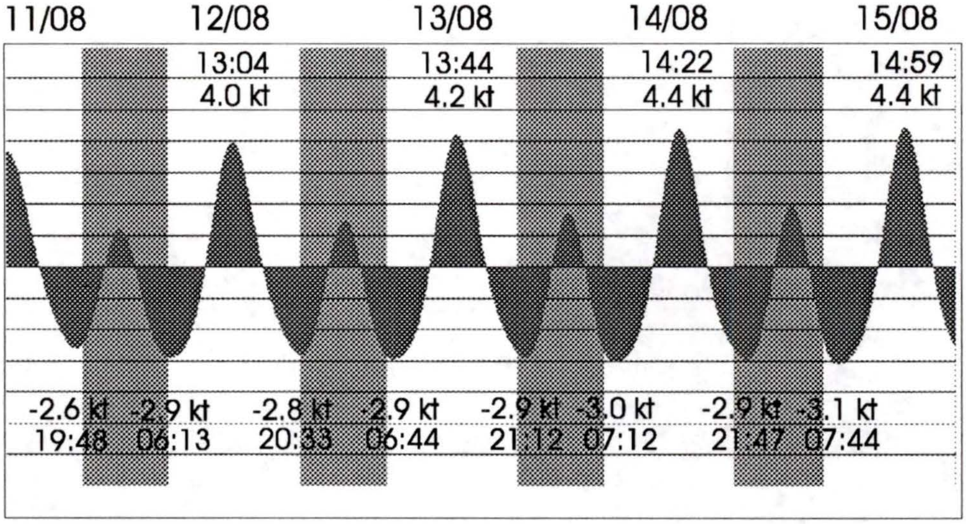

Figure 4.15: Semi-diurnal tidal currents for Sansum Narrows from August 11^{th} to August 15^{th} and their peaks.

from *M09* and thermistor *T02*. For E1 and E3 files, the probe *M05* was oriented horizontally to obtain a measure of the horizontal component of shear. Also, the other two probe locations were occupied by the relatively new Bullet probe, which has superior resolution at higher wavenumbers over Mantles, but suffers from more severe temperature contamination at lower wavenumbers.

Also incorporated into Table 4.4 are average estimates of the buoyancy frequency squared (N^2), the buoyancy Reynolds number (Re_b) and the Ozmidov wavenumber (k_{oz}) for all file segments. Comparison of $1/N$ to file length yields insight into the number of turbulent realizations potentially captured by the file segment, where files with lengths far exceeding the respective value for $1/N$ are likely to incorporate many overturns at various stages of evolution, whereas shorter files with larger estimates for $1/N$ are potentially capturing fluxes from only a small part of an overturn. Crawford (1987) found that for buoyancy length scales slightly smaller ($\approx 4/5$) than respective Thorpe scales for turbulence in a stably stratified fluid, the decay-time constant of kinetic energy is $3/5 - 1$ times the value of the buoyancy period $1/N$. This estimate is based on the assumption that the buoyancy period is constant, and represents the time scale associated with the decay of turbulence if the source of TKE is suddenly no longer present. Although it is not necessarily representative of the evolution and

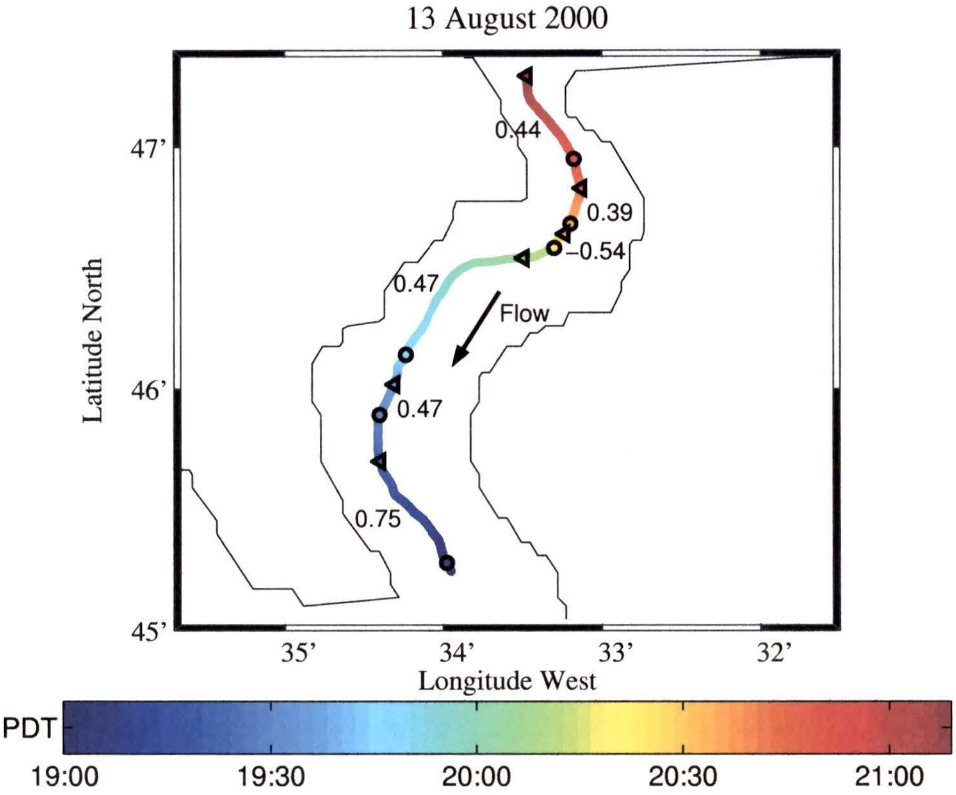

Figure 4.16: Scaled buoyancy flux results (E2 files) with respect to channel position for the evening ebb tide of August 13^{th}. R estimates correspond to tow sections which start with a circle ($\circ$) and end with a triangle ($\triangleleft$). The peak current was -2.9 knots at 21:12.

decay of a Kelvin-Helmholtz billow, it does suggest that file segments significantly longer than estimates for $1/N$ encompass a number of turbulent realizations. The decay time of a Kelvin-Helmholtz instability is expected to be of order $1/N$.

Figs. 4.16 and 4.17 correspond to the physical locations of average R estimates for tows during two ebb tides (Table 4.4). Fig. 4.16 displays the locations of R estimates for the E2 file segments, and Fig. 4.17 shows R estimates from the ebb tide the following morning (E3 files), which peaked at 7:12 am (-4.4 knots). Scaled buoyancy flux estimates for E2 files are the average ($\overline{R}$) of the two independent estimates of the scaled buoyancy flux, assuming both satisfied the test for statistical significance (Section 4.2.4). The estimation of R in the same locations during a series of ebb tides provides insight into the generalities and variability in B/ϵ for Sansum Narrows.

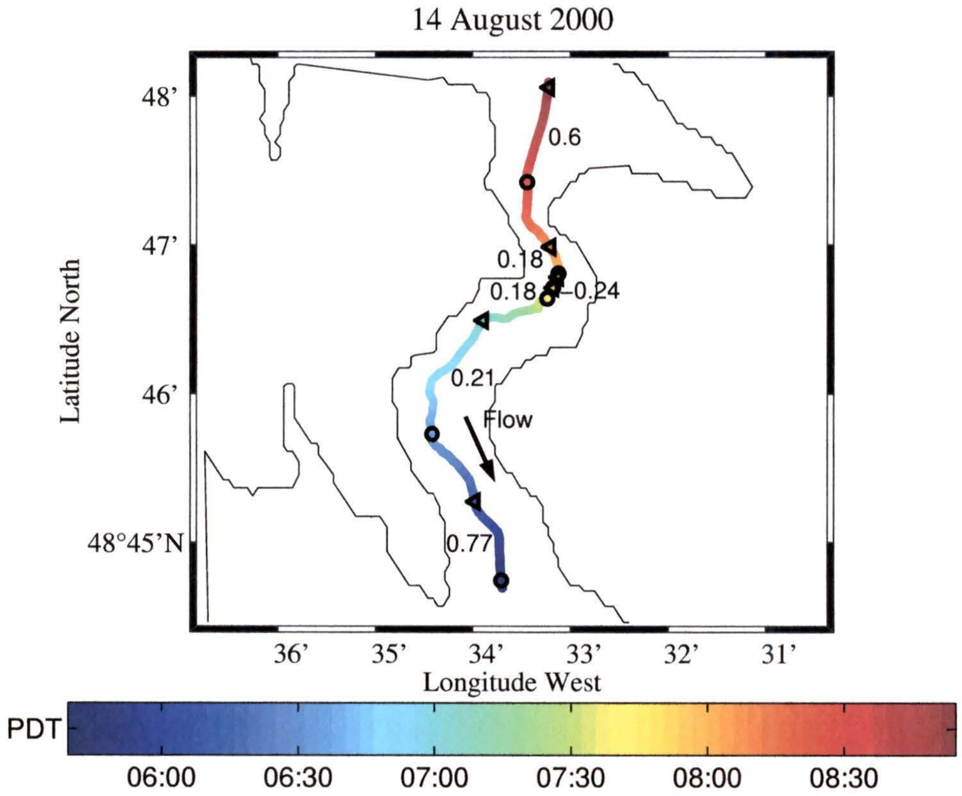

Figure 4.17: Scaled buoyancy flux results (E3 files) with respect to channel position for the morning ebb tide of August 14^{th}. R estimates correspond to tow sections which start with a circle ($\circ$) and end with a triangle ($\triangleleft$). The peak current was -3.0 knots at 07:12.

The southern portion of the channel between Ctd-02 and Ctd-03 produces consistently high estimates for R, which range from 0.65 to 0.77. Further upstream, in the vicinity of Ctd-04, R estimates are consistently lower ($R \approx 0.45$), and become more variable in the shallower waters half a nautical mile to the north-east ($0.21 < R < 0.47$). At Ctd-05, co-spectra exhibit occasional countergradient content at the lowest wavenumbers ($0.02 \rightarrow 0.04$), resulting in lower estimates of the scaled buoyancy flux ($R \approx 0.18$). Concurrently, pronounced upgradient transports in this region yield $R = -0.54$, and seem to coincide with the center of the northernmost turn in the channel, just south of the Narrows. The flow in the vicinity of Ctd-06 is markedly turbulent, with corresponding higher levels of dissipation and near zero values for N^2. Patches of downgradient transport with associated R values as high as

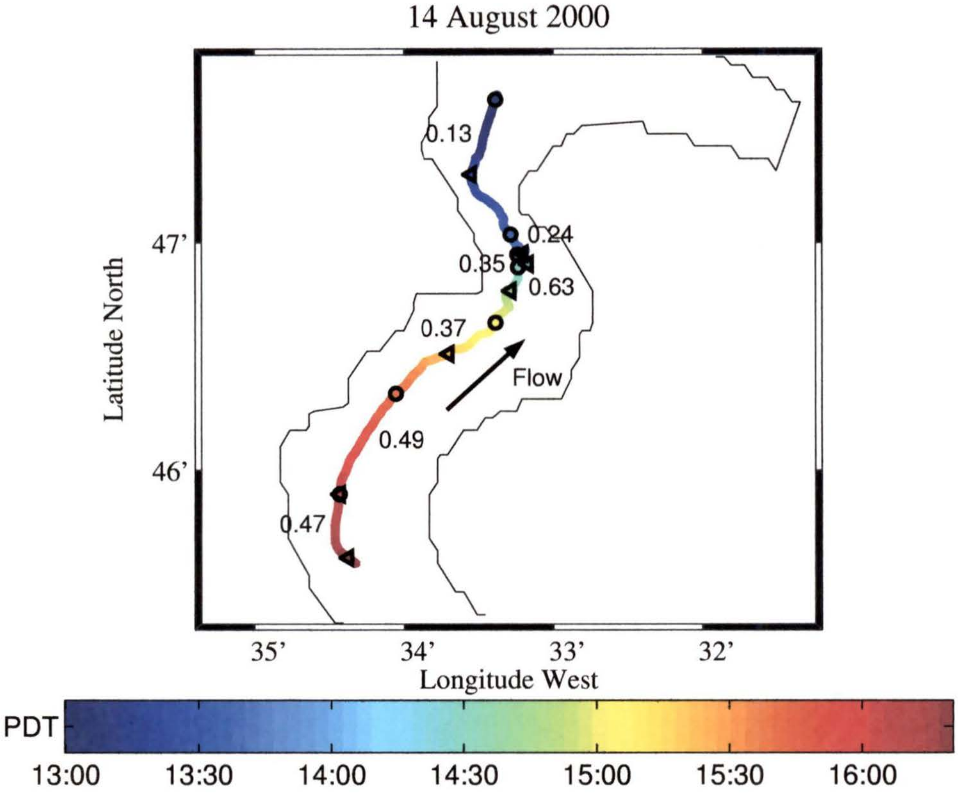

Figure 4.18: Scaled buoyancy flux estimates (F1 files) with respect to channel position for the afternoon flood tide of August 14^{th}. R estimates correspond to tow sections which start with a circle ($\circ$) and end with a triangle ($\triangleleft$). The peak current was +4.4 knots at 14:22.

0.39 are surrounded by regions of upgradient transport ($R \approx -0.24$). In the narrowest part of the channel, one-half nautical mile north of Ctd-06, R appears to increase again to 0.44, followed by another increase to $R \approx 0.60$ in the vicinity of Ctd-08. To summarize, it appears that B is relatively high with respect to ϵ well before the flow converges into the Narrows. Partially mixed water then entering the Narrows mixes vigorously but at lower R until the first bend, where the swirling motions in the turn and visible boils at the surface coincide with intense intermittent upgradient transports. This vigorous restratification may be partially responsible for the elevated fluxes of buoyancy and higher values of R found further downstream in the vicinity of Ctd-04. The largest values of R occur in between stations Ctd-03 and Ctd-02, but do not correspond to the highest levels of net mixing (highest B estimates), but rather,

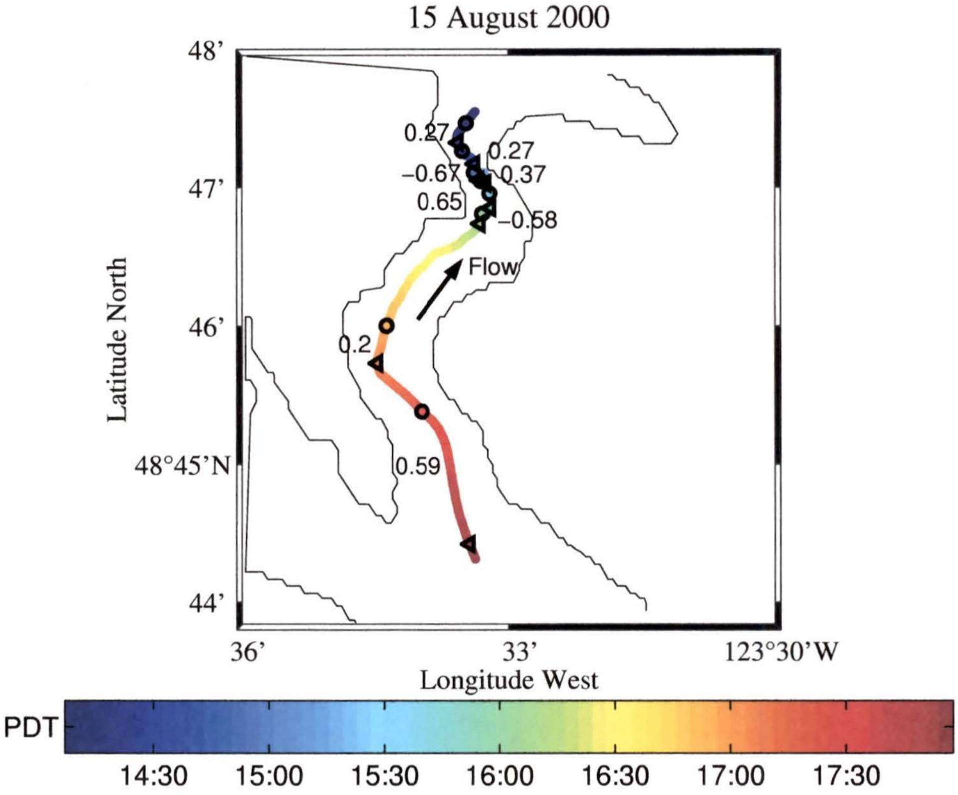

Figure 4.19: Scaled buoyancy flux estimates (F2 files) with respect to channel position for the afternoon flood tide of August 15th. R estimates correspond to tow sections which start with a circle ($\circ$) and end with a triangle ($\triangleleft$). The peak was +4.4 knots at 14:59.

occur in a region of relatively low dissipation rate.

Figs. 4.18 and 4.19 present the locations for estimates of R associated with tows during flood tides in Sansum Narrows (Table 4.4). Progressing southwards from Stuart Channel towards the Narrows, we begin to see elevated turbulence levels in the region north of the Narrows (Ctd-08), but lower values for R. The scaled buoyancy flux is as low as 0.13 at Ctd-08, and remains less than 0.27 for the stretch of water between Ctd-08 and Ctd-07. Once within the Narrows, estimates of R begin to rise from 0.27 at Ctd-07, to 0.65 by Ctd-06. Interspersed with these downgradient estimates are significant countergradient transports to as high as $R = -0.67$, which are typically occurring for only short periods ($t < 500$ s). Once around the northernmost bend, and into the shallowest section of the channel (Ctd-05), R ceases to exhibit

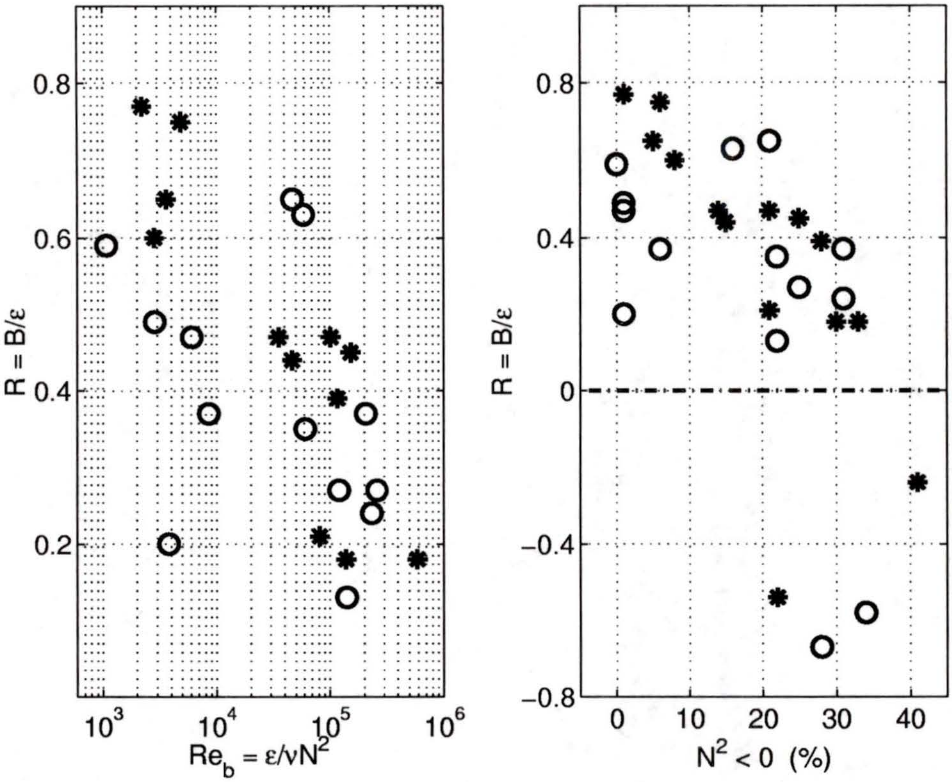

Figure 4.20: Values for B/ϵ compared to the buoyancy Reynolds number (left panel), and to the fraction of N^2 that is negative (right panel). Estimates of R from ebb tides are represented by stars ($*$) and from flood tides by circles ($\circ$).

countergradient transports and shows a general positive increase with progression in a southerly direction. Estimates of R climb from 0.37 at Ctd-05, to 0.49 at Ctd-04, to 0.59 between Ctd-02 and Ctd-03. One short estimate of R in the vicinity of Ctd-04 suggests R could be as low as 0.20 in that region; but corresponds to a file that has already been flagged as questionable (F2_7). In summary, the waters flowing northwards through SN exhibit a range in R from one end of the channel to the other. The highest estimates for R occur in a region south of the southernmost bend. R estimates then show a decreasing trend as the southern bend is rounded and waters climb the hump in the vicinity of Ctd-05. As this partially mixed water rounds the northernmost bend, it plunges into the deeper but narrower section between Ctd-06 and Ctd-07, resulting in regions of intense mixing and occasional displays of pronounced upgradient transport. The high levels of vertical shear as measured by the

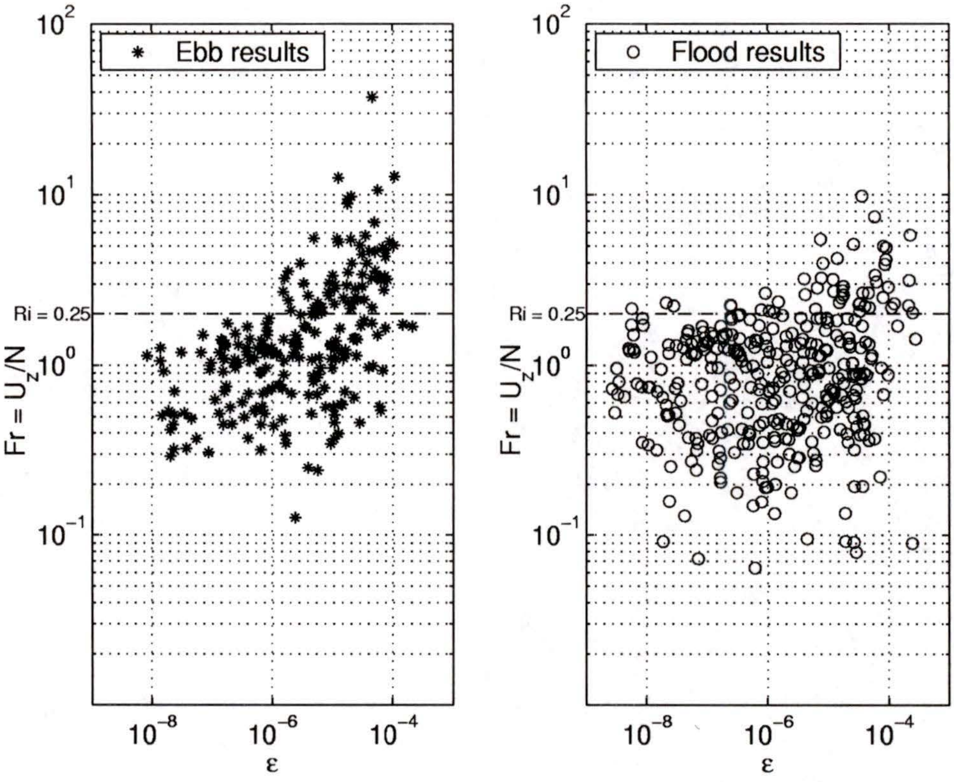

Figure 4.21: Froude number with respect to dissipation rate (ϵ) for an ebb tide (left panel) and a flood tide (right panel). A Froude number of 2 corresponds to the critical Richardson number 0.25.

ADCP suggest mixing is particularly vigorous in this region. The highest values for B calculated in this study also correspond to this region during flood tides. By the time the flow reaches the opening into Stuart Channel, values for R are much reduced.

Fig. 4.20 is a plot of the scaled buoyancy flux ($R = B/\epsilon$) results with respect to buoyancy Reynolds number (Re_b) for all positive values of R (left panel), and the scaled buoyancy flux estimates with respect to the fraction of N^2 estimates that are less than zero (right panel). Estimates for R from ebb tides are plotted using stars ($*$), and estimates for flood tides are shown using circles ($\circ$). Comparison of these quantities indicates that the work done by buoyancy forces relative to dissipation rate diminishes as Re_b increases, and shows a similar tendency as the percentage of negative values in N^2 increases. Also, negative values for the scaled buoyancy flux (i.e. upgradient transports) begin to appear only when the fraction of the record with

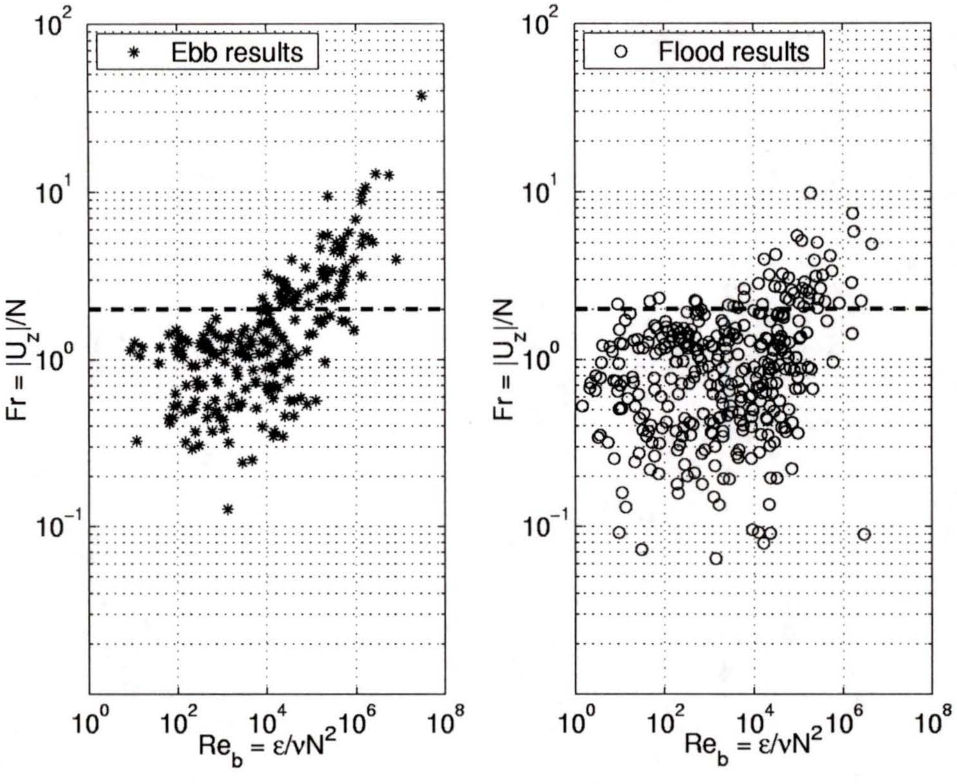

Figure 4.22: Froude number with respect to the buoyancy Reynolds number for an ebb tide (left panel) and a flood tide (right panel). A Froude number of 2 corresponds to the critical Richardson number 0.25.

$N^2 < 0$ is higher than 20%. The file F2_7, which was earlier earmarked as potentially unreliable, appears in the left panel as the circle closest to zero in the vicinity of $Re_b = 4 \times 10^3$.

Fig. 4.21 compares the Froude number (Eq. 4.1) to the dissipation rate ϵ for the two tows depicted in Figures 4.7 and 4.8. The data in the left panel correspond to the ebb tide on the morning of August 14^{th}, and in the right panel to the flood tide that afternoon. Both flows show increasing variability in the Froude number with respect to increasing dissipation rate. A critical Richardson number of 0.25, which is equivalent to a Froude number of 2, is marked by a dashed line in both panels. Values for Froude number tend to remain below this theoretical threshold until $\epsilon \approx 10^{-6}$ W kg^{-1}, above which the Froude number varies from $0 \rightarrow 13$ by $\epsilon = 10^{-4}$ W kg^{-1}. The highest values for B/ϵ (files E1_1, E2_1 and E3_1) in Sansum

Narrows correspond to dissipation rates in the range $2.8 \cdot 10^{-6} < \epsilon < 3.4 \cdot 10^{-6}$ W kg^{-1}. This range for ϵ coincides with $0.2 < Fr < 3$. Fig. 4.22 compares the same Froude number data from Fig. 4.21 to the buoyancy Reynolds number. The highest measured values for R in Sansum Narrows occur in the range $2 \cdot 10^3 < Re_b < 5 \cdot 10^3$ (Fig. 4.20), which coincide with Froude numbers ranging from 0.2 to 2. This range in Froude number is equivalent to a gradient Richardson number range of $0.25 < Ri < 25$.

Chapter 5

Discussion

5.1 Flow in Sansum Narrows

The observations and description of water properties in the vicinity of Sansum Narrows during the course off ebb and flood tides presented here is only relevant to summer conditions. Seasonal variations are much greater near shore than out in the open sea, and so in order to obtain a complete picture of oceanographic conditions in the region it is necessary to extend observations over one or more full years. A single summer cruise is quite obviously insufficient to describe the full range of water characteristics and the times and extent of changeover periods between winter and summer extremes in Sansum Narrows. That said, with the large array of instrumentation made available for the summer cruise in August of 2000, significant observational information has led to the identification of a number of flow features that are of scientific interest.

Somewhat unexpected was the discovery that waters produce such high estimates for the scaled buoyancy flux north of the Narrows during ebb tides. A lack of evidence for turbulence near the surface in Satellite Channel during ebb tides belied the mixing of heavily stratified waters beneath. In hindsight, it appears less than surprising that dissipation levels were sufficiently high to overcome the pronounced ambient stratification in Stuart Channel when considering the series of bends in the channel north of the Narrows that southward travelling water must navigate. As the seawater carries on into the Narrows, a slight decline in R estimates is observed as waters become mixed, only to rise again after the narrowest section of the channel has been negotiated. As expected, flows within the Narrows are highly turbulent during peak flows, and yield the highest values for B during ebb tides. However, the highest computed values for the scaled buoyancy flux occur in a region further downstream.

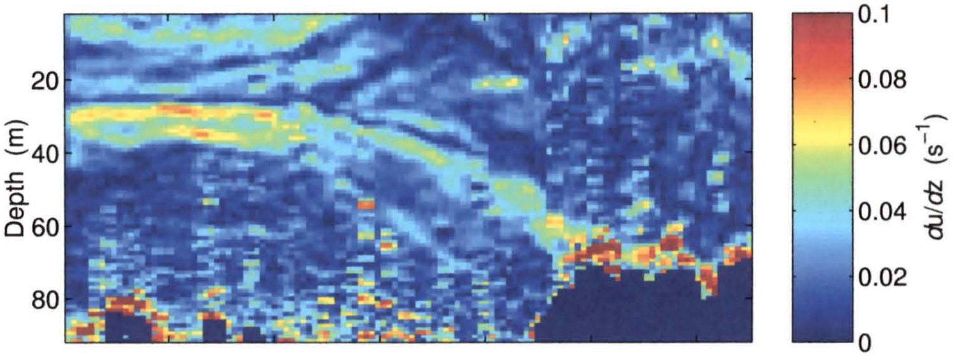

Figure 5.1: Distinct flow separation in the southern region of Sansum Narrows during an ebb tide as seen through ADCP measurements of vertical shear. The flow is ebbing southward, from right to left.

Estimates for B/ϵ peak in the southern portion of Sansum Narrows, just south of the second bend, and are perhaps in part the result of a marked flow separation (Fig. 5.1) south of Ctd-04. This $5-10$ meter thick plume of enhanced shear emanates from bottom topography and appears to gravitate towards a depth of $30-40$ meters further downstream. It's presence contributes to vertical mixing, and hence entrainment, of deeper water in the faster flowing upper layer.

Colder, denser water from Satellite Channel is carried northward through Sansum Narrows with the flooding tide, producing higher estimates of R along the length of the channel, and vigorous mixing in the Narrows. The temperature profile shown in Fig. 4.6 indicates that, during a flood tide, the mixed water mass emerging from the Narrows encounters significant stratification at the surface in the southern portion of Stuart Channel, and subsequently dives to a depth of $15-25$ meters. As it does so, it exhibits a wavelike form. This feature suggests the possibility that the flow is hydraulically driven. A more likely explanation is the water mass is forced below light water at the mouth of the Narrows, and rebounds off deeper, denser water slightly further downstream, thereby creating a waveform which quickly dissipates. By approximating the narrowest part (vertically) of this flow to be $2-3$ meters, and assuming a maximum flow rate of 4.4 knots (2.3 m s^{-1}), we discover the Froude number is no greater than 0.5, implying the flow never goes critical (Fr $=1$). Dissipation rates also appear to be lower (Fig. 4.8) north of the Narrows during flood tides, suggesting the unlikelihood of a breaking wave in the vicinity of Ctd-08.

5.2 Fluxes

5.2.1 Auto- and Co-Spectra

Velocity and temperature spectra show some general trends with respect to estimates of R. Ebb tide file segments E1_1, E2_1 and E3_1 (Table 4.4) all correspond to higher values of R (~ 0.7), and originate from the southern portion of Sansum Narrows during ebb tides. In most cases, spectral peaks for vertical velocity and temperature coincide. One file with a high R estimate shows spectral peaks that are relatively shifted, where velocity tends to be at higher wavenumber (0.06 cpm) and temperature at lower wavenumber (0.04 cpm). This feature of velocity and temperature spectra was reported by Gargett and Moum (1995), hereafter GM, for oceanic measurements and Kaimal et al. (1972) for the atmospheric boundary layer. Further upstream from this region during the ebb, estimates for R tend to decrease (~ 0.45). Corresponding spectra show coincidence of w' and T' spectral peaks. For file segments E1_2, spectra peak at 0.04 cpm, and for E2_2 and E3_2, spectral peaks coincide at 0.06 cpm. From the few files exhibiting countergradient transports, it appears that spectral peaks shift such that the spectral maxima for w' occurs at slightly lower wavenumber than the peak for T'. Spectra from flood tide measurements show similar trends.

Another feature which occurs sporadically amongst spectra are indications that temperature variance is present below 0.02 Hz. A few examples exist where either the temperature peak has not been reached by the low wavenumber cutoff of the high-pass filter, or the peak is present but obvious attenuation of the temperature signal has taken place as a result of filtering. The effect of not fully resolving the low wavenumber content of the thermistor signal on heat flux estimates is assumed to be relatively insignificant, since vertical velocity spectra for these files show little variance at wavenumbers just above 0.02 cpm.

Through comparison of turbulent lengthscale, velocity and diffusivity scalings with data from numerical, laboratory and field experiments, Barry et al. (2001), hereafter BIWI, finds that the rmsturbulent lengthscale is independent of the rate of dissipation of turbulent kinetic energy when $\epsilon/\nu N^2 > 300$ (Gargett and Moum 1995). This finding is not necessarily validated by results in this study since our Re_b values are consistently higher than this transition value, but is certainly not disputed by spectral estimates of w' found in Sansum Narrows. Vertical velocity spectral peaks varied between 0.04 – 0.07 cpm for the vast majority of flux estimates, with a slight bias towards peaks at higher wavenumber for regions of lower dissipation. This range in wavenumber is not viewed as significant in light of the large range in dissipation rate represented by them. BIWI also suggests that for a given N, an increase in ϵ does not result in an increase in the turbulent overturn scale but rather, leads to an increase in the magnitude of the *rms* turbulent velocity. This concept appears to be supported by measurements of w' in Sansum Narrows, where turbulent velocities of 10 cm s^{-1} at $\epsilon = 5 \times 10^{-6}$ increase to $w' > 20$ cm s^{-1} in regions where $\epsilon = 5 \times 10^{-5}$ W kg^{-1}, for similar scales.

Co-spectra of w' and T', and w' and S', are downgradient, countergradient, or a mix of the two states. The most common form for co-spectra from Sansum Narrows was downgradient transport in the wavenumber range $0.04 < k < 0.5$ cpm, accompanied by countergradient fluxes at mostly larger scales ($0.02 < k < 0.04$ cpm). Occasionally there was evidence of countergradient fluxes at smaller scales while downgradient transports were occurring at larger scales. This mixed form for the co-spectrum has been observed by a number of researchers attempting to directly measure fluxes (Gargett and Moum 1995, Moum 1996). Also, GM found their co-spectra peaked somewhere between the peaks for w' and T', whereas in this study the vast majority of co-spectral maxima occurred at wavenumber locations common to all signals.

Good agreement in peaks between heat and salt fluxes for all data segments allows for some general observations about co-spectral peaks to be made. As previously pointed out, file segments E1_1, E2_1 and E3_1 all provide elevated estimates for R (~ 0.7). E1_1 and E2_1 have co-spectral peaks at 0.05 cpm, considerable content above 0.05 cpm, and similar dissipation rates (3×10^{-6} W kg^{-1}). E3_1 peaks at 0.07 cpm, but also has more pronounced countergradient content at lower wavenumbers than E1_1 and E2_1. Slightly further upstream at Ctd-04, dissipation levels have climbed to $\epsilon \approx 4 \times 10^{-5}$ W kg^{-1} (E1_2, E2_2 and E3_2), R estimates have dropped

(~ 0.45), and co-spectral peak locations all lie in the range $0.04 < k < 0.06$ cpm. Dissipation rates for flood file segments F1_1 and F1_2 are high ($\epsilon \approx 6 \times 10^{-5}$ W kg^{-1}) and originate from the narrowest section of the channel. Associated estimates of R vary between $0.13 - 0.25$, and correspond to co-spectral peaks at 0.06 cpm. Further upstream, and away from the intense turbulence found at the channel constriction, we find higher values for R (~ 0.45) with associated co-spectral peaks in the $0.07 - 0.08$ cpm range (F1_6 and F1_7). Co-spectral peaks for both ebb and flood tides describing countergradient transports seem to gravitate towards $k \approx 0.04$ cpm, and always correspond to higher dissipation rates ($\epsilon > 1 \times 10^{-5}$ W kg^{-1}). The most pronounced countergradient co-spectra occasionally had a small downgradient contribution at wavenumbers larger than $k = 0.09$ cpm.

In an earlier study, Gargett et al. (1984) determined that for stratified turbulent flows, the velocity spectrum peaked in the range $(0.5 - 1)k_o$. In this study, the in-situ measurement of N^2 and ϵ allowed for estimates of the Ozmidov wavenumber for each file segment to be made (Table 4.4). These values for the Ozmidov wavenumber varied from as low as 0.01, to as high as 0.5, and to some degree relates to estimates of R. The highest values of R had associated k_o values at higher wavenumbers ($0.08 < k_o < 0.5$), whereas the lower and sometimes negative values of R always had corresponding Ozmidov wavenumbers less than 0.06 cpm. A few estimates of k_o appear to be excessively large, implying smaller flux carrying scales than observed in measured co-spectra. Since k_o is an average estimate of the Ozmidov wavenumber for the entire record length, it seems possible that co-spectra implying larger scales than the ambient stratification would allow are due to an event(s) within the data segment that produce significant fluxes of density but that do not occur sufficiently long for k_o to be heavily influenced.

Addressing the question of differential diffusion in Sansum Narrows can be achieved by comparing heat and salt fluxes through the scaling of their co-spectra by the mean temperature and salinty gradients. For the 1000 second file segment in Fig. 5.2, $C_{w'T'}(k)$ has been scaled by T_z, and $C_{w'S'}(k)$ by S_z. The resulting co-spectra show a clear resemblance, and yield similar variance estimates, indicating that heat and salt are mixed equally by the turbulence in this instance. In general, co-spectra from Sansum Narrows showed similar proportions to the unscaled versions of co-spectra

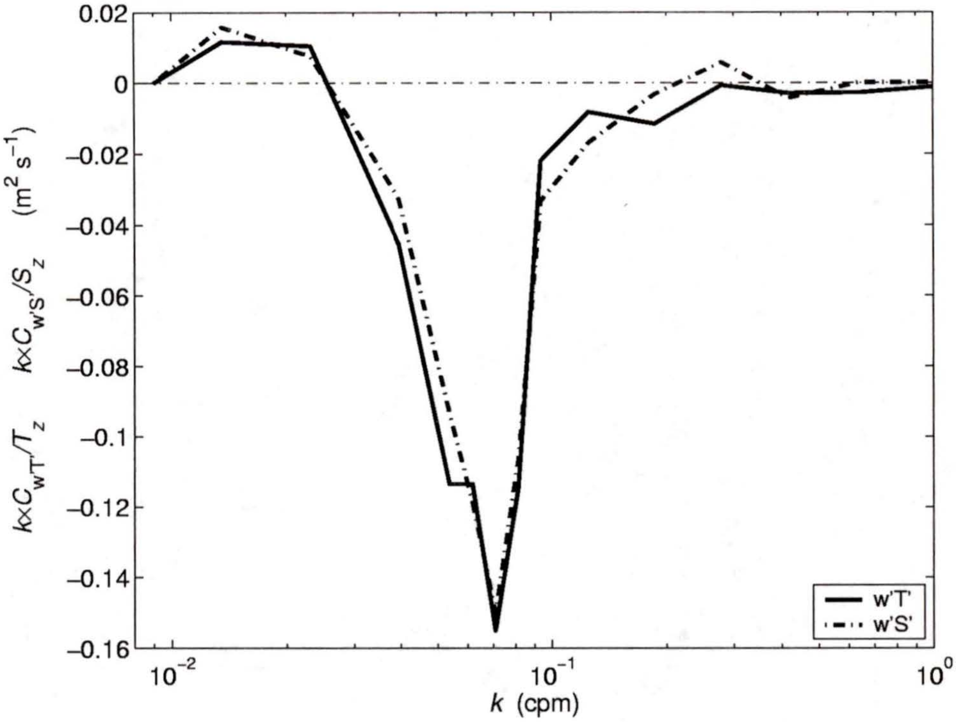

Figure 5.2: The co-spectra from Fig. 3.7 scaled by their respective gradients. Their near identical forms indicate that, for this file segment, there is little evidence to suggest differential diffusion is occurring; i.e. heat and salt appear to be mixed equally by the turbulence.

shown in Fig. 5.2, suggesting that different diffusion rates for heat and salt in Sansum Narrows were generally not common (assuming the gradient ratio is similar to this case).

5.2.2 Buoyancy Flux Estimates

Buoyancy flux estimates show general trends for ebb and flood tides in Sansum Narrows. Within the Narrows (Ctd-07), the buoyancy flux is estimated to be 9×10^{-6} W kg^{-1} for an ebb tide near its peak, which is over a decade higher than an estimate north of the Narrows. Estimates in the vicinity of Ctd-06 range from 8×10^{-6} for downgradient fluxes, to occasional upgradient transport as high as -1×10^{-5} W kg^{-1}. Southerly flow past Ctd-05 experiences downgradient buoyancy fluxes on the order 3×10^{-6} W kg^{-1}, followed by more vigorous mixing at Ctd-04 where $B \approx 2 \times 10^{-5}$ W kg^{-1}. Further downstream, between Ctd-03 and Ctd-02, where estimates for R are the highest measured, we find B values never exceeding 2.6×10^{-6} W kg^{-1}. In summary, it appears that for ebb tides, R is a maximum at the north and south extremities of Sansum Narrows, whereas the highest measured values for B occur within the Narrows, and at the southern-most bend (Ctd-04).

Waters travelling northwards with the flood tide experience buoyancy fluxes no greater than 2×10^{-6} W kg^{-1} up until just past the region near Ctd-05. As the flow draws into the narrowest section of the channel and becomes highly turbulent, downgradient transports produce buoyancy fluxes as high as 2.2×10^{-5} W kg^{-1}, accompanied by occasional upgradient transports on the order -2.5×10^{-5} W kg^{-1}. As the flow progresses towards the mouth of the Narrows (Ctd-07), the buoyancy term periodically exceeds 3×10^{-5} W kg^{-1}. Once in Stuart Channel, just north of the Narrows, we see a decline in B of almost 3 times despite a persistently high dissipation rate, suggesting the water has been well mixed by this stage. In summary, for flood tides in SN it appears that consistently higher values of R are found in the southern portion of the channel, alongside periodic higher values from within the Narrows. However, R shows a decreasing trend with flow through the Narrows. The highest buoyancy fluxes correspond to the region between Ctd-06 and Ctd-07 for flood tides, with levels a decade lower to the south (Ctd-02 to Ctd-05), and only a third as high to the north (Ctd-08).

The dominant wavenumbers at which buoyancy fluxes are occurring lie in the 0.04-0.07 cpm range, which indicates a dominant wavelength range for buoyancy fluxes of $14 < \lambda < 25$ meters. If we define the length scales associated with these wavelengths by

$$L = (2\pi)^{-1} \times \lambda, \tag{5.1}$$

then it appears that buoyancy fluxes in Sansum Narrows are dominated by overturns with scales of $2 - 4$ meters. With the above discussion in mind, it then follows that high R values correspond predominantly to scales of $2 - 3$ meters ($0.05 < k < 0.08$), whereas higher buoyancy fluxes are carried by $3 - 4$ ($0.04 < k < 0.06$) meter scales.

Plotting buoyancy term estimates from both probes with their respective estimates

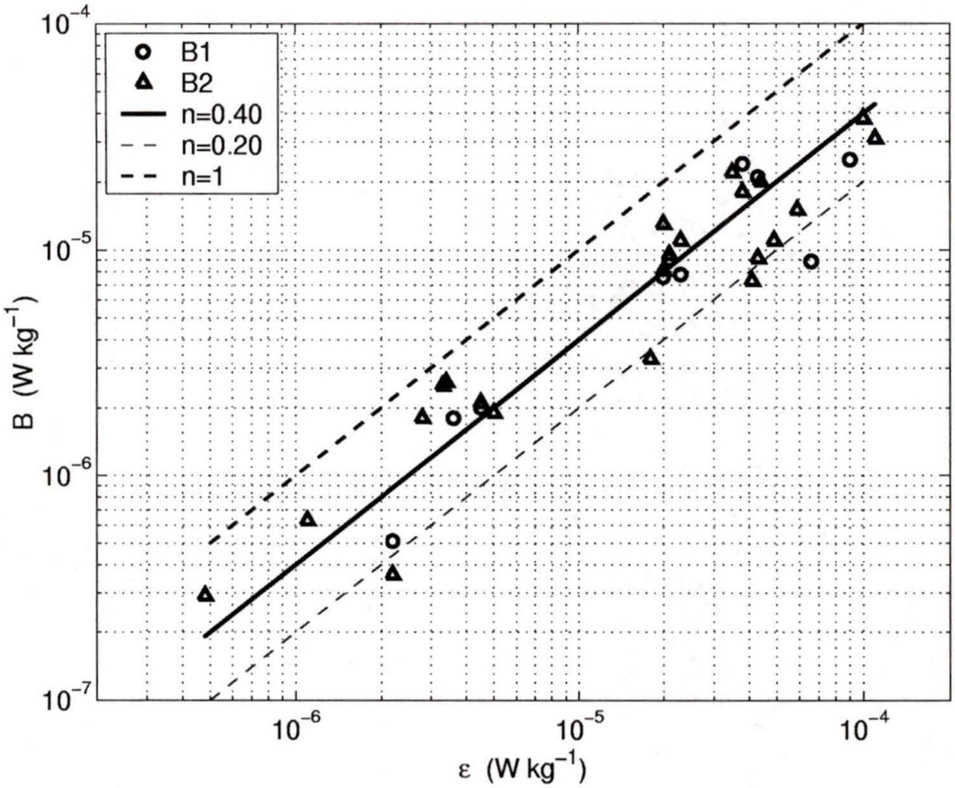

Figure 5.3: All non-negative estimates of the buoyancy terms $B1$ and $B2$ with respect to the dissipation rate ϵ. The resultant points in logarithmic space yield a best fit line when R=0.40. Also plotted are lines representing R=0.20 and R=1.0.

of dissipation rate (Fig. 5.3) reveals that B is an increasing function of ϵ. Both $B1$ and $B2$ estimates are plotted here, and are overlain by a best fit line representing $R = 0.40$. Also plotted are lines corresponding to $R = 0.20$, the long term maximum value for Γ suggested by Osborn (1980), and $R = 1$, which corresponds to $B = \epsilon$.

The average for all positive values of the scaled buoyancy flux is $\overline{R} = 0.41$, with a 95% bootstrap range of 0.35 to 0.47. An alternate average scaled buoyancy flux is provided by the inverse of the mean of the inverse of R, which yields $(\overline{R^{-1}})^{-1} = 0.33$ with a 95% bootstrap range of 0.28 to 0.40. The range between these equally valid average estimates for R is relatively small, however, both averages still lie outside the confidence intervals of the alternate estimate. These results suggest an average flux Richardson number (R_f) of 0.25 – 0.29 for Sansum Narrows.

5.3 Dimensionless Parameters

5.3.1 R vs. Fr

Rohr and Atta (1987), hereafter RA, undertook the measurement of near steady state mixing efficiency in a stably stratified shear flow in a laboratory. One general result achieved from analysis of their results was the increasing trend in mixing efficiency (R_f) with an increase in Richardson number (where $0.02 < Ri < 0.08$). With regard to Froude number, their results imply mixing efficiency tends to grow as the Froude number decreases (for $3.5 < Fr < 7.1$). When the gradient Richardson number falls within $0.08 < Ri < 0.25$, they postulate that mixing efficiency most likely does not decrease significantly since while $Ri \leq 0.25$, turbulence continues to grow downstream. However, for increasing values of Ri above $Ri \approx 0.25$ ($Fr \approx 2$), the turbulence was found to decay, and R_f was observed to decrease due to the growing proportion of internal waves replacing the turbulence. The authors also observe that the net mixing in their laboratory flows is greatest where the turbulence is greatest (high ϵ), although the mixing there is least efficient.

R values are typically highest in Sansum Narrows in regions outside of the Narrows, where ϵ is somewhat reduced and stratification is more pronounced. A typical dissipation rate associated with these higher values for R is $\epsilon = 3\times10^{-6}$ W kg^{-1}, which corresponds to Froude numbers (Fig. 4.21) at and slightly above $Fr \approx 2$ ($Ri \leq 0.25$). This agrees with observations made by RA, and suggests that the Froude number may be an effective means for determining relative estimates of B/ϵ. Furthermore, RA's observation that the highest levels of mixing do not in fact coincide with the most efficient mixing is also observed in Sansum Narrows.

It also appears that the highest estimates for R in SN occur when $Fr \approx 2$ when considering the plots of Re_b with respect to Fr (Fig. 4.22). From Fig. 4.20 we observe the highest R estimates occur within a limited buoyancy Reynolds number range centered on 4×10^3, which corresponds to Froude numbers in the vicinity of $Fr = 2$. R estimates begin to fall off as $Re_b \gg 4 \cdot 10^3$, which corresponds to Froude numbers increasing above 2, and Richardson numbers decreasing below 0.25. RA find an increase in mixing efficiency (R_f) with increasing Ri below 0.25, which agrees with the trends in R observed in Sansum Narrows.

5.3.2 R vs. Re_b

Only a handful of researchers have attempted to understand the relationship between dimensionless parameters such as the buoyancy Reynolds number ($Re_b = \epsilon/\nu N^2$) and measured buoyancy fluxes. Ruddick and Walsh (1997), hereafter RW, estimated an apparent mixing efficiency (Γ_d) from microstructure measurement estimates of χ and ϵ, according to

$$\Gamma_d = \frac{\chi N^2}{2\overline{T_z^2}\epsilon}, \tag{5.2}$$

where Γ_d is the true mixing efficiency assuming the conditions for validity of both the Osborn-Cox (1972) and the Osborn (1980) models are satisfied, and the observed mixing is conventional high Reynolds number turbulence ($K_T = K_\rho$). By accepting this criteria, they found an increasing trend in Γ_d from 0.10 to 0.35 as Re_b increased from 40 to 2000. Gargett and Moum (1995) also calculated Γ_d according to Eq. 5.2, and found Γ_d was consistently much lower than direct estimates of mixing efficiency obtained from ADCP and CTD measurements in conjunction with Osborn's method (Osborn 1980).

Although these results do not permit a direct comparison with those found in this study, they do lend themselves well to explain potential behaviour of B/ϵ at buoyancy Reynolds numbers not measured in Sansum Narrows. The lowest estimate of Re_b for which a value for B/ϵ exists is $Re_b = 2000$ (Fig. 4.20). The upwards trend witnessed by RW is not contradicted by results from Sansum Narrows, but rather suggests a possible peak in B/ϵ in the $1000 < Re_b < 10,000$ range for flows of this nature.

GM established a mean value of $\Gamma_0 \approx 0.7$ for a series of passes through tidal fronts in Haro Strait. Γ_d for the same tows produced a mean efficiency over 3 times lower, implying that either the direct estimate is overestimated, or the indirect approach (Γ_d) tends to underestimate the buoyancy flux. GM go on to provide a number of arguments in favour of the direct approach over the indirect, most significant of which being the assumptions made when using indirect methods for estimating fluxes. In defense of their seemingly high direct estimates of Γ, GM also argue that if phase differences exist between velocity, temperature and salinity signals, then direct estimates of fluxes are more likely to be underestimated. Their mean estimate for mixing efficiency ($\Gamma \sim 0.7$) has associated Reynolds number on the order $Re \approx 10^7$. This estimate comes from assuming $w' = 20$ cm s^{-1}, $l = 50$ meters, and $\nu = 1 \times 10^{-6}$ m^2 s^{-1}. Initially, this result seems to contradict the trend plainly visible in Fig. 4.20, which indicates that with increasing buoyancy Reynolds number beyond $Re_b \sim 10^4$, the ratio B/ϵ begins to decrease. What is not clear is the variability in Reynolds number associated with GM's mean mixing efficiency estimate. It seems possible a range in Re was realized over the duration of their measurements.

Further questions are raised when comparing the results from this study to those summarized by BIWI. Figure 5.4 (upper panel) is a compilation of results from primarily laboratory experiments (Rohr 1985, Itsweire et al. 1987, Barry et al. 2001) which show a dependence of the flux Richardson number R_f on the buoyancy Reynolds number Re_b. The horizontal line ($R_f = 0.15$) corresponds to Osborn's (Osborn 1980) suggestion that the mixing efficiency is on average $\Gamma \approx 0.20$. Their results suggest a maximum R_f and hence mixing efficiency at $Re_b \approx 10^2$, with a subsequent fall off in R_f with increasing Re_b. At $Re_b = 10^2$, $R_f \approx 0.10$, and by $Re_b = 10^4$, R_f has decreased to below 0.01.

The results from this study (lower panel) show a different yet similar story in regards to R_f with respect to Re_b. The most significant difference between results lies in the value for R_f, where estimates of B/ϵ from Sansum Narrows were as high as 0.77. By adopting the assumptions made by Osborn (Osborn 1980), this estimate of B/ϵ produces an R_f value of 0.43, which is over 3 times as high as the maximum estimates assumed by BIWI. The similarity between results lies in the trends witnessed at the higher buoyancy Reynolds numbers in each case. Both exhibit a distinct roll off as Re_b increases. For data summarized by BIWI, the roll off begins at $Re_b = 10^2$ and shows a decline in R_f of over a decade by $Re_b = 10^4$. With regard to the data presented in this study, R peaks in the $Re_b = 10^3 - 10^4$ range, and a decrease in R_f with respect to Re_b is certainly evident by 10^5. By $Re_b = 10^6$, R_f has declined by almost 4 orders of magnitude.

A number of direct measurements of buoyancy flux in the ocean serve to refute the generalizations made by BIWI and others in regard to the maximum value for R_f for

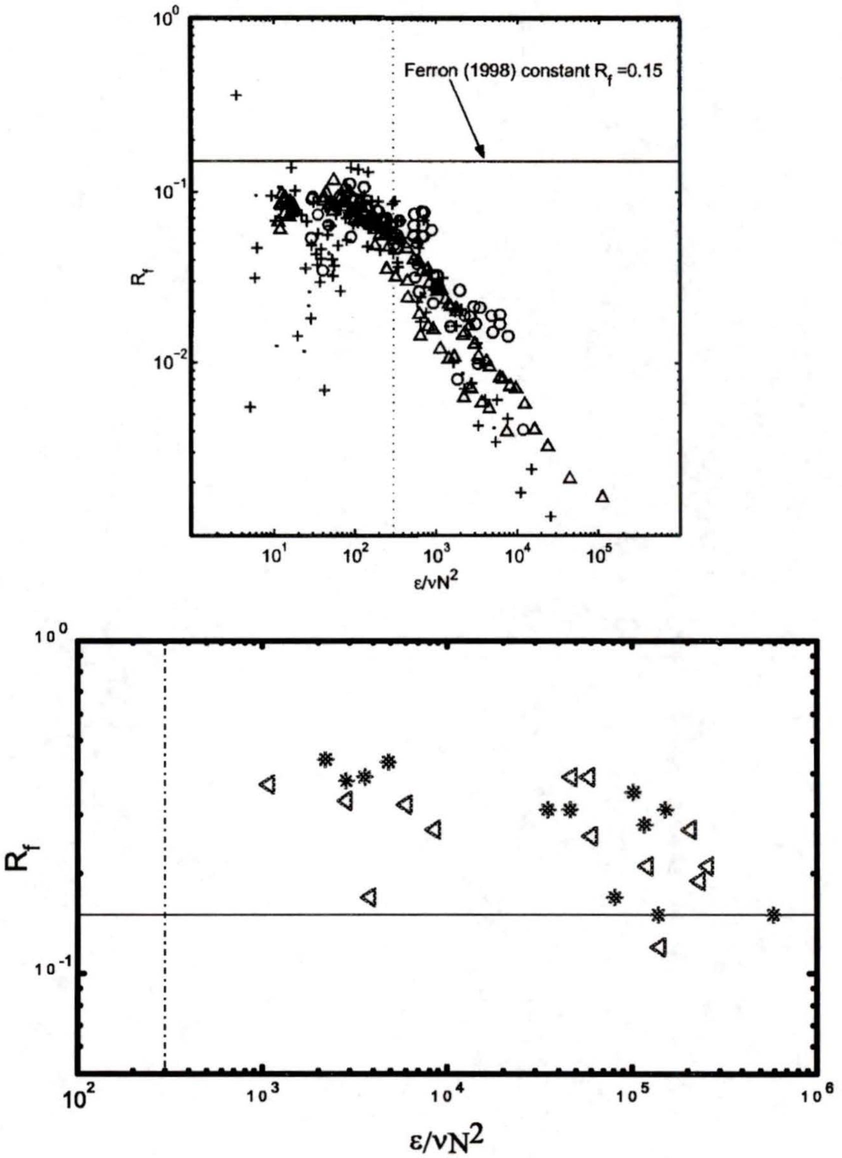

Figure 5.4: Plot of the Richardson flux number R_f with respect to buoyancy Reynolds number Re_b for field and laboratory data from Stillinger et al. (1983), Rohr (1985), Itsweire et al. (1987), Barry et al. (2001) (upper panel) and R_f vs. Re_b for this study (lower panel). Comparison of these two plots is facilitated by the horizontal solid line at $R_f = 0.15$ suggested by Osborn (1980), and the vertical dashed line at $Re_b = 300$. On the lower panel, estimates of R_f from ebb tides are represented by stars ($*$) and from flood tides by triangles ($\triangleleft$).

geophysical flows. GM estimated that R_f was as high as $R_f \approx 0.4$ for measurements taken in tidal fronts. Conventional thinking is that in order to sustain turbulence, R_f should be a good deal smaller than one. In addition to shear instabilities within the horizontal shear flow, GM also postulated that vertical flow resulting from mean horizontal convergence was directly supplying energy to the vertical component of TKE, thereby producing higher values of R_f.

RW produced estimates of the apparent mixing efficiency Γ_d (Eq. 5.2) as high as 0.35 at $Re_b = 2000$. For their data, GM have shown that estimates of Γ_d are consistently smaller than direct estimates of Γ, which suggests it is plausible that RW's results were an underestimation of the true efficiency. Hence, R_f is at least 0.26, and quite possibly higher. Wolk and Lueck (2001) used similar arguments to GM in explaining mixing efficiency estimates up to $\Gamma = 0.5$ ($R_f = 0.33$) from measurements in the oceanic boundary layer. They argue that horizontal gradients in water properties due to wind forcing causes horizontal convergences/divergences, which in turn result in additional vertical flow. This vertical flow then boosts production of turbulence and helps to overcome the buoyant energy losses that suppress turbulence.

When considering the physical processes taking place in Sansum Narrows contributing to R_f values as high as 0.4, one cannot overlook the role of the generally neglected terms in the TKE equation (Eq. 2.2). For purposes of discussion, the estimates of R_f for Sansum Narrows are calculated by assuming B/ϵ is equivalent to the mixing efficiency according to Eq. 2.7. This method for estimating R_f requires making the same assumptions made by Osborn (1980) about the relative insignificance of various terms in the TKE equation. If in fact the terms neglected by Osborn are significant, then the production term P is no longer simply the sum of B and ϵ (Eq. 2.5), but rather is larger by whatever factor the neglected terms equate to. By definition, the Richardson flux number is the ratio of the energy lost to buoyancy (B), to the production of turbulent kinetic energy from the mean flow (P). The inclusion of the neglected terms from Eq. 2.2 could increase P, and hence decrease R_f.

Regardless of our confidence in the estimate for P, the high values for R_f found in Sansum Narrows may also be explained using similar arguments to GM with regard to the underlying physical processes governing the work against buoyancy. Horizontal convergences in the mean flow in close proximity to vertical convergences due to topography throughout the Narrows suggests that large-scale vertical flows supplying energy directly into the vertical component of TKE could exist alongside the instabilities due to the vertically sheared horizontal current. The combination of these effects mean the energy available for working against buoyancy is no longer constrained by the inefficient transfer from a horizontal component (Gargett and Moum 1995), and hence values for R_f above 0.20 can be expected. Furthermore, the upper limit deemed possible for R_f (0.15) based on scaling arguments and laboratory experiments seems not to readily lend itself to larger scale geophysical flows exhibiting Reynolds numbers 10^4 times as large, and as such perhaps understanding the difference between the scales of these flow is the key to understanding the processes governing mixing.

Chapter 6

Conclusions & Future Work

Concurrent measurement of vertical velocity, temperature and salinity fluctuations has provided estimates of the heat and salt fluxes in a turbulent tidal channel. These fluxes provide estimates of the buoyancy flux (B), which are then compared with estimates of the dissipation of TKE (ϵ). The ratio of B/ϵ is found to vary significantly over the course of ebb and flood tides in Sansum Narrows, and seems to show a dependency on dimensionless buoyancy Reynolds and Froude numbers. The following points summarize the major conclusions of the study.

- The terms generally neglected with regard to the TKE equation are relatively small. The most significant term was the transport of turbulent velocity fluctuations, which amounted to less than 1/10 of the value of B for the data segment chosen.

- Inertial measurements can be used to remove body motions from airfoil probe signals. Furthermore, inertial measurements also provide low frequency motions that probes cannot resolve as a result of nose motions in larger eddies. Corrected vertical velocity signals are generally larger than 10 cm s^{-1} in Sansum Narrows during peak flows, with velocities sometimes exceeding 30 cm s^{-1} within the narrowest portion of the channel.

- The most common form for heat and salt fluxes were downgradient transport at all scales except the largest overturns (small k), which were countergradient. Spectra also exhibited entirely downgradient and occasionally entirely countergradient transports. The cospectra of w' and T', and w' and S' displayed peaks at similar wavenumbers. Cospectra rolled off at lower wavenumbers than their peak, and were zero for most cases before the high-pass cut-off at 0.02 cpm. This roll-off indicates the real decorrelation of w', T' and S'. Occasionally, cospectra were prematurely cut-off below their peak by the high-pass filtering of the signal, but since the variance at these lower wavenumbers was small, this was not deemed to be of concern.

- Buoyancy flux estimates varied significantly over the length of the channel and with respect to flow direction. For ebb tides, the maximum mixing levels were $B \approx 2 \times 10^{-5}$ W kg^{-1} in the vicinity of Ctd-04, and the minimum mixing levels were $\approx 2 \times 10^{-6}$ W kg^{-1} south of Ctd-03 and north of Ctd-07. These lower levels also correspond to the highest values for R. For flood tides, B had a maximum value of 3×10^{-5} W kg^{-1} in the narrowest portion of the channel, and lower values north of Ctd-07 and south of Ctd-05 ($\approx 2 \times 10^{-6}$ W kg^{-1}). Peak overturning scales contributing to buoyancy fluxes in Sansum Narrows are on the order 2-4 meters.

- Estimates of the scaled buoyancy flux ($R = B/\epsilon$) also varied significantly over the length of the channel and with respect to flow orientation. The larger values for R (0.60 - 0.77) during ebb tides occurred in the southern portion of the channel between Ctd-04 and Ctd-02, and north of Ctd-07. Within the narrowest portion of the channel, R varied between 0.18-0.44, and was occasionally negative. For flood tides, R remained relatively high (0.20-0.49) as the flow negotiated the southern part of Sansum Narrows, then peaked at Ctd-06 (0.65), and then displayed a decreasing trend as the water mixed rapidly between Ctd-06 and Ctd-07. By Ctd-08, R had dropped to 0.13.

- For this study, a decreasing trend appears to exist between estimates of R and the buoyancy Reynolds number Re_b. At the lowest values for Re_b measured ($10^3 - 10^4$), R is at its relative maximum (up to 0.77). By $Re_b = 5 \times 10^4$, maximum values for R remain below ≈ 0.60, and by $Re_b = 10^5$, $R \leq 0.5$. The highest value of Re_b in Sansum Narrows was $\approx 6 \times 10^5$, and its associated value for the scaled buoyancy flux is $R \approx 0.20$. Also, negative values for R only occur when $Re_b > 7 \times 10^4$.

- By assuming the generally neglected terms in the TKE are in fact insignificant, estimates of $R = B/\epsilon$ can be viewed as estimates of the mixing efficiency Γ.

These assumptions then allow for comparison of these results with those from other experiments. Estimates of R_f based on scaling arguments and laboratory experiments have concluded that mixing efficiency is a maximum at 0.20. Some researchers also show a decreasing trend in R_f with respect to Re_b. Geophysical flow experiments have produced both similar results to the lab, and other estimates of R_f that suggest Γ could be as high as 0.70 under certain flow conditions. The results from Sansum Narrows indicate that R_f is generally higher than predicted by theory and laboratory experiments, and that R_f decreases with increasing Re_b.

A few suggestions for future work are

- Further effort to evaluate the generally neglected terms in the TKE equation. One segment of data was utilized in this study to calculate average values for these terms, but a broader approach would certainly be more desirable, and could provide insight into the conditions under which these terms may in fact be significant.
- Analysis of Thorpe scales from CTD casts within the Narrows. A number of studies have found scaling relations between Ozmidov and Thorpe scales, and as such an analysis of flux scales with regard to Thorpe scales would be of interest.
- Determination of the probability distribution of dissipation rate estimates. PDF's of ϵ could provide insight into the homogeneity of the turbulence, and hence be a useful tool when trying to understand the significance of B/ϵ with regard to non-dimensional parameters like Re_b.
- More thorough profiling with a lower frequency ADCP. The nature of vertical shear north of the Narrows during a flood would be of interest, and improved resolution of the channel bottom would help to clarify the source of various flow features such as the pronounced flow separation in the south part of the channel during ebb tides.
- An attempt to model the effects of low frequency temperature changes on the response of the airfoil probe. By extending the resolution of the airfoil probes

to below 0.01 cpm we could be sure that the largest flux contributing scales are never artificially removed through the application of a high-pass filter. There is little evidence in this study to suggest that significant flux containing scales fall below 0.02 cpm however.

Bibliography

M. E. Barry, G. N. Ivey, K. B. Winters, and J. Imberger. Measurements of diapycnal diffusivities in stratified fluids. *Journal of Fluid Mechanics*, 442:267–291, 2001.

R. E. Britter. *An experiment on turbulence in a density-stratified fluid.* PhD thesis, Monash University, Victoria, Australia, 1974.

J. A. Businger. Turbulent transfer in the atmospheric surface layer. *Workshop on Micrometeorology, American Meteorological Society*, 1973.

D. R. Caldwell and J. N. Moum. Turbulence and mixing in the ocean. *Reviews of Geophysics, Supplement, AGU*, pages 1385–1394, 1995.

W. R. Crawford. A comparison of length scales and decay times of turbulence in stably stratified flows. *Journal of Physical Oceanography*, 16:1847–1854, 1987.

T. H. Ellison. Turbulent transport of heat and momentum from an infinite rough plane. *Journal of Fluid Mechanics*, 2:456–466, 1957.

B. Etkin. *Dynamics of Atmospheric Flight.* Wiley and Sons, 1972.

M. Fleury and R. G. Lueck. Direct heat flux estimates using a towed vehicle. *Journal of Physical Oceanography*, 24:801–818, 1994.

A. E. Gargett. The scaling of turbulence in the presence of stratification. *Journal of Geophysical Research*, 93:5,021–5,036, 1988.

A. E. Gargett and J. N. Moum. Mixing efficiencies in turbulent tidal fronts: results from direct and indirect measurements of density flux. *Journal of Physical Oceanography*, 25:2583–2608, 1995.

A. E. Gargett, T. R. Osborn, and P. W. Nasmyth. Local isotropy and the decay of turbulence in a stratified fluid. *Journal of Fluid Mechanics*, 144:231–280, 1984.

E. C. Itsweire, K. N. Helland, and C. W. Van Atta. The evolution of grid-generated turbulence in a stably stratified fluid. *Journal of Fluid Mechanics*, 162:299–338, 1987.

E. C. Itsweire, J. R. Koseff, D. A. Briggs, and J. H. Feiziger. Turbulence in stratified shear flow: Implications for interpreting shear-induced mixing in the ocean. *Journal of Physical Oceanography*, 23:1508–1522, 1992.

G. N. Ivey and J. Imberger. On the nature of turbulence in a stratified fluid. part i: The energetics of mixing. *Journal of Physical Oceanography*, 21:650–659, 1991.

J. C. Kaimal, J. C. Wyngaard, Y. Izumi, and O. R. Cote. Spectral characteristics of surface-layer turbulence. *Quarterly Journal of the Royal Meteorological Society*, 98:563–589, 1972.

E. L. Lewis and R. G. Perkin. The practical salinity scale 1978: a conversion of existing data. *Deep-Sea Research*, 28A:307–328, 1981.

J. H. Lienhard and C. W. Van Atta. The decay of turbulence in thermally stratified flow. *Journal of Fluid Mechanics*, 210:57–112, 1990.

J. L. Lillibridge. Computing the seawater expansion coefficients directly from the 1980 equation of state. *Journal of Atmospheric and Oceanic Technology*, 6:59–66, 1989.

R. G. Lueck, D. Huang, D. Newman, and J. Box. Turbulence measurements with a moored instrument. *Journal of Atmospheric and Oceanic Technology*, 14:143–161, 1997.

R. G. Lueck and F. Wolk. An efficient method for determining the significance of covariance estimates. *Journal of Atmospheric and Oceanic Technology*, 16:773–775, 1999.

P. Macoun and R. G. Lueck. Modelling the spatial response of the airfoil shear probe using different sized probes. *JTECH*, 2002.

F. J. Millero and A. Poisson. International one-atmosphere equation of state of seawater. *DSR*, 28:625–629, 1981.

A. S. Monin and A. M. Yaglom. *Statistical fluid mechanics: Mechanics of turbulence.* The MIT Press, 1975.

J. N. Moum. The quest for k_ρ - preliminary results from direct measurements of turbulent fluxes in the ocean. *Journal of Physical Oceanography*, 20:1980–1985, 1990.

J. N. Moum. Efficiency of mixing in the main thermocline. *Journal of Geophysical Research*, 101:12057–12069, 1996.

J. N. Moum and R. G. Lueck. Causes and implications of noise in oceanic dissipation measurements. *Deep-Sea Research*, 32:379–390, 1985.

T. D. Mudge and R. G. Lueck. Digital signal processing to enhance oceanographic observations. *Journal of Atmospheric and Oceanic Technology*, 11:825–836, 1994.

P. W. Nasmyth. *Oceanic Turbulence.* PhD thesis, University of British Columbia, Vancouver, British Columbia, Canada, 1970.

N. S. Oakey. An instrument to measure oceanic turbulence and microstructure. *Report Series BI-R-77-3, Bedford Institute of Oceanography*, page 52, 1977.

N. S. Oakey. Determination of the rate of dissipation of turbulent kinetic energy from simultaneous temperature and velocity shear microstructure measurements. *Journal of Physical Oceanography*, 12:256–271, 1982.

T. R. Osborn. Estimates of the local rate of vertical diffusion from dissipation measurements. *Journal of Physical Oceanography*, 10:83–89, 1980.

T. R. Osborn and C. S. Cox. Oceanic fine structure. *Geophysical Fluid Dynamics*, 3: 321–345, 1972.

T. R. Osborn and W. R. Crawford. *Air-Sea interaction Instruments and Methods - An Airfoil Probe for Measuring Turbulent Velocity Fluctuations in Water.* Plenum Press, New York, 1980.

S. Pond and G. L. Pickard. *Introductory Dynamical Oceanography.* Butterworth-Heinemann, Woburn, MA, 1983.

J. J. Rohr. *An experimental study of evolving turbulence in uniform mean shear flows with and without stable stratification.* PhD thesis, Engineering Sciences, University of California, San Diego, California, USA, 1985.

J. J. Rohr and C. W. Van Atta. Mixing efficiency in stably stratified growing turbulence. *Journal of Geophysical Research*, 92(C5):5,481–5,488, 1987.

J. J. Rohr, E. C. Itsweire, and C. W. Van Atta. Growth and decay of turbulence in a stably stratified shear flow. *Journal of Fluid Mechanics*, 195:77–111, 1988.

B. Ruddick and D. Walsh. Variations in the apparent mixing efficiency in the north atlantic central water. *Journal of Physical Oceanography*, 27:2,589–2,605, 1997.

T. E. Siddon. A miniature turbulence gauge utilizing aerodynamic lift. *Review of Scientific Instruments*, 42:653–656, 1971.

T. E. Siddon and H. S. Ribner. An aerofoil probe for measuring the transverse component of turbulence. *American Institute of Aeronautics and Astronautics*, 3: 747–749, 1965.

W. D. Smyth, J. N. Moum, and D. R. Caldwell. The efficiency of mixing in turbulent patches: inferences from direct simulations and microstructure observations. *Journal of Physical Oceanography*, 31(8):1969–1992, 2001.

L. St. Laurent and R.W. Schmitt. The contribution of salt fingers to vertical mixing in the north altlantic tracer release experiment. *Journal of Physical Oceanography*, 29:1404–1424, 1999.

R. W. Stewart. The problem of diffusion in a stratified fluid. *Advances in Geophysics*, 6:303–311, 1959.

D. C. Stillinger, K. N. Helland, and C. W. Van Atta. Experiments on the transition of homogeneous turbulence to internal waves in a stratified fluid. *Journal of Fluid Mechanics*, 131, 1983.

H. Tennekes and J. L. Lumley. *A First Course in Turbulence.* MIT Press Design Dept., Halliday Lithograph Corp., 1972.

S. Thorpe. Turbulence and mixing in a scottish loch. *Philosophical Transactions of the Royal Society, London*, A286:125–181, 1977.

F. Wolk. Near surface heat flux measurements with a towed vehicle. Master's thesis, University of Victoria, Victoria, British Columbia, Canada, 1997.

F. Wolk and R. G. Lueck. Heat flux and mixing efficiency in the surface mixing layer. *Journal of Geophysical Research*, 106(C9):19,547–19,561, 2001.

H. Yamazaki and T. Osborn. Direct estimation of heat flux in a seasonal thermocline. *Journal of Physical Oceanography*, 23(3):503–516, 1993.

Appendix A

Correcting Spatial Averaging

The airfoil shear probe is the only robust sensor currently available for measuring the rate of dissipation of kinetic energy in the ocean. The wavenumber (or spatial) resolution of the shear probe is determined by its physical dimensions, while the bandwidth of shear fluctuations is determined by the rate of dissipation. For most oceanic work, the Mantle airfoil probe resolves the shear spectrum adequately. However, measurements taken in regions of larger dissipation rates, such as boundary regions, require a resolution beyond that of the Mantle. The newly designed Bullet probe, with dimensions approximately one-half of those of the Mantle, was tested side by side with the Mantle probe in a vigorously turbulent tidal channel. The relative response of these two probes was the basis by which Macoun and Lueck (2002), hereafter ML, determined the wavenumber response of the airfoil probe.

Some effort has been made over the last 30 years to estimate and model the response of airfoil probes to determine the degree to which the probe signal is attenuated at high wavenumbers. Oakey (1982) was the first to suggest that airfoil probes respond as single-pole low-pass filters, and estimated the effective wavelength of his probe to be $\lambda = 2 \pm 1$ cm. The form of his amplitude squared response estimate is

$$H^2(k) = \frac{1}{1 + (\frac{k}{k_c})^2}\ , \tag{A.1}$$

where k is the cyclic wavenumber and k_c is the half-power wavenumber ($k_c = 50$ cpm).

ML chose to use Oakey's transfer function as an appropriate model for spatial averaging, and applied it to two probes of different size to obtain a relative measure of the degree of averaging by each probe. This comparison revealed that diameter is the geometric dimension that determines the spatial averaging nature of a probe. The relative response of the two types of probe indicated that both probes could be characterized by a single-pole low-pass filter, with half-power wavenumbers of

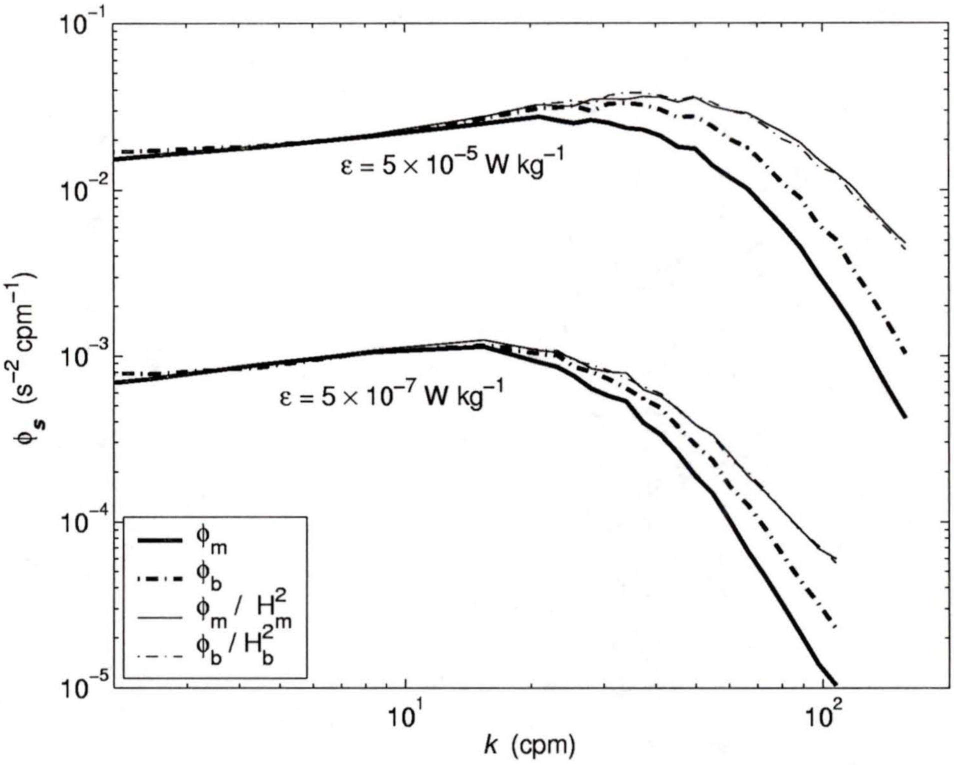

Figure A.1: Mantle (thick solid) and Bullet (thick dashed) spectra for two dissipation rates, and their corrected forms (thin solid and dashed).

49 and 88 cpm for the Mantle and Bullet probes respectively. After correction for this response, the spectra from both probes agreed closely for the dissipation range $10^{-7} - 10^{-4}$ W kg^{-1} (Fig. A.1). The Mantle probe spectra used in this study for calculation of the dissipation rate were first corrected for spatial averaging using this single-pole filter model.

Appendix B

SB Temperature & Conductivity

The *Sea-Bird* SBE3 thermometer and SBE4 conductivity cells generate a frequency proportional to the temperature and conductivity of the seawater respectively, which is digitized by the acquisition system. Temperature values are calculated from the recorded bit-count N_t using the following polynomial relation

$$T \;=\; \frac{1}{g \;+\; hF + iF^2 + jF^3} \;-\; 273.15, \quad [^\circ\mathrm{C}] \tag{B.1}$$

where g, h, i and j are sensor dependent calibration coefficients, and

$$F \;=\; ln\left[\frac{1000\;(2^{16} \;+\; N_t)}{32 \;\times\; 10^6}\right]. \tag{B.2}$$

Conductivity was extracted from the recorded bit-count N_c using

$$C \;=\; \frac{g \;+\; hF^2 + iF^3 + jF^4}{10\;(1 \;+\; \delta T \;+\; \epsilon P}), \quad [\mathrm{Siemens/m}] \tag{B.3}$$

where δ and ϵ are also sensor dependent calibrations, T is the temperature value from the SBE3 thermometer, P is the depth, and

$$F \;=\; \left[\frac{32 \;\times\; 10^6}{2^{16} \;+\; N_c}\right] \;\times\; 10^{-3}. \tag{B.4}$$

VITA

Surname: Macoun *Given name: Paul*

UNIVERSITY EDUCATION

- *University of Victoria*, Victoria, British Columbia, Canada
    - *September 1999–December 2002*
      Master of Science (Physical Oceanography)
- *University of Waterloo*, Waterloo, Ontario, Canada
    - *September 1990–April 1995*
      Honours Co-Operative Bachelor of Applied Science (Mechanical Engineering)

PUBLICATIONS

- *Modeling the response of the airfoil shear probe using different sized probes*, J. Atm. Ocean. Tech., submitted May 2002
- *Buoyancy flux estimates for a tidal channel*, J. Phys. Ocean., in preparation

WORK EXPERIENCE

- *Geco Prakla Schlumberger*, Houston, Texas, USA
    - *May 1997–January 1999*
      Seismic Engineer
- *Canamera Geological Ltd.*, Yellowknife, NWT, Canada
    - *March 1996–February 1997*
      Field Operative
- *Goodyear Canada Inc.*, Collingwood, Ontario, Canada
    - *May–September 1995*
      Projects Engineer
- *Kimberley-Clark Canada Inc.*, Huntsville, Ontario, Canada
    - *January–April 1993*
      Engineering Support
- *Energy, Mines & Resources Canada, CANMET*, Ottawa, Ontario, Canada
    - *September–December 1991*
      Research Assistant

November 21, 2002

University of Victoria
Partial Copyright License

Title of Thesis: Buoyancy Flux Estimates for a Tidal Channel.

Author: [redacted]

Paul Macoun
2002 November 1